X-ray Intensity Fluctuation Spectroscopy in the Energy Range from 1 to 4 keV

Dissertation
zur Erlangung des Doktorgrades
des Fachbereichs Physik
der Universität Hamburg

vorgelegt von

Cornelia C. Retsch

aus Hamburg

Hamburg, im März 2001

Gutachter der Dissertation:	Prof. Dr. J. R. Schneider Prof. Dr. R. L. Johnson Dr. I. McNulty
Gutachter der Disputation:	Prof. Dr. J. R. Schneider Prof. Dr. D. Heitmann
Datum der Disputation:	12.06.2001
Dekan des Fachbereichs Physik und Vorsitzender des Promotionsausschusses:	Prof. Dr. F.-W. Büßer

Abstract

X-ray intensity fluctuation spectroscopy was developed in the energy range of 1 to 4 keV and was used to study complex sample structures and dynamics in a liquid-crystal – aerosil dispersion. The advantages of a focusing versus a nonfocusing setup were explored, and the effects of using x-ray energies near absorption edges were investigated to enhance the capabilities of the method. It was found that even though excellent real space resolution and an increase in flux density can be gained from a Fresnel zone plate focusing setup, this usually comes at the expense of speckle contrast. At absorption edges, the speckle contrast is dominated by the imaginary part of the sample's index of refraction and therefore varies in a way similar to the total transmitted intensity. Employing these results, the dynamics of a dispersion of low-density silica aerosil in octylcyanobiphenyl (8CB) were studied. It was found that the known cross-over behavior of 8CB – aerosil samples towards the $3d$-XY universality class could be understood as the coupling of the aerosil-gel dynamics to the dynamics of the director fluctuations in the liquid-crystal. This work indicates that the aerosil-gel mimics and dampens these director fluctuations and thus, by suppressing the director fluctuations, achieves a pure $3d$-XY system.

Kurzfassung

Im Rahmen der vorliegenden Arbeit wurde ein Aufbau zur Röntgen-Intensitätsfluktuationsspektroskopie im Energiebereich von 1 bis 4 keV entwickelt und zum Studium komplexer Probenstrukturen und -dynamiken in einer Aerosil-Flüssigkristall-Dispersion verwendet. Die Vor- und Nachteile eines fokussierenden Aufbaus wurden mit denen eines nicht-fokussierenden Aufbaus verglichen und die Auswirkungen von Absorptionskanten auf die Speckle-Eigenschaften untersucht, um die Möglichkeiten der Methode zu erweitern. Obwohl ein Aufbau mit einer fokussierenden Fresnelschen Zonenplatte exzellente räumliche Auflösung und eine erhöhte Flussdichte bieten kann, bringt solch ein Aufbau doch gewöhnlich reduzierten Speckle-Kontrast mit sich. An Absorptionskanten wird der Speckle-Kontrast vom Imaginärteil des Brechungsindexes der Probe dominiert und variiert daher in ähnlicher Weise wie die transmittierte Intensität. Unter Ausnutzung dieser Ergebnisse wurde die Dynamik einer Dispersion aus niedrig konzentriertem Silikat-Aerosil in Oktylzyanobiphenyl (8CB) untersucht. Die Ergebnisse zeigen, dass das bereits beobachtete „cross-over"-Verhalten von 8CB – Aerosil-Proben in Richtung auf die $3d$-XY-Universalitätsklasse als eine Kopplung der Dynamik des Aerosil-Gels an die Dynamik der Direktorfluktuationen im Flüssigkristall verstanden werden kann. Dieses Experiment legt die Schlussfolgerung nahe, dass das Aerosil-Gel diese Direktorfluktuationen widerspiegelt und dämpft, so dass durch das Unterdrücken der Direktorfluktuationen schließlich der Übergang zu einem reinen $3d$-XY-System erreicht wird.

Introduction

For several years now, it has been possible to obtain highly coherent high-intensity x-ray radiation from undulator sources at third-generation synchrotrons. The coherent flux can be used to investigate structure and dynamics down to atomic length scales. One way to do this is to analyze the intensity distribution and its variation in time of speckle patterns produced by a sample illuminated with coherent x-rays.

A random intensity distribution, called a speckle pattern, is formed when coherent or partially coherent light propagates through a medium with a randomly varying refractive index. Speckle phenomena have been investigated by many scientists since Newton [New87]. About a century ago, first Exner and then Laue observed speckle in Fraunhofer diffraction rings produced by light scattered from small particles on a glass plate [Exn77, Exn80, vL14]. A speckle pattern contains all the structural information about the sample medium that can be probed with a given wavelength. If the distribution of the refractive index evolves in time, the speckle pattern will change accordingly. Thus, observation of the temporal intensity fluctuations in the speckle pattern provides a direct measure of the time correlation function of the sample inhomogeneities.

The technique of x-ray intensity fluctuation spectroscopy (XIFS), also known as x-ray photon correlation spectroscopy (XPCS) or x-ray dynamic light scattering (XDLS), is especially suitable for the study of structure and dynamics of disordered systems on time scales down to milliseconds or even less. A large body of work has been done recently in this field by a number of scientists (see, e.g., [SMG$^+$91, CLY$^+$94, DPF$^+$95, MMS$^+$97, AGB$^+$98, MSL$^+$98, EGM$^+$99, PSK$^+$99, SLM$^+$99, LLS$^+$00, FDG$^+$00, LLMS00, SMT$^+$01]). Figure 1 shows the frequency range and length scales of the fluctuations that can be investigated with this technique in comparison to some other scattering techniques. However, most of the previous work was done in the range of 5 keV and higher photon energies. In the scope of this thesis, speckle techniques have been extended into the intermediate x-ray energy range of 1 to 4 keV. In this energy region, there are a number of important absorption edges. Figure 2 shows the elemental distribution of K-, L-, and M-edges between 1 and 4 keV. Elements that are important for biology (e.g., calcium, phosphorus, sulfur) and for industry (e.g., silicon, aluminum, rare earths) are amongst them. Besides allowing for element-specific studies, this energy region offers better coherence properties compared to higher energies, and a higher scattering cross section for lighter elements or

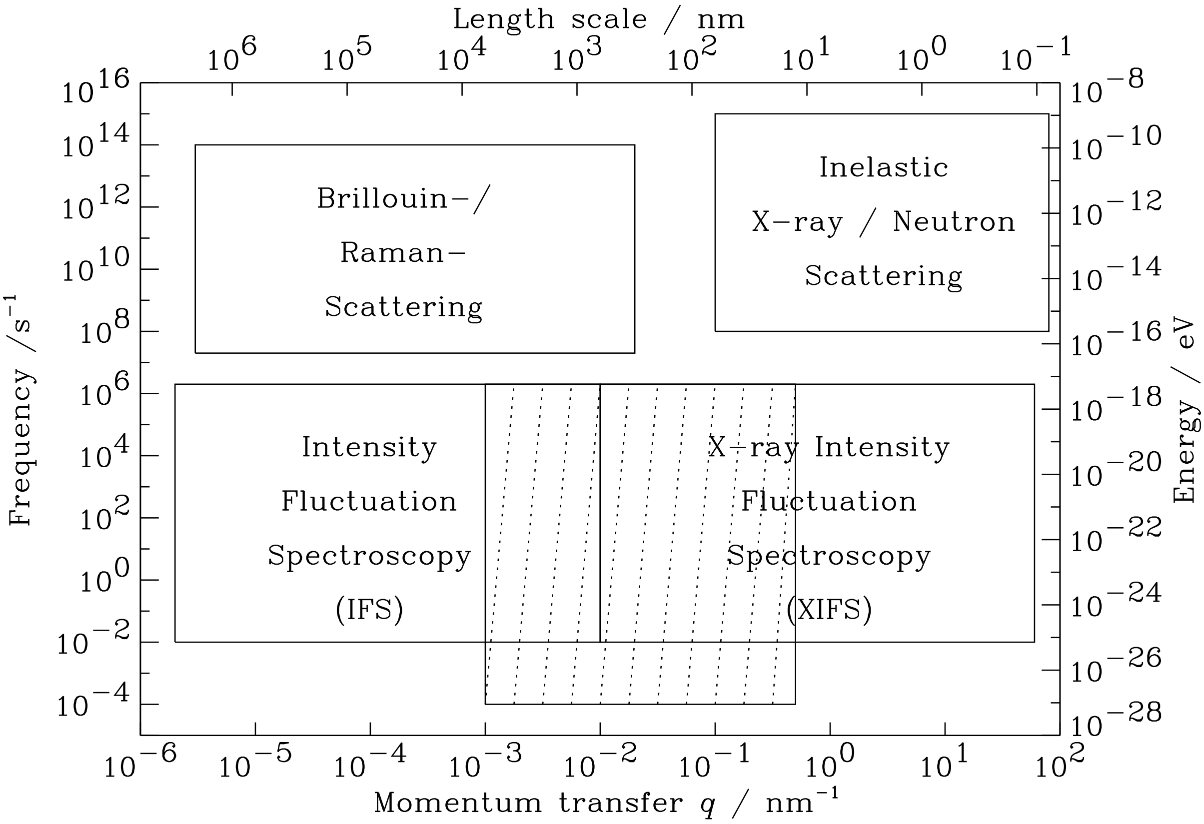

Figure 1: *Schematic of frequency range and length scales relevant for various coherent scattering techniques. The dashed area indicates time and lengths scales accessible with methods described in this thesis.*

thin samples. Compared to visible-light intensity fluctuation spectroscopy (IFS), it is possible to study thick opaque samples in transmission without significant multiple scattering and to access structures smaller than 200 nm. The dashed region in Fig. 1 indicates the frequency range and length scales that can currently be covered in the energy regime of 1 to 4 keV.

The outline of this thesis is as follows:
Chapter 1 describes the theory needed throughout this work. The first section introduces the phenomenon of coherence, a basic property of light needed to produce speckle. In Section 2 of Chapter 1, static speckle theory is presented. This theory is concerned with describing the statistics of static speckle patterns. The approach follows common descriptions, including some generalizations. Chapter 1.3 gives an introduction to the field of time correlation spectroscopy using speckle techniques. The last section of this chapter discusses the focusing of light by Fresnel zone plate lenses.

The experimental configuration used for this thesis is described in Chapter 2. After a description of the beamline at which the experiments were done, a commonly used pinhole setup and a focusing setup employing a Fresnel zone plate are introduced. The sample holder, especially

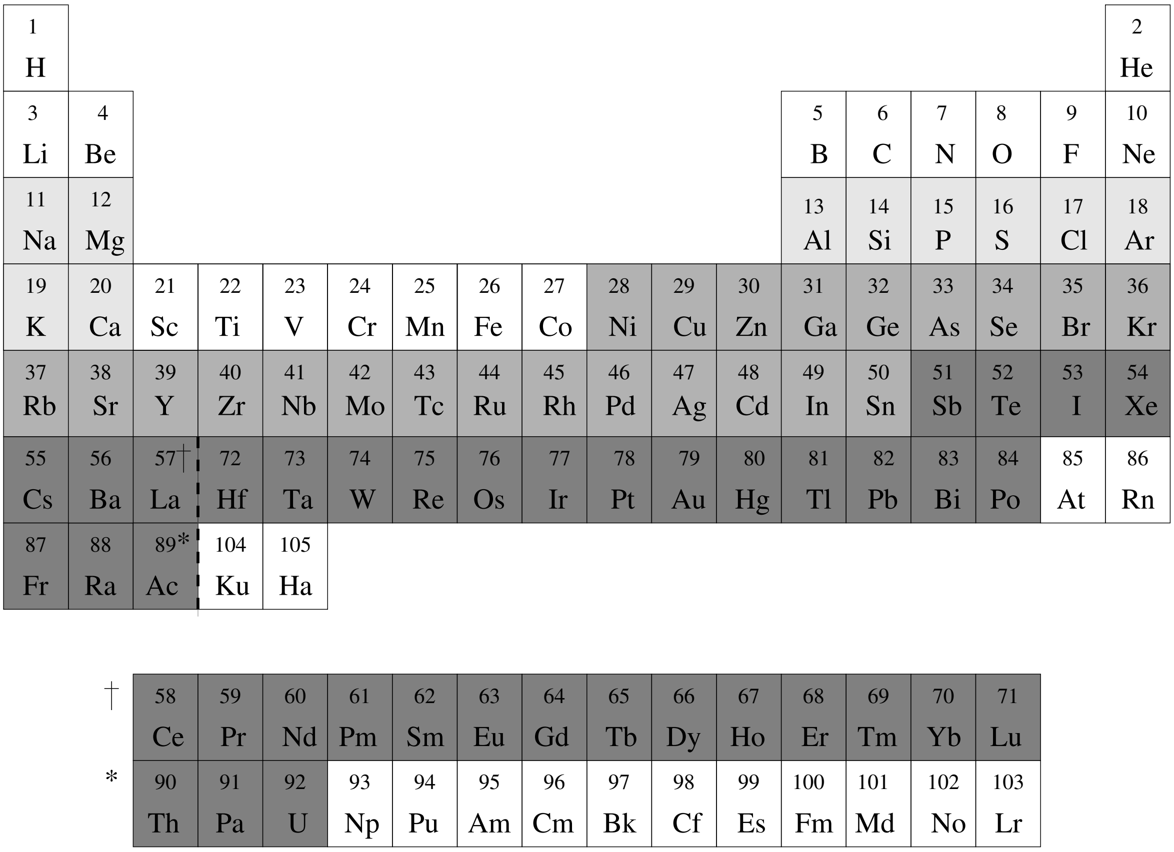

Figure 2: *Elemental distribution of absorption edges between* 1 *and* 4 *keV. The light gray shade indicates K-edges, the medium gray fields indicate L-edges and the dark gray fields, M-edges.*

designed for these experiments, is presented and some adaptions of common-type detectors are shown.

In the following chapters, the experiments and their results are presented and the findings discussed. Necessary extensions to the standard theory presented in Chapter 1 that were developed in the scope of this work are explained here. These chapters also cover the extensive data reduction methods applied to the raw two-dimensional data in order to extract the results.

Measurements to investigate advantages and disadvantages of the two setups described in Chapter 2 are shown and discussed in Chapter 3. Both experimental setups were tested under identical conditions, and their performances regarding speckle widths and contrast were analyzed. With modern x-ray zone plates capable of submicrometer focusing, the illuminated area on the sample can easily be orders of magnitude smaller than the thickness of the sample. For this case, an extension to standard theory has been developed in order to describe the observed decrease in speckle contrast.

Chapter 4 deals with the effect of sample-specific absorption edges on speckle contrast. Energy scans were performed across a sample-specific absorption edge, as well as, for comparison, an absorption edge of a filter material not present in the sample. The detected variation in speckle contrast was modeled and fit using fundamental theory.

In Chapter 5, experiments on the dynamic structure of a liquid-crystal-aerosil dispersion are presented. First the results from a static reference experiment performed to characterize the experimental setup are described. Then, time-series data recorded at different temperatures of the liquid-crystal-aerosil dispersion are analyzed to retrieve information on the dominant relaxation times in the system. These experiments demonstrate an application of x-ray intensity fluctuation spectroscopy in the intermediate x-ray energy region. The findings give revealing insight into the nature of the observed critical phenomena.

Finally, conclusions of the findings presented in this thesis are given in Chapter 6. This chapter also presents an outlook to further directions of study for a better understanding of the systems investigated in this thesis and similar dynamic systems using x-ray intensity fluctuation spectroscopy.

For ease of reading, in this thesis function arguments are always denoted with $(\ldots)$, whereas groupings of terms are done using $[\ldots]$. The magnitude of a vector $\vec{a}$, i.e., $|\vec{a}|$, is written as a.

Contents

List of Figures

List of Tables

Chapter 1

Theory

This chapter provides the theoretical basis for the following chapters of this thesis. It first introduces the concept of coherence and its implications for the experimental setup. Afterwards, basic statistical speckle theory as commonly known and used is presented. Consideration is given separately to static and dynamic behavior, the former basically used in Chapters 3 and 4, the latter introducing the theoretical approach needed for Chapter 5. For extensions to this theoretical basis, developed in the scope of this thesis in order to understand some of the experimental results, the reader is referred to the appropriate later chapters of this thesis. In the last section of this theory chapter, an introduction to Fresnel zone plates is given.

1.1 Coherence

The amplitudes and phases of light waves can undergo irregular fluctuations much too rapid for the eye or currently available detectors to follow. If the fluctuations in different parts of a beam from an extended source are correlated, the beam is said to be completely or partially *coherent*, depending on whether the correlation is complete or partial. Without such a correlation, the beam is said to be *incoherent*. When a coherent beam travels through an inhomogeneous medium, different parts of this beam may experience different phase shifts. The superposition of these parts can exhibit a phenomenon called *interference*, i.e., an intensity distribution that varies from point to point between maxima, which exceed the sum of the intensities of the different parts, and minima, which may be zero [BW97]. An incoherent beam traveling through the same medium will not produce such a pattern. The total intensity in this case will everywhere be the sum of the intensities of the different parts in the beam. The present work deals with one special kind of interference effect called speckle, which is described in the following section. The current section deals with determining to what degree the radiation can interfere, i.e., is coherent.

The experiments described in this thesis were done using an x-ray undulator source at a third-generation synchrotron (for details see Chapter 2). Such a source generates many radiative modes over an area primarily determined by the emittance of the electron beam in the storage ring. Wavefields originating from different electrons in the electron beam are incoherent with respect to each other. Thus, to good approximation, the undulator is an extended incoherent source.

However, according to the Van Cittert-Zernicke theorem [BW97], the beam from a small extended quasi-monochromatic* incoherent source develops a certain *complex degree of spatial coherence* μ with distance from the source, if observed under small angles, i.e., in the far-field of this source. μ describes the degree of correlation between complex wavefields present at two points of interest a distance $\Delta\vec{r} = [\Delta x, \Delta y]$ apart and at a distance R_{source} from the source. For a wave number k, μ is defined as

$$\mu(\Delta\vec{r}) = \frac{\exp(i\psi) \iint\limits_{\Sigma} I(\vec{\rho}) \, \exp\left(- i \frac{k}{R_{\text{source}}} \; \Delta\vec{r} \cdot \vec{\rho} \right) \mathrm{d}\vec{\rho}}{\iint\limits_{\Sigma} I(\vec{\rho}) \, \mathrm{d}\vec{\rho}} \quad , \tag{1.1}$$

where $\vec{\rho}$ is a position within the area Σ of the source. ψ represents the phase difference $k\,\Delta r = k|\Delta\vec{r}|$ and may be neglected when $k\,\Delta r \ll 2\pi$ [BW97]. $I(\vec{\rho})$ is the intensity of the source at point $\vec{\rho}$. Thus, if the linear dimensions Σ of the extended source and the distance Δr between the points of interest are small compared to the distance R_{source} of these points from the source, the *spatial degree of coherence* $|\mu|$ is equal to the absolute value of the normalized Fourier transform of the intensity distribution $I(\vec{\rho})$ of the source.

For a slit-shaped source, the spatial degree of coherence perpendicular to the orientation of the slit reduces to

$$\big|\mu(\Delta x)\big| = \left|\frac{\sin(\nu)}{\nu}\right| , \quad \nu = \Delta x \frac{ak}{2R_{\text{source}}} \quad , \tag{1.2}$$

where a is the full width of the slit. In this case, the criterion of 50% coherence between two points of interest separated by the distance Δx, i.e., $|\mu(\Delta x)| = 0.5$, yields the *transverse coherence length* $\Delta x_{50\%}$:

$$\Delta x_{50\%} = 1.895 \, \frac{2R_{\text{source}}}{ak} \quad . \tag{1.3}$$

The factor 1.895 is a consequence of the slit-type shape of the source.

*The condition for quasi-monochromaticity is given by $\frac{\Delta k}{k} \ll 1$, where k is the wave number.

1.2 Static Speckle Theory

Coherent illumination of a single scatterer produces a certain intensity distribution in the detector plane that can be calculated according to Huygens' principle [Goo68]. If a disordered system of scatterers is illuminated with temporally and spatially coherent light, all the scattered waves originating from the various scatterers interfere with each other, giving rise to speckle, a complex pattern of maxima and minima in the detection plane (Fig. 1.1). This pattern contains all the

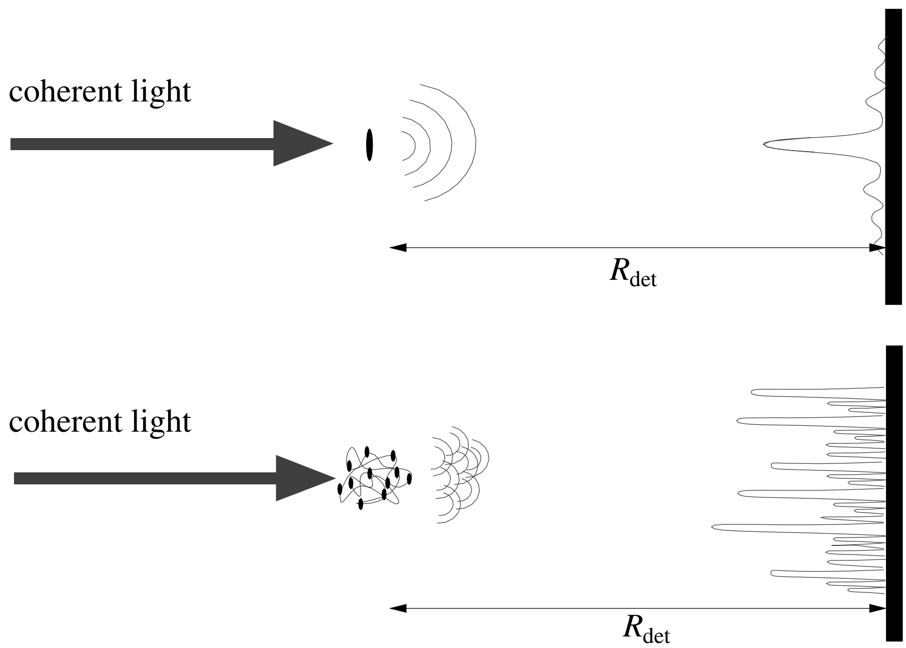

Figure 1.1: *Origin of speckle. A single scatterer (top) versus disordered scatterers (bottom).*

information about the structure of the sample that can be probed with a given wavelength. Full reconstruction of the sample structure from the speckle pattern, however, is complicated because the phase reconstruction is generally not unique. Some work has been done in this field (see, e.g., [VPLR97, RLV$^+$99, MCKS99]). So far, reconstruction was only possible for pure phase or pure absorption objects, however not in the general case.

The point of interest of the present work lies in the average or *statistical* properties of the sample, such as preferred orientations and correlation lengths or times, as well as sample-independent features originating from the experimental configuration. This section, specifically, deals with static properties. A description of the static speckle theory used to explain the measurements in Chapters 3, 4, and 5 is presented, following mostly the descriptions given by Goodman [Goo85] and Parry [Par84].

This theory is a far-field theory. The pattern is observed in the Fraunhofer regime of scattering, i.e., at a distance R_{det} from the object plane that is large enough so that length differences in the

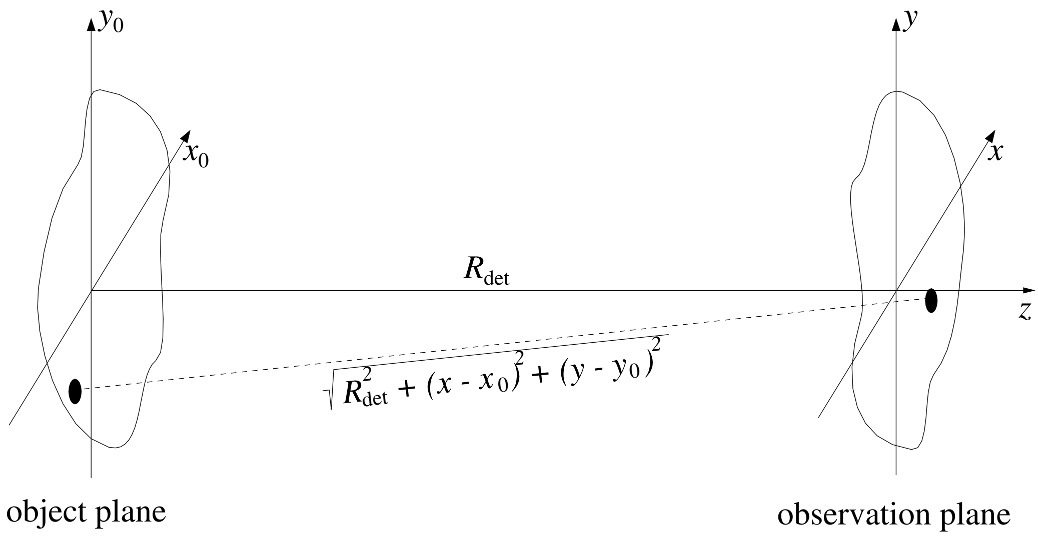

Figure 1.2: *Diffraction geometry.*

various paths from the extended object to a point in the plane of observation are small compared to $1/k$ and therefore can be neglected [Goo68, BW97]:

$$R_{\text{det}} \gg \frac{k}{2}\Big[x_0^2 + y_0^2\Big]_{\max} \quad , \tag{1.4}$$

where $[x_0, y_0]$ are the object coordinates as shown in Fig. 1.2, and R_{det} is the distance between the sample and the observation plane, i.e., the detector. In this regime, the intensity distribution in the plane of observation, $|A(\vec{r})|^2$, is basically given by the Fourier transform of the sample's response $A(\vec{r}_0)$ to the illumination by a wave front whose properties are given by $B(\vec{r}_0)$:

$$A(\vec{r}) = \frac{k\ \exp\big(ikR_{\text{det}}\big)}{2\pi i\, R_{\text{det}}} \iint B(\vec{r}_0)A(\vec{r}_0)\ \exp\big(-i\ \ \vec{q}\,(\vec{r})\cdot\vec{r}_0\big)\ \mathrm{d}r_0^3 \quad . \tag{1.5}$$

$\vec{q}$ is the momentum transfer $\vec{q} = \vec{k}_{\text{out}} - \vec{k}_{\text{in}}$, where $\vec{k}_{\text{in}}$ and $\vec{k}_{\text{out}}$ are the incident and the outgoing wave vector, respectively. $\vec{q}$ depends on the position $\vec{r} = [x, y, z]$ in the observation plane. $B(\vec{r}_0)$ contains the information about the extent of the volume of illumination, the distribution of the incoming wavefield within this volume if no sample was present, and the spatial degree of coherence of the incident wavefield.

The present interest lies in the statistical properties of the speckle pattern. A useful function for analyzing these properties is the normalized and baseline-subtracted spatial intensity autocorrelation function:

$$C_{\vec{r}}(\Delta\vec{r}) \equiv \frac{\big\langle\, I(\vec{r})\ \ I(\vec{r}+\Delta\vec{r})\,\big\rangle_{\vec{r}}}{\big\langle I(\vec{r})\,\big\rangle_{\vec{r}}\ \big\langle I(\vec{r}+\Delta\vec{r})\,\big\rangle_{\vec{r}}} - 1 \quad , \tag{1.6}$$

where $I(\vec{r})$ is the intensity at a point $\vec{r}$ in the speckle pattern. $\langle \ldots \rangle_{\vec{r}}$ denotes an average over a region around $\vec{r}$ that is large compared to the size of one speckle. $\Delta\vec{r}$ is the difference between the coordinates of two points within that region around $\vec{r}$. $C_{\vec{r}}(\Delta\vec{r})$ has a global maximum value at $\Delta\vec{r} = 0$. The width around this maximum is a measure for the average speckle width Ω in the region of interest. The speckle contrast Γ can be defined as the maximum of $C_{\vec{r}}(\Delta\vec{r})$, i.e., $C_{\vec{r}}(0)$, which is equal to the square of the intensity standard deviation $\sigma_{I,\vec{r}}$ in the region of interest around $\vec{r}$, divided by the square of the mean intensity:

$$\Gamma(\vec{r}) \equiv C_{\vec{r}}(0) = \frac{\sigma^2_{I,\vec{r}}}{\left[\left\langle I(\vec{r})\right\rangle_{\vec{r}}\right]^2} \quad . \tag{1.7}$$

For now, it will be assumed that

I) the sample can be divided into small scattering volumes $\mathrm{d}r_0^3$ so that each volume scatters with the *same* amplitude $\left|A_0\left(\vec{q}(\vec{r})\right)\right|$ determined by the short-range correlations in the sample;

II) the scattering regions $\mathrm{d}r_0^3$ are uncorrelated with respect to each other, so that the phase $\delta_0(\vec{r}_0)$ of the scattered field amplitude varies independently from region to region;

III) $\delta_0(\vec{r}_0)$ is equally distributed over 2π, i.e., the sample scatters with a white spectrum of phase distributions;

IV) the incoming beam is perfectly monochromatic.

Assumptions I to III separate length scales in the sample in a way that within the sample all correlations are much smaller than the illuminated volume and that the correlations in the sample follow circular complex Gaussian statistics. With these assumptions and expressing the intensity in terms of amplitudes, i.e., $I(\vec{r}) = |A(\vec{r})|^2$, the correlation term in Eq. (1.6) reduces to[†]

$$\begin{aligned} \Big\langle\, I(\vec{r}_1)I(\vec{r}_2)\, \Big\rangle_{\vec{r}} &= \Big\langle\, A(\vec{r}_1)A^*(\vec{r}_1)\, A(\vec{r}_2)A^*(\vec{r}_2)\, \Big\rangle_{\vec{r}} \\ &= \Big\langle\, |A(\vec{r}_1)|^2\, \Big\rangle_{\vec{r}} \Big\langle\, |A(\vec{r}_2)|^2\, \Big\rangle_{\vec{r}} + \Big|\Big\langle\, A(\vec{r}_1)A^*(\vec{r}_2)\, \Big\rangle_{\vec{r}}\Big|^2 \quad . \end{aligned} \tag{1.8}$$

With $\vec{r} = [\vec{r}_1 + \vec{r}_2]/2$ and $\Delta\vec{r} = \vec{r}_2 - \vec{r}_1$, Eq. (1.6) can be written as

$$C_{\vec{r}}(\Delta\vec{r}) = \frac{\left|\left\langle A(\vec{r}_1)A^*(\vec{r}_2)\right\rangle_{\vec{r}}\right|^2}{\left[\left\langle I(\vec{r})\right\rangle_{\vec{r}}\right]^2} \equiv \left|\gamma_A(\Delta\vec{r})\right|^2 \quad , \tag{1.9}$$

which defines $\gamma_A(\Delta\vec{r})$, the normalized mutual amplitude correlation function. $\gamma_A(\Delta\vec{r})$ is commonly written as a convolution of two components [STG98]: a part Ψ, describing the correlations

[†]This may be thought of as a consequence of the *central limit theorem* [Goo85].

given by the experimental setup, such as dimensions and coherence, and a sample part Φ, describing the correlations in the sample:‡

$$\gamma_A(\Delta\vec{r}) = \Psi(\Delta\vec{r}) \otimes \Phi(\Delta\vec{r}) \ . \tag{1.10}$$

$\Psi(\Delta\vec{r})$ is the Fourier transform of the autocorrelation function of the complex pupil function, i.e., a three-dimensional Fourier transform of the extension of the illuminated sample volume, times the degree of coherence present during the experiment. $\Phi(\Delta\vec{r})$ is the Fourier transform of the correlation properties of the electron density in the sample.

The separation of length scales assumed in assumptions I to III guarantees that the speckle statistics are characterized by the properties of the incident radiation and the illuminated sample volume, rather than the detailed structure of the sample. Mathematically, they allow the sample-part $\Phi(\Delta\vec{r})$ in Eq. (1.10) to be approximated by a δ-distribution. The phase and the amplitude part of $\gamma_A(\Delta\vec{r})$ can then truly be separated. If the illuminated sample volume is described by a three-dimensional Gaussian function, it follows:

$$\gamma_A(\Delta\vec{r}) = \exp\left(- \frac{\Delta q_z^2\, \sigma_T^2}{2} - \frac{\left[\Delta q_r^2 + \Delta q_\phi^2\right] \sigma_D^2}{2} \right) \left|\mu(D)\right| \ , \tag{1.11}$$

where σ_T is proportional to the thickness T of the sample and σ_D to the diameter D of the illuminated area on the sample. $|\mu(D)|$ is taken from Eq. (1.2). Δq_r , Δq_ϕ , and Δq_z are the cylindrical components of the difference in momentum transfer between the two points of interest in the speckle pattern separated by $\Delta\vec{r}$. With $\vec{q}$ given by

$$q_r = k\sin(2\theta) \ , \quad q_\phi = \phi \ , \quad \text{and} \quad q_z = k[\cos(2\theta) - 1] \ , \tag{1.12}$$

these components can be expressed as

$$\begin{aligned} \Delta q_r &= k\Big[\sin(2\theta_2) - \sin(2\theta_1)\Big] \ , \\ \Delta q_\phi &= \Delta\phi \ , \\ \Delta q_z &= k\Big[\cos(2\theta_2) - \cos(2\theta_1)\Big] \ , \end{aligned} \tag{1.13}$$

where $2\theta_1$ and $2\theta_2$ are the scattering angles of $\vec{r}_1$ and $\vec{r}_2$, respectively.

With Eqs. (1.9) and (1.11),

$$C_{\vec{r}}(\Delta\vec{r}) = \exp\Big(- \Delta q_z^2\, \sigma_T^2 - \left[\Delta q_r^2 + \Delta q_\phi^2\right] \sigma_D^2 \Big) \left|\mu(D)\right|^2 \ . \tag{1.14}$$

From this, Ω_azim and Ω_rad for the azimuthal and radial speckle full-width at half-maximum (FWHM) in reciprocal space can be calculated. To do this, it has to be taken into account that Δq_z

‡This is sometimes referred to as *Schell's theorem* [Sch61, Goo85]. It implies that the parts Ψ and Φ only depend on the difference between the coordinates of the two points of interest.

and Δq_r are functions of the angle 2θ between the direct beam and the scattered beam, whereas Δq_ϕ is not. Thus, Ω_{rad} depends on the angle 2θ, and Ω_{azim} is independent of that angle:

$$\Omega_{\mathrm{azim}} = \frac{2\sqrt{\ln(2)}}{\sigma_D} \ , \tag{1.15}$$

$$\Omega_{\mathrm{rad}}(2\theta) = \frac{2\sqrt{\ln(2)}}{\sqrt{\sigma_T^2 \sin^2(2\theta) + \sigma_D^2 \cos^2(2\theta)}} \ . \tag{1.16}$$

In this derivation (see Appendix A for details), Eq. (1.14) has been approximated by a Gaussian function.

The width of one speckle is thus determined by the dimensions of the illuminated volume in the sample and not by structural properties within this volume. This can be understood from the fact that the speckle pattern is related to the Fourier transform of the sample electron density distribution. Therefore, the largest correlation seen in the sample, i.e., the size of the illuminated volume in the sample, is transformed into the smallest correlation in the speckle pattern, i.e., the speckles. Assumptions I to III ensure that the sample correlation lengths are much smaller than the illuminated volume, thus producing only larger scale variations in the speckle pattern. As can be seen from the derivations in Appendix B, it turns out that Ω_{azim} and Ω_{rad} depend not only on the size but also on the shape of the illuminated volume in the sample. The circular profile of the beam on the sample produces an Airy pattern[§] for the intensity distribution in reciprocal space. The illuminated sample volume in direction of the beam is of a slit type, producing the square of a sinc function[¶] in reciprocal space. Comparing a Gaussian function with an Airy pattern or the square of a sinc function, respectively, σ_D and σ_T result from the beam diameter D and sample thickness T by scaling with the following factors:

$$\sigma_D \approx \frac{\sqrt{\ln(2)}\, D}{1.03\,\pi} \approx 0.26\, D \ , \qquad \sigma_T \approx \frac{\sqrt{\ln(2)}\, T}{0.89\,\pi} \approx 0.30\, T \ . \tag{1.17}$$

The speckle contrast $\Gamma(\vec{r})$, derived from Eq. (1.14), is equal to the square of the degree of coherence $|\mu(D)|^2$.

Now, assumption IV requiring perfect monochromaticity will be relaxed. Instead, quasi-monochromatic light will be considered. The conditions for quasi-monochromaticity are given if

$$\frac{\Delta k}{k} \ll 1 \tag{1.18}$$

and if the maximum path length difference in the experiment is much less than the longitudinal coherence length $\lambda^2/\Delta\lambda$ [Goo85], where $\lambda = 2\pi/k$ is the wavelength. Instead of the intensity $I(\vec{r})$ used previously, the *spectrally integrated intensity* I_W has to be introduced:

$$I_W(\vec{r}) = \int W(k) I(k, \vec{r})\, \mathrm{d}k \ , \tag{1.19}$$

[§] $\mathrm{Airy}(x) \equiv \left[2\frac{J_1(x)}{x}\right]^2$, where J_1 stands for the Bessel function of first kind, order one.

[¶] $\mathrm{sinc}(x) \equiv \frac{\sin(x)}{x}$.

where $W(k)$ is the spectral intensity distribution, or *spectral response function* of the source. Here, 'source' stands for the combination of all beamline components upstream of the sample. Now, $\Delta\vec{q}$ is given by

$$\Delta\vec{q} = \vec{q}_2(k_2, \vec{r}_2) - \vec{q}_1(k_1, \vec{r}_1) \quad , \tag{1.20}$$

where k_1, k_2 and $\vec{r}_1, \vec{r}_2$ are the two wave numbers and the two corresponding locations on the detector, respectively. In order to write the explicit dependence of $C_{\vec{r}}$ on $\Delta\vec{r}$, the normalized mutual amplitude correlation function γ_A has to be written as $\gamma_A(k_1, k_2, \vec{r}_1, \vec{r}_2)$. A two-dimensional convolution with the distribution of wave numbers k present in the experiment yields the auto-correlation function $C_{\vec{r},W}(\Delta\vec{r})$:

$$C_{\vec{r},W}(\Delta\vec{r}) = \frac{\iint W(k_1)W(k_2)\ \left|\gamma_A(k_1, k_2, \vec{r}_1, \vec{r}_2)\right|^2\ \big\langle I(k_1, \vec{r})\big\rangle_{\vec{r}}\big\langle I(k_2, \vec{r})\big\rangle_{\vec{r}}\ \mathrm{d}k_1\ \mathrm{d}k_2}{\left[\int W(k)\ \langle I(k, \vec{r})\rangle_{\vec{r}}\ \mathrm{d}k\right]^2} \ . \tag{1.21}$$

Under the conditions for quasi-monochromaticity, $\langle I(k, \vec{r})\rangle_{\vec{r}}$ will usually vary slowly in k over the width of the spectral response function W [BS91] and thus can be considered as a constant and be removed fom the integrals in Eq. (1.21) to give

$$C_{\vec{r},W}(\Delta\vec{r}) = \iint \widetilde{W}(k_1)\widetilde{W}(k_2)\ \left|\gamma_A(k_1, k_2, \vec{r}_1, \vec{r}_2)\right|^2\ \mathrm{d}k_1\ \mathrm{d}k_2 \quad , \tag{1.22}$$

where $\widetilde{W}(k) = W(k) / \left[\int W(k)\,\mathrm{d}k\right]$ is the normalized spectral response function. $C_{\vec{r},W}(\Delta\vec{r})$ is now a two-dimensional convolution of γ_A with this normalized spectral response function. If $W(k)$ is assumed to be a Gaussian function

$$\widetilde{W}(k) = \frac{1}{\sqrt{2\pi\sigma_k^2}}\ \exp\left(-\frac{[k - k_0]^2}{2\sigma_k^2}\right) \quad , \tag{1.23}$$

the integrals in Eq. (1.22) can be solved analytically, in a straightforward manner, for the width and the contrast of the speckles, as shown in Appendix C. Ω_{azim} stays unaffected by the wave number smearing. The radial width Ω_{rad} and the speckle contrast Γ , however, are affected:

$$\Omega_{\mathrm{rad},W}(2\theta) \;=\; 2\sqrt{\ln(2)}\sqrt{\frac{1\,+\,4\sigma_T^2\sigma_k^2\big[1-\cos(2\theta)\big]^2\,+\,4\sigma_D^2\sigma_k^2\sin^2(2\theta)}{4\sigma_T^2\sigma_D^2\sigma_k^2\big[1-\cos(2\theta)\big]^2\,+\,\sigma_T^2\sin^2(2\theta)\,+\,\sigma_D^2\cos^2(2\theta)}} \ , \tag{1.24}$$

$$\Gamma_W(2\theta) \;=\; \left|\mu(D)\right|^2\sqrt{\frac{1}{1\,+\,4\sigma_T^2\sigma_k^2\big[1-\cos(2\theta)\big]^2\,+\,4\sigma_D^2\sigma_k^2\sin^2(2\theta)}} \ . \tag{1.25}$$

The effect on Ω_{rad} is very small in a wide range of monochromaticity, which is $\propto k/\sigma_k$. However, the speckle contrast of the pattern decreases noticeably with a decrease in monochromaticity [AGB+98].

In addition, resolution effects have to be considered: the detector at distance R_{det} from the sample is usually not an ideal point detector but integrates over an area with linear dimension D_{det} . The source is not a point source either, but has a finite linear dimension D_{source} at a distance R_{source} from the sample. Therefore, the corrected speckle widths and speckle contrast are

$$\Omega_{\text{corr}} = \Omega\sqrt{1 + r_{\text{det}}^2 + r_{\text{source}}^2} \tag{1.26}$$

and

$$\Gamma_{\text{corr}} = \Gamma\frac{1}{\sqrt{1 + r_{\text{det}}^2 + r_{\text{source}}^2}} \quad , \tag{1.27}$$

with the contributions r_{det} and r_{source} given by

$$r_{\text{det}} = \frac{D_{\text{det}}}{D_{\text{speckle}}} \quad , \quad r_{\text{source}} = \frac{D_{\text{source}}/R_{\text{source}}}{D_{\text{speckle}}/R_{\text{det}}} \quad , \tag{1.28}$$

where D_{speckle} is the speckle size in real space without resolution corrections. Here, Ω denotes either Ω_{azim} or Ω_{rad} .

1.3 Time Correlations

A speckle pattern originating from a temporally varying distribution of the refractive index in a sample will vary in time. The time correlation constants or relaxation times of the sample material are reflected in the fluctuations of the speckle pattern.[‖] Thus, the observation of the temporal intensity fluctuations at a given q-position in the speckle pattern provides a measure of the time correlation function for the respective spatial correlation length $2\pi/q$ in real space. This technique is well established in the field of laser light scattering, whereas its introduction to the x-ray regime is still very recent.

For the statistical analysis of such data, the normalized baseline-subtracted *temporal* autocorrelation function provides a useful tool. It is given by

$$g_2(\tau, \vec{q}) \equiv \frac{\left\langle\, I(t, \vec{q})\, I(t + \tau, \vec{q})\,\right\rangle_t}{\left[\left\langle I(t, \vec{q})\right\rangle_t\right]^2} - 1 \quad , \tag{1.29}$$

where $\vec{q}$ gives the location of interest in reciprocal space (Eq. (1.12)), τ is the lag time, and $\langle \ldots \rangle_t$ denotes a time average.

[‖] Time correlation constants associated with the experimental setup, e.g., vibrations, are often present in the temporal fluctuations of the speckle pattern as well. Measures have to be taken to eliminate or characterize those contributions.

This function can assume values between 0 and 1, having the maximum value at $\tau = 0$. Therefore, the value of g_2 for $\tau = 0$ is a measure for the temporal *fluctuation contrast* Γ_{fl} of the time series. For static speckles, all patterns $I(t, \vec{q})$ of a temporal series are identical and no longer time dependent:

$$g_2(\tau, \vec{q}) = \frac{\langle I^2(\vec{q}) \rangle_t}{\left[\langle I(\vec{q}) \rangle_t\right]^2} - 1 = \frac{I^2(\vec{q})}{I^2(\vec{q})} - 1 = 0 \ , \tag{1.30}$$

yielding zero fluctuation contrast. For strong fluctuations, i.e., fluctuations that occur throughout the sample and not only in a few nonrepresentative locations, $\Gamma_{\text{fl}} = 1$. Small but nonzero fluctuation contrast is due to one of the following three conditions:

Speckles may be *blurred in space*. The cause of this is poor speckle contrast Γ_{corr} as described in the previous section (Eqs. (1.25) and (1.27)), i.e., the experiment was done with poor monochromaticity or poor spatial coherence. The superposition of several speckles at the same time but in slightly different locations is detected. If dynamics are studied, such a limited speckle contrast results in an overall decrease in fluctuation contrast:

$$\Gamma_{\text{fl}} \leq \Gamma_{\text{corr}} \ . \tag{1.31}$$

Speckles may be *blurred in time*. The cause of this lies in temporal fluctuations that are faster than the integration time of the detector. The superposition of speckles that occur at different times in different places is recorded with the detector. In this case, the calculated speckle contrast Γ_{corr}, which does not account for dynamics in the sample, is much higher than that observed. Consistent with Eq. (1.31), Γ_{fl} can be written as:

$$\Gamma_{\text{fl}}(2\theta) = \alpha \, \Gamma_{\text{corr}}(2\theta) \, \phi(\tau = 0) \ , \tag{1.32}$$

where α corrects for distortion of the data due to finite sampling time [Pat85]. It assumes values between 0 and 1.

$\phi(\tau) \propto g_2(\tau)$ describes the time correlations in the sample. For strong fluctuations, i.e., fluctuations that occur throughout the sample and not only in a few nonrepresentative locations, $\phi(0) = 1$. However, temporal fluctuations in the sample may consist of *only small fractions* of the sample material fluctuating or the scale of the fluctuations may be *smaller than what can be detected* with the used wavelength. Even though the speckle patterns might exhibit high speckle contrast in every single detected pattern, the series will yield a small fluctuation contrast. This is the third possible origin of reduced fluctuation contrast. The limiting case is the totally static pattern (Eq. (1.30)).

Because of the different origins of the factors that determine Γ_{fl}, a way to find the cause of an observed $\Gamma_{\text{fl}} < 1$ is to compare Γ_{fl} with the speckle contrast Γ_{corr} in a single speckle pattern of the time series. If the measured speckle contrast agrees with the calculations of Γ_{corr}, then $\alpha = 1$. The reason for the reduced fluctuation contrast must be a small value of $\phi(0)$.

Physical Process	Theoretical Form of $g_2(\tau, q)$
Translational diffusion of single species	$A + B \exp\big(-2Dq^2\tau\big)$
Translational diffusion in polydisperse samples	$A + \Big[\int B(M)\exp\big(-D(M)q^2\tau\big)\,\mathrm{d}M\Big]^2$
Rotational diffusion of single species	$A + \Big[\sum_{l=\text{even}} B_l \exp\big(-\big[Dq^2 + l[l+1]/\tau_R\big]\tau\big)\Big]^2$
Flexing molecules	$A + \Big[\sum_{m,n} P_{m,n}\exp\big(-[Dq^2 + m/\tau_n]\tau\big)\Big]^2$
Motile objects	$A + B\exp\big(-\tau^2/2\tau_d^2\big)$
Directed motion; propagating waves on a surface	$A + B\exp(-\tau/\tau_d)\cos(\omega\tau)$

Table 1.1: *Overview of theoretical forms of correlation functions corresponding to various physical processes [For85].*

Besides the strength of the fluctuations reflected in the fluctuation contrast, the time structure of the fluctuations, especially its relaxation with time is of interest. Various forms of relaxations are predicted for different sample systems. A brief general classification of forms is given in Table 1.1. For further details see, e.g., [For85].

From Table 1.1, it is obvious that, for a wide range of physical processes, the temporal autocorrelation function g_2 follows exponential forms. A single-exponential form of $g_2(\tau)$ can be analyzed in terms of a single relaxation time τ_d. The cause for non-single-exponential forms of $g_2(\tau)$ may be a distribution $w_{\bar{\tau}_d}$ of relaxation times around an average relaxation time $\bar{\tau}_d$:

$$g_2(\tau) = \Gamma_{\text{fl}}\left[\int w_{\bar{\tau}_d}(\tau_d)\ \exp(-\tau/\tau_d)\ \mathrm{d}\tau_d\right]^2 \quad . \tag{1.33}$$

In practice it is found that the data can often be described very well by the empirical Williams-Watts relaxation function, sometimes called a stretched-exponential function [Ste93]:

$$g_2(\tau) = \Gamma_{\text{fl}}\exp\big(-2[\tau/\tau_d]^\beta\big) \quad , \tag{1.34}$$

with $0 < \beta \leq 1$. Because of Eq. (1.33), the square-root of Eq. (1.34) can be interpreted as the Laplace transform of the distribution $w_{\bar{\tau}_d}$ of relaxation processes in the experiment. The average relaxation time for the Williams-Watts function is found to be

$$\bar{\tau}_d = \frac{\tau_d}{\beta}\,\mathbf{\Gamma}\left(\frac{1}{\beta}\right) \quad , \tag{1.35}$$

with the gamma function $\mathbf{\Gamma}(x)$. This allows for a meaningful interpretation of the data with only two parameters: β and $\bar{\tau}_d$. β is a measure for the width of the distribution $w_{\bar{\tau}_d}$ of relaxation times, and $\bar{\tau}_d$ is the average relaxation time.

If the measured g_2 follows Eq. (1.34) with $\beta > 1$, the interpretation in terms of a distribution of single-exponential relaxations cannot be done anymore. More complicated forms of relaxations (for examples, see Table 1.1) are then involved in the total measured relaxation process.

1.4 Zone Plates

In this section, the theory of x-ray focusing using Fresnel zone plates will be described (see, e.g., [Mic86]). Specifically, the diameter of the beam near the *first-order* focal plane of a zone plate will be calculated. Here, the beam diameter is defined as the diameter of the disk parallel to this focal plane through which 50% of the time-averaged total energy passes. In the following, the term focal plane will always refer to the first-order focal plane of the zone plate unless otherwise specified.

A Fresnel zone plate is a device capable of focusing light by diffraction. It consists of alternating transparent and opaque annular zones (amplitude zone plate) or alternating transparent and phase-shifting zones (phase zone plate). In reality, almost all zone plates for x-rays lie between these two limiting cases. The zone widths become finer with increasing radius, maintaining an optical path length difference between adjacent zones of exactly $\lambda/2$. This construction principle results in a sequence of focii at distance f_m from the zone plate with

$$f_m = \frac{ka\delta_{\mathrm{oz}}}{m\pi} \quad , \tag{1.36}$$

where δ_{oz} is the width of the outermost zone and a is the radius of the zone plate.

Figure 1.3 shows the geometry for the following derivation. It is useful to introduce dimensionless quantities u and v by transforming the coordinates r and z:

$$u = k\,\frac{a^2}{f^2}\,z, \qquad v = k\,\frac{a}{f}\,r \quad , \tag{1.37}$$

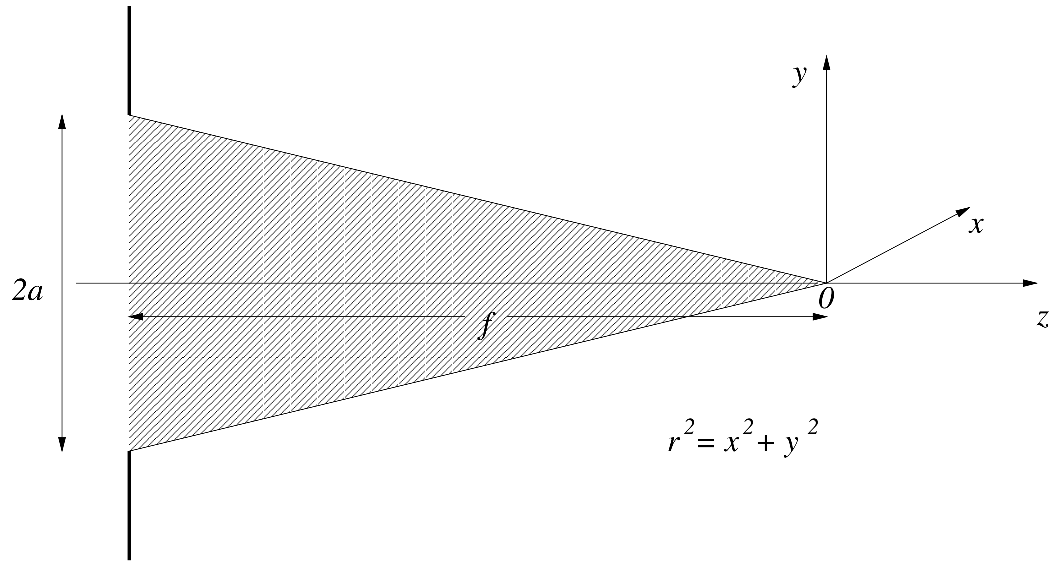

Figure 1.3: *Diffraction geometry used for the calculations. The dashed region shows the geometrical cone between the aperture and the first-order focal plane at distance f.*

where $f \equiv f_1$ is the distance of the first-order focus.

A zone plate can be considered to be a stack of transmissive and opaque apertures of radius a_n. For one such aperture, the wavefront disturbance at a point $[u_n, v_n]$ close to the focal plane is given by [BW97]

$$\begin{aligned} A(u_n, v_n) &= -i\, A_0\, k\, \frac{a_n^2}{f^2} \exp\left(i \tfrac{f^2}{a_n^2} u_n\right) \int_0^1 J_0(v_n \rho) \exp\left(-\tfrac{i}{2} u_n \rho^2\right) \rho \, \mathrm{d}\rho \\ &= -i\, \frac{A_0}{2}\, F_n \Big[C(u_n, v_n) - iS(u_n, v_n) \Big] \ , \end{aligned} \tag{1.38}$$

with

$$\begin{aligned} C(u,v) &= \frac{\cos\left(\frac{1}{2}u\right)}{\frac{1}{2}u} U_1(u,v) + \frac{\sin\left(\frac{1}{2}u\right)}{\frac{1}{2}u} U_2(u,v) \ , \\ S(u,v) &= \frac{\sin\left(\frac{1}{2}u\right)}{\frac{1}{2}u} U_1(u,v) - \frac{\cos\left(\frac{1}{2}u\right)}{\frac{1}{2}u} U_2(u,v) \ , \end{aligned} \tag{1.39}$$

and

$$F_n = k\, \frac{a_n^2}{f^2} \ . \tag{1.40}$$

A_0/f is the amplitude incident on a point within the aperture, and J_0 is the Bessel function of first kind and zero order. U_l is a *Lommel function* given by

$$U_l(u,v) = \sum_{s=0}^{\infty} [-1]^s \left[\frac{u}{v}\right]^{l+2s} J_{l+2s}(v) \ . \tag{1.41}$$

In order to determine the total amplitude near the focal plane, the contributions $A(u_n, v_n)$ arising from the apertures of radii a_n have to be alternately added and subtracted. This yields the intensity distribution $I_{\mathrm{ZP}}(u,v)$ of a zone plate with N zones:

$$\begin{aligned} I_{\mathrm{ZP}}(u,v) &= \left| \sum_{n=1}^{N} [-1]^n A(u_n, v_n) \right|^2 \\ &= \frac{|A_0|^2}{4} \left[\left[\sum_{n=1}^{N} [-1]^n F_n\, C(u_n, v_n) \right]^2 + \left[\sum_{n=1}^{N} [-1]^n F_n\, S(u_n, v_n) \right]^2 \right] \ . \end{aligned} \tag{1.42}$$

To simplify further calculations, it will now be shown that, for a large number of zones N, the intensity distribution in the focal plane of a zone plate approaches that of a perfect lens. This treatment follows Michette [Mic86], but corrects for misprints present in some of the formulas in this reference.

The focal plane is located at $u = 0$. From Eq. (1.41), it can be shown, that

$$\begin{aligned} \lim_{u\to 0}\left(\frac{U_1(u,v)}{u}\right) &= \frac{J_1(v)}{v} \quad , \\ \lim_{u\to 0}\left(\frac{U_2(u,v)}{u}\right) &= 0 \quad . \end{aligned} \tag{1.43}$$

In this limit and using Eqs. (1.37), (1.39), and (1.40), $I_{\mathrm{ZP}}(0,v)$ reduces to

$$\begin{aligned} I_{\mathrm{ZP}}(0,v) &= |A_0|^2 \left[\sum_{n=1}^{N}[-1]^n F_n \frac{J_1(v_n)}{v_n}\right]^2 \\ &= \frac{|A_0|^2 a^4 k^2}{f^4 v^4}\left[\sum_{n=1}^{N}[-1]^n J_1(v_n)\, v_n\right]^2 \quad . \end{aligned} \tag{1.44}$$

For a zone plate, the relation between any zone of radius a_n and the first zone is given by** $a_n^2 = n a_1^2$, and therefore $v_n^2 = n v_1^2$. Inserting this into Eq. (1.44) yields

$$I_{\mathrm{ZP}}(0,v) = 4I_0\left[\sum_{n=1}^{N}[-1]^n\, J_1\left(\sqrt{n}\,v_1\right)\frac{\sqrt{n}}{N}\frac{1}{v_1}\right]^2 \quad , \tag{1.45}$$

with

$$I_0 = \left[\frac{k}{2}\frac{a^2}{f^2}\,|A_0|\right]^2 \tag{1.46}$$

being the total intensity at $u = v = 0$, and $v = \sqrt{N}\,v_1$.

Equation (1.45) is plotted in Fig. 1.4 for different values of N. For comparison, the intensity distribution in the focal plane of a perfect lens [BW97],

$$I(0,v) = I_0\left[\frac{2J_1(v)}{v}\right]^2 \quad , \tag{1.47}$$

is shown as well. The term in square brackets is called the Airy pattern of the dimensionless quantity v. With increasing N, $I_{\mathrm{ZP}}(0,v)$ rapidly approaches the Airy pattern. To illustrate the relative error introduced by using Eq. (1.47) instead of Eq. (1.45), Fig. 1.5 shows the radius $r_{0,\mathrm{ZP}}$ of the first intensity minimum for a zone plate with N zones, divided by the radius $r_{0,\mathrm{Lens}}$ of the first intensity minimum of a perfect lens, as a function of N. This ratio rapidly approaches 1 with increasing N.

If N is large enough, the intensity distribution can thus be approximated by that of a perfect lens. The intensity distribution *in* the focal plane of a lens as given by the Airy pattern yields a FWHM diameter of D_{diffr}:

$$2v = k\,\frac{a}{f}\,D_{\mathrm{diffr}} \approx 3.23 \qquad \Rightarrow \qquad D_{\mathrm{diffr}} \approx 1.03\,\frac{\pi f}{ak} \quad , \tag{1.48}$$

**Strictly speaking, this holds only if $N \ll 4f/\lambda$, which is usually the case, and if a_0 is 0. If $a_0 \neq 0$, the validity of the calculations can be recovered by adding an offset to the lower limit of the sum over n.

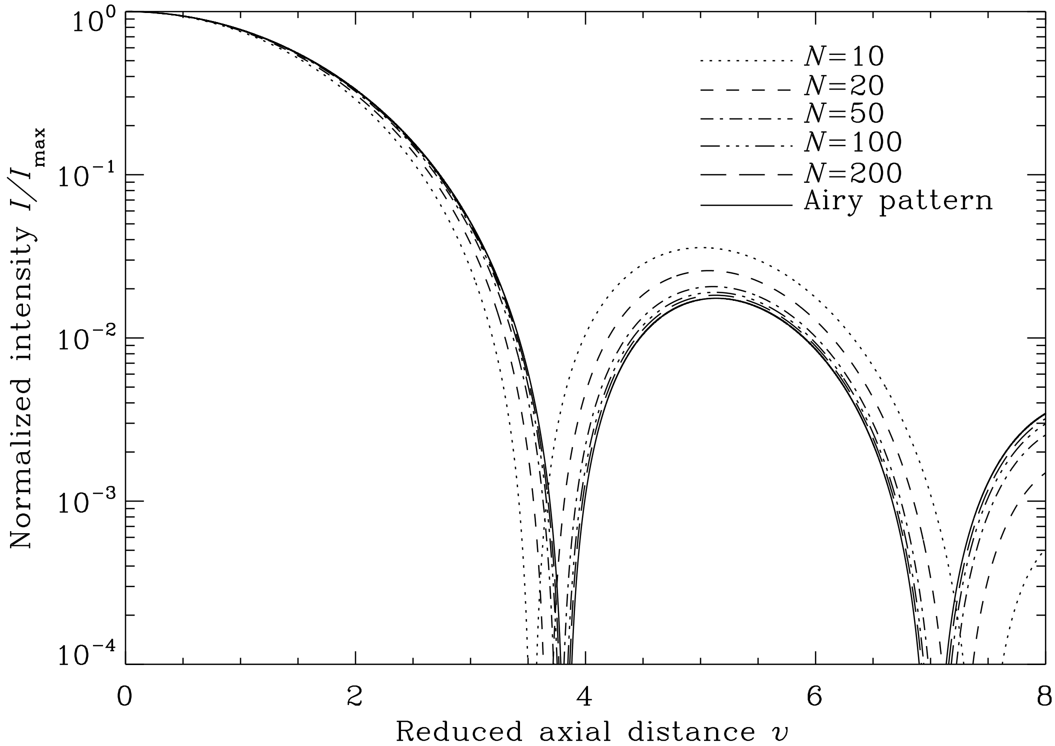

Figure 1.4: *Normalized intensity distribution in the focal plane of a zone plate for different numbers of zones N as a function of the reduced distance v from the optical axis. The Airy pattern distribution for a perfect lens is plotted as a solid line.*

which with Eq. (1.36) leads to

$$D_{\mathrm{diffr}} \approx 1.03\,\delta_{\mathrm{oz}} \quad . \tag{1.49}$$

To calculate the beam diameter *near* the focal plane, let E be the total energy incident onto the lens. Then the fraction L of the time-averaged total energy that passes through a circle of radius r_0 parallel to the focal plane of a lens is given by

$$\begin{aligned} L(u, v_0) &= \frac{1}{E}\int_0^{r_0}\int_0^{2\pi} I(u,v)\,r\,\mathrm{d}r\mathrm{d}\psi \\ &= \frac{1}{2I_0}\int_0^{v_0} I(u,v)\,v\,\mathrm{d}v \quad , \end{aligned} \tag{1.50}$$

where

$$v_0 = k\,\frac{a}{f}\,r_0 \quad . \tag{1.51}$$

$I(u,v)$ is given by the two equivalent Lommel – expressions:

$$I(u,v) = I_0\left[\frac{2}{u}\right]^2\left[U_1^2(u,v) + U_2^2(u,v)\right] \tag{1.52}$$

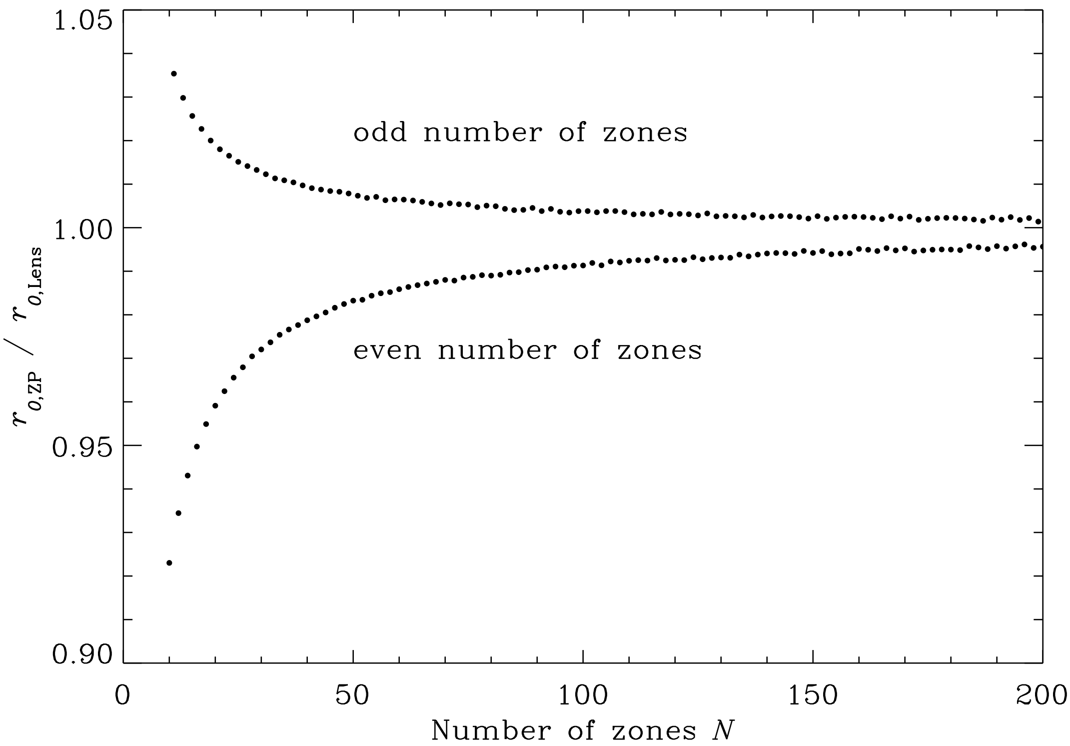

Figure 1.5: *Radius $r_{0,\mathrm{ZP}}$ of the first intensity minimum in the focal plane of a zone plate with N zones divided by the radius $r_{0,\mathrm{Lens}}$ of the first intensity minimum of a perfect lens.*

and

$$I(u,v) = I_0 \left[\frac{2}{u}\right]^2 \left[1 + V_0^2(u,v) + V_1^2(u,v) \right. \\ \left. - 2V_0(u,v)\cos\left(\frac{1}{2}\left[u+\frac{v^2}{u}\right]\right) - 2V_1(u,v)\sin\left(\frac{1}{2}\left[u+\frac{v^2}{u}\right]\right)\right] \ , \tag{1.53}$$

where Eq. (1.52) was derived in analogy to Eqs. (1.38) and (1.42). Depending on the region of interest (i.e., $u \leq v$ or $u \geq v$), either Eq. (1.52) or Eq. (1.53) turns out to be more convenient for calculations. U_l was already defined above in Eq. (1.41), and V_l is the other Lommel function given by:

$$V_l(u,v) = \sum_{s=0}^{\infty} [-1]^s \left[\frac{v}{u}\right]^{l+2s} J_{l+2s}(v) \ . \tag{1.54}$$

Expanding Eq. (1.50) into a series involving Bessel functions, two resulting expressions for $L(u,v)$ can be found [Wol51, Foc56], one of which again is advantageous for calculations in the case of $v \geq u$ and the other in the case of $v \leq u$. For $|v/u| \geq 1$, i.e., for disks that extend beyond the geometrical cone of the lens indicated in Fig. 1.3, $L(u,v)$ is given by

$$L(u,v) = 1 - \sum_{s=0}^{\infty} \frac{[-1]^s}{2s+1} \left[\frac{u}{v}\right]^{2s} Q_{2s}(v) \ , \tag{1.55}$$

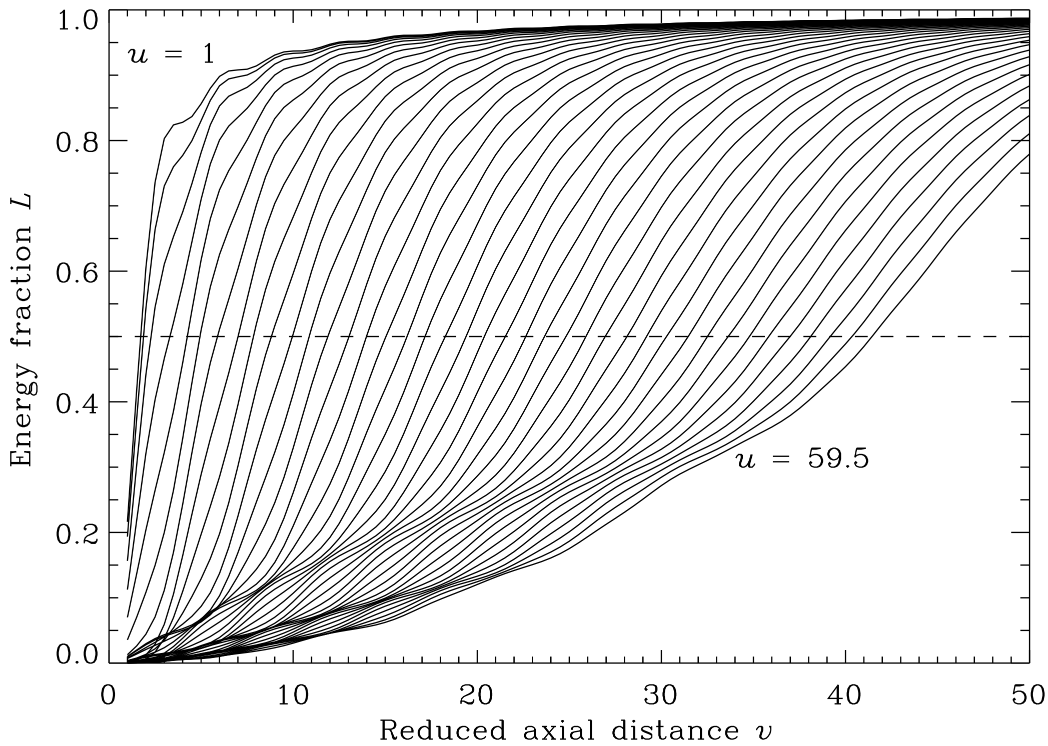

Figure 1.6: *Fraction L of the total energy passing through a disk of the reduced radius* v *around the optical axis of a lens at various reduced distances* u *from the focal plane. The lines from left to right represent the calculations for values of* $1.0 \leq u \leq 59.5$ *with steps of* $\Delta u = 1.5$. *The dashed line indicates the* 50%*-level.*

with

$$Q_{2s}(v) = \sum_{p=0}^{2s} \big[-1\big]^p \big[J_p(v)J_{2s-p}(v) + J_{p+1}(v)J_{2s+1-p}(v)\big] \quad . \tag{1.56}$$

And for $|v/u| \leq 1$, i.e., for disks that are confined within the geometrical cone of the lens (see Fig. 1.3), $L(u,v)$ is found to be

$$\begin{aligned} L(u,v) = &\left[\frac{v}{u}\right]^s \left[1 + \sum_{s=0}^{\infty} \frac{[-1]^s}{2s+1}\left[\frac{v}{u}\right]^{2s} Q_{2s}(v)\right] \\ &- \frac{4}{u}\left[Y_1(u,v)\cos\left(\frac{1}{2}\left[u + \frac{v^2}{u}\right]\right) + Y_2(u,v)\sin\left(\frac{1}{2}\left[u + \frac{v^2}{u}\right]\right)\right] \quad , \end{aligned} \tag{1.57}$$

with

$$Y_l(u,v) = \sum_{s=0}^{\infty}[-1]^s[l+2s]\left[\frac{v}{u}\right]^{l+2s} J_{l+2s}(v) \quad . \tag{1.58}$$

Figure 1.6 shows the fraction of the energy within a disk of radius v at different distances u from the focal plane. These calculations were done numerically with an approximation to the infinite sums of $s \leq 70$, showing good convergence. The resulting values of $2\,v_{0.5}$ for $L = 0.5$ are a measure for the FWHM beam diameter at distance u from the focal plane. Equations (1.37) allow a back transform into experimental coordinates.

In addition to this beam diameter, the image size D_{image} of the source focused by the lens has to be considered. Let R_{sl} be the distance between the source and the lens and R_{li} the distance between the lens and the image of the source. Then, according to the *thin lens* equation

$$\frac{1}{f} = \frac{1}{R_{\mathrm{li}}} + \frac{1}{R_{\mathrm{sl}}} \quad , \tag{1.59}$$

the image size D_{image} of a source of size D_{source} is given by

$$D_{\mathrm{image}} = \frac{R_{\mathrm{li}}}{R_{\mathrm{sl}}} D_{\mathrm{source}} \quad . \tag{1.60}$$

If this image is formed sufficiently close to the focal plane, i.e., for $R_{\mathrm{sl}} \gg R_{\mathrm{li}}$, its size has to be taken into account in deriving the final beam diameter near the focal plane. In this case, the final FWHM beam diameter D_{total} is approximately

$$D_{\mathrm{total}} = \sqrt{\left[\frac{R_{\mathrm{li}}}{R_{\mathrm{sl}}} D_{\mathrm{source}}\right]^2 + \left[\frac{2f}{ak} v_{0.5}\right]^2} \quad . \tag{1.61}$$

Chapter 2

Experimental Configuration

In this chapter, the experimental station is explained, starting with the beamline, then describing the various setups employed, as well as sample holding devices and detectors.

2.1 Beamline 2-ID-B

The measurements described in this thesis have been performed at the undulator beamline 2-ID-B of the SRI-CAT at the Advanced Photon Source [APS]. Figure 2.1 shows a schematic of the beamline. First, a flat mirror suppresses higher-energy x-rays and filters out most of the unused power in the undulator beam to reduce the heat load on the other optical components. A cylindrical mirror then focuses the source vertically onto the location of the exit slit of the monochromator, yielding an approximately 50-μm-sized focal spot in the vertical plane. The third mirror (spherical) focuses the source in the horizontal direction onto the entrance slit of the spherical grating monochromator (SGM). The grating in the SGM focuses the image of the entrance slit onto the exit slit of the SGM. Thus the exit slit acts as a virtual source in the horizontal plane, coincident with the virtual source in the vertical plane provided by the cylindrically focusing mirror. The horizontal beam size is determined by the size of the monochromator exit slit. The experimental setup is located 8 m downstream of the exit slit of the monochromator. Up to this point, the beamline is windowless. A 700×700 μm^2-sized free-standing silicon nitride film of 200 nm thickness, supported on a 5×5 mm^2-sized silicon wafer of 250 μm thickness [FaST], separates the high vacuum in the beamline from ambient pressure. This exit window allows for $\geq 85\%$ transmission for x-ray energies between 1 keV and 4 keV. The experiment was set up in air downstream of this exit window, facilitating modifications and adjustments during the measurement.

The transverse coherence length at the exit window can be calculated according to Eq. (1.3). For an energy of 1820 eV with an effective horizontal source extension of 50 μm determined by

(a)

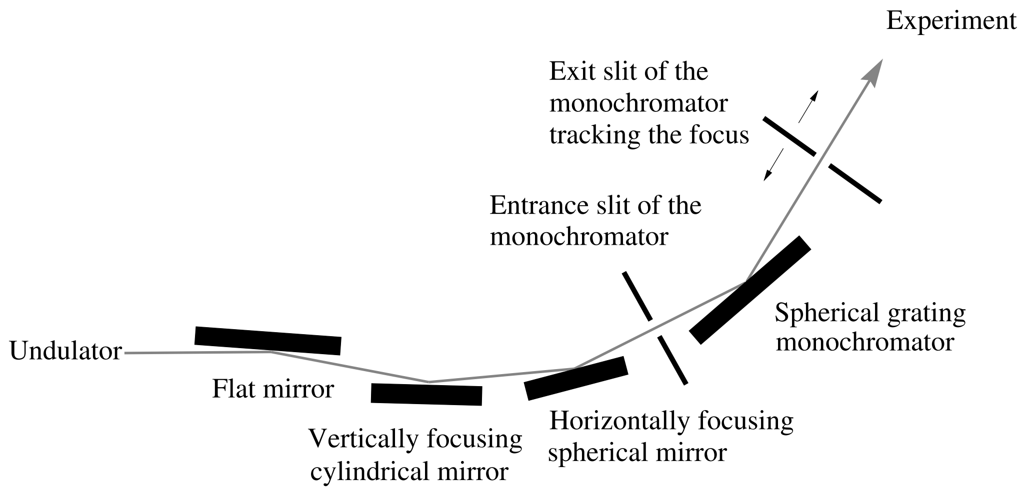

(b)

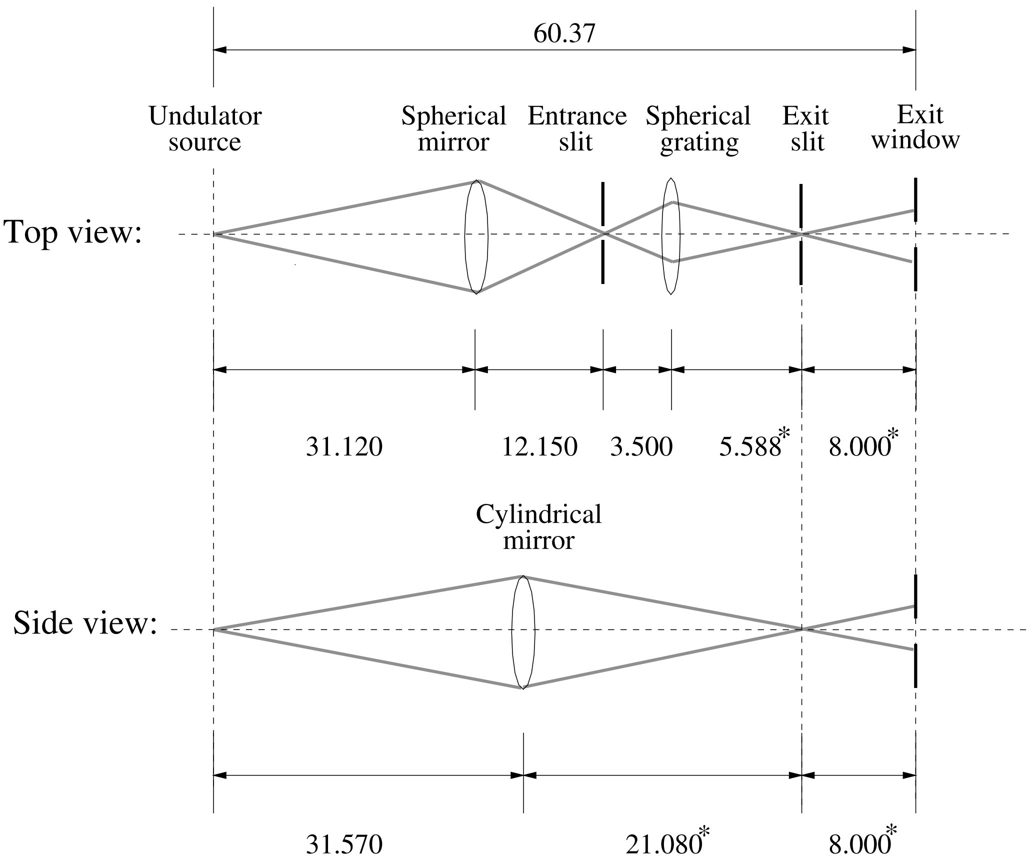

Figure 2.1: *Layout of the beamline: (a) overview, (b) focusing scheme (horizontal above, vertical below). Distances given are in meters for an energy of* 1820 *eV. The asterisked distances change with the selected energy.*

the monochromator exit slit* at 8 m distance from the exit window, Eq. (1.3) yields a transverse coherence length of 65.7 μm, in horizontal as well as vertical direction. Work by Paterson *et al.* [PAM$^+$01] suggests that this assumption for the position and horizontal size of the virtual source is consistent with the measured coherence of the 2-ID-B undulator beam at the experiment for settings of the exit slit smaller than ~ 210 μm. At larger exit slit settings, the degree of coherence in horizontal direction at the experiment is consistent with the coherence as calculated from an incoherent source located at the position of the undulator and demagnified by the beamline optics. This seems to be the minimum degree of spatial coherence present at this beamline. It is determined by the dimensions of the beamline as given in Fig. 2.1. The flux at this beamline is approximately 2×10^7 photons/s within the area of a 5-μm-diameter pinhole, or 5×10^9 photon/s in the first-order focus of a 77-μm-diameter zone plate with 20% efficiency. Both numbers are given for an exit slit size of 50 μm. More detailed information on the beamline and its performance is available in [MKF$^+$96, MFFM97, MFR$^+$98].

2.2 Experimental Setups

For the experiments described in Chapters 3 through 5, two different setups were employed: the widely used pinhole setup, where a pinhole selected a partially coherent pencil-like beam for the experiment (Fig. 2.2 (a)), and a zone plate setup, where a Fresnel zone plate focused the coherent beam onto a submicrometer-sized focal spot (Fig. 2.2 (b)).

High-quality 5- and 10-μm-diameter pinholes made of platinum-iridium (95:5 in vol-%) by Ted Pella, Inc. [TP] were used in the pinhole setup. They had a thickness of 2 μm around the opening. Thus, around the opening, more than 99.2% of the incident x-ray intensity was blocked up to an energy of 4 keV.

The zone plate used had a diameter of 77 μm and a nominal outermost zone width of $\delta_{\mathrm{oz}} = 100$ nm. It focused down to a near-diffraction-limited spot size of approximately 140 nm in diameter with a focal length of 11.3 mm at 1820 eV. A 20-μm-diameter pinhole† used as an order-sorting aperture (OSA) downstream of the zone plate selected the first-order focus by suppressing most of the other diffraction orders of the zone plate. The measured overall efficiency of the zone plate was 20%.

In both setups, the sample was placed into the beam in a transmission geometry (Fig. 2.2) similar to that used in small-angle x-ray scattering (SAXS) experiments. The sample holder (see following section) was mounted on a three-axis translational stage on top of a Huber two-circle

*The effective source extension in the vertical direction is 50 μm, not affected by the size of the monochromator exit slit.

†Again made of platinum-iridium (95:5 in vol-%) with a thickness of 2 μm around the opening, by Ted Pella, Inc. [TP].

(a)

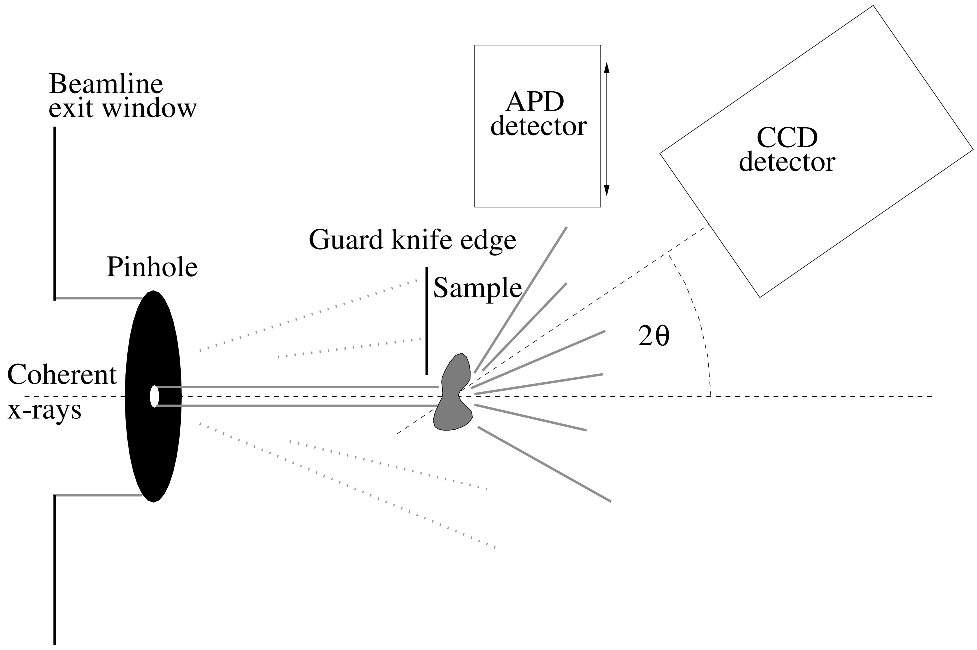

(b)

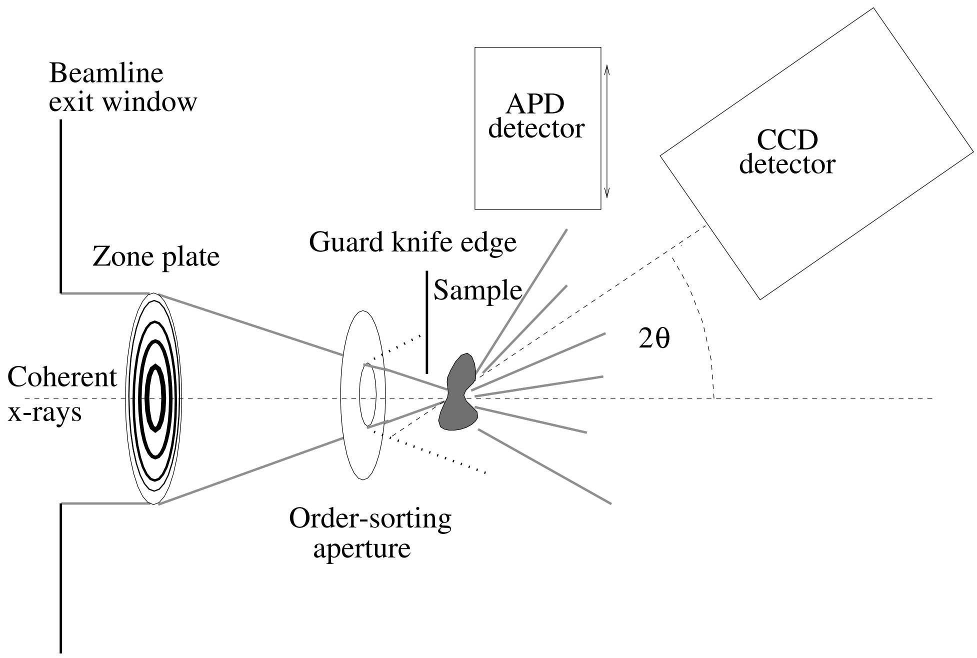

Figure 2.2: *Experimental setups: (a) pinhole setup and (b) zone plate setup.*

goniometer [Hub]. The three-axis stage provided alignment capabilities with respect to the center of rotation and the beam height. For horizontal alignment with respect to the beam, the position of the two-circle goniometer was adjusted by sliding it on a custom-made stainless steel track.

A guard knife edge, consisting of a piece of freeze-clipped single-crystal germanium directly upstream of the sample, blocked parasitic scattering from upstream components. For alignment purposes and to allow for transmission measurements, an avalanche photodiode (APD) could be inserted directly behind the sample. A charge-coupled-device (CCD) area detector was situated further downstream on the 2θ-arm of the two-circle goniometer to measure the scattered intensities at an arbitrary scattering angle 2θ.

2.3 Sample Holder

The sample holder was designed to allow temperature control, as well as a liquid-tight sample environment. Figure 2.3 shows the schematic of this sample holder, which is made of copper to ensure good heat transfer. A copper pipe leading through the body of the holder could be connected to a recirculating chiller to provide temperature control. This basic sample holder body supported various kinds of sample cells as described below. To minimize water condensation when cooling and to minimize absorption by air when using lower-energy x-rays, a cap (see Fig. 2.3, dashed lines) was designed to fit on top of the sample cell. Helium could be blown into this cap through a channel in the body of the sample holder. Beam holes in the cap allowed the

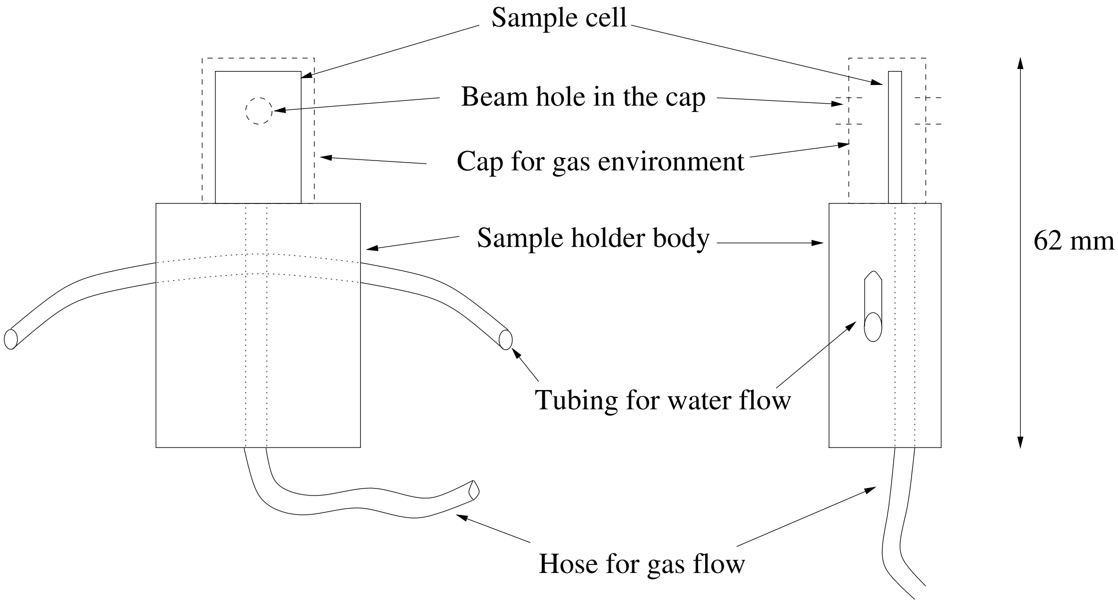

Figure 2.3: *Sample holder. The cap for providing a stable He environment is drawn as dashed lines.*

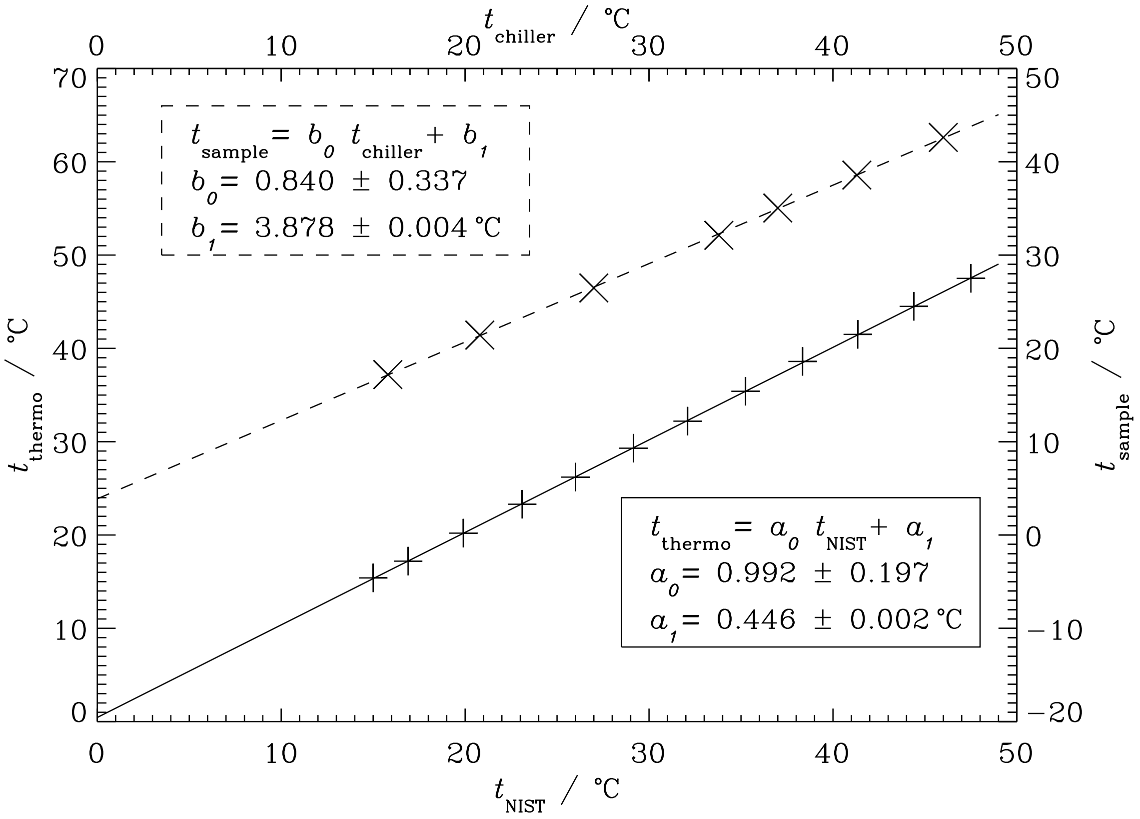

Figure 2.4: *Temperature calibration. The solid line shows a linear regression curve for the relation between data points measured with a thermocouple* t_{thermo} *and data points obtained with a thermometer traceable to NIST standard* t_{NIST} *. The dashed line shows the regression for the relationship between temperature points measured at the sample* t_{sample} *and the chiller set-temperatures* t_{chiller} *. The values given in the boxes are the results of the linear regressions.*

gas to flow out again. Thus, the total air path for the x-rays upstream of the sample could be reduced to $\lesssim 0.5$ mm in the experiments.

The recirculating chiller used in the experiments with temperature control allowed for temperatures between -30 °C and $+150$ °C with a specified accuracy of ± 0.1 °C. Figure 2.4 shows the calibration curves. In order to calibrate the temperature maintained at the sample position for a given temperature setting of the chiller, a type K thermocouple (nickel chromium / nickel aluminum) was calibrated against a thermometer traceable to the standard of the National Institute of Standards and Technology [NIST], using a water bath. This calibration is shown by $(+)$ in Fig. 2.4. The thermocouple was then attached to the sample cell at the position of the sample using thermally conducting grease and used to measure the temperature for various chiller temperature settings. The $(\times)$ symbols in Fig. 2.4 show the results of this measurement. A linear regression of these data points yielded a temperature offset of ~ 3.9 °C and a slope between the chiller set-temperature and the actual temperature at the sample of ~ 0.8 . Including the stan-

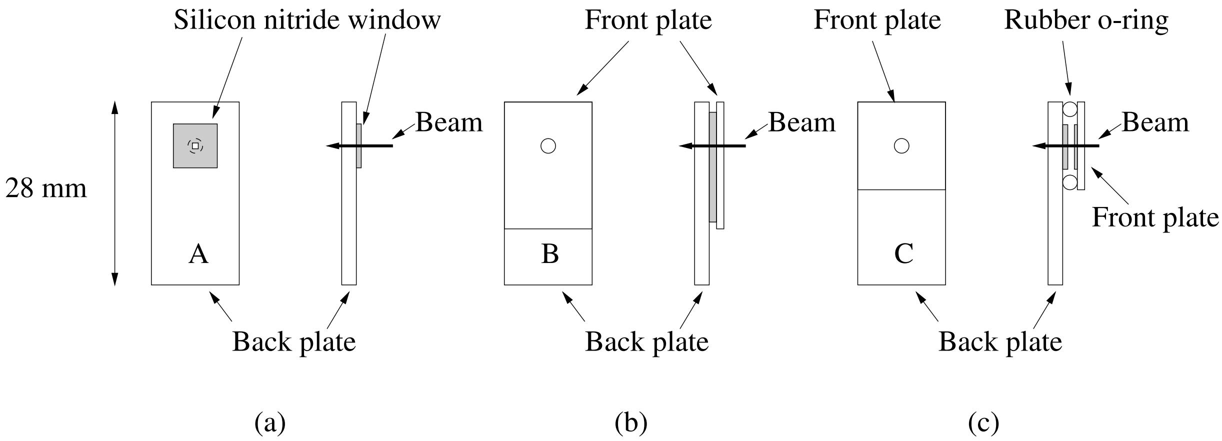

Figure 2.5: *The three different kinds of sample cells used: (a) a plain, flat sample support, sample cell type A, (b) a thin photoresist spacer wet/dry cell, sample cell type B, and (c) a rubber o-ring wet/dry cell, sample cell type C.*

dard deviations of the linear regression values, the temperature at the sample was known with an accuracy of better than 0.4 °C. The observed temperature stability was ± 0.1 °C.

The different kinds of sample cells used are illustrated in Fig. 2.5. Sample cell type A was mostly used for static or solid samples. Types B and C were used for liquid samples.

Sample cell type A was a simple support, used for samples such as powders. A silicon nitride window [FaST] was glued onto a copper plate, $10 \times 28 \times 2$ mm^3, sized to fit into the body of the sample holder. The sample material was held on the silicon nitride window by adhesive forces. The silicon nitride window consisted of a 200-nm-thick free-standing silicon nitride membrane of 700×700 μm^2 in size on a 5×5 mm^2 square silicon wafer of 160 μm thickness.

Sample cells type B and C were designed for samples that needed to be kept either dry or wet, or liquid samples. Type B consisted of a copper back plate, $10 \times 28 \times 2$ mm^3, again sized to fit into the sample holder, and a thin copper front plate. Both plates had specially designed silicon nitride windows attached to them, in between which the sample material was confined. The silicon nitride windows used for this type of cell were elongated versions with 5×15 mm^2 frame size. The window attached to the front plate carried a rim made from photoresist of typically 20 or 50 μm thickness. This rim acted as a spacer and seal at the same time. Thus, the sample material in this cell had a defined thickness and was sealed from influences of the atmosphere. The two sample cell plates were held together by screws.

Sample cell type C provided more space for the sample and its immediate surrounding. The copper back plate, $13 \times 28 \times 2$ mm^3, again fitted into the sample holder body. It had a groove to hold a standard rubber o-ring. The front plate, consisting of 1-mm-thick copper in order to be stable enough to press the o-ring against the backplate, was thinned to ~ 200 μm from the inside within the inner region of this o-ring to reduce the distance between the sample and the exit window of the beamline. Silicon nitride windows as used in sample cell type A were glued to both plates to seal this cell. The sample material was spread onto the window attached to the front plate and was held by adhesive forces. Between the silicon nitride windows of the cell, the o-ring defined roughly a distance of 1 mm. As samples had to be prepared much thinner than that (typically on the order of a few tens of micrometers), thickness control had to be done during the application of the sample material. The size of this cell allowed for additional material inside the cell to maintain a defined environment around the sample material, e.g., a water droplet to provide a quasi-fixed degree of humidity. Again, the two sample cell plates were held together by screws.

2.4 Detectors

Two different detectors were used for the experiments: a charge-coupled-device detector and an avalanche photodiode, the former being an area detector with high sensitivity for low count rates, the latter being a point-type detector with high dynamic range and fast counting capabilities.

Charge-coupled-device (CCD) The Princeton Instruments' [PI] 1024×1024 pixel CCD chip of 25×25 μm^2 size was directly backside-illuminated, i.e., no visible-light optics were involved; the x-ray photons interacted directly with the CCD chip. It was operated at approximately -120 °C (using liquid nitrogen for cooling), so that the dark count rate was effectively zero.[‡] A long vacuum tube evacuated to a pressure below 6.7 Pa in front of the CCD chip prevented water condensation on the cooled CCD chip and reduced the air path for the x-rays (Fig. 2.6). Thus, the total air path (upstream plus downstream of the sample) could effectively be limited to $\lesssim 1$ mm in the experiments.

The entrance window to this vacuum tube was a 250-nm-thick free-standing silicon nitride film of 700×700 μm^2 on a 5×5 mm^2 square silicon wafer [FaST]. It was coated with ~ 1000 Å of aluminum to block the intensity of visible light to less than 10^{-5} times the incident intensity while still providing high transmission of $\gtrsim 75\%$ for x-rays between 1 keV and 4 keV. The length of the vacuum tube was determined by the geometry of the experiment. In general it was chosen to match the condition for the Fraunhofer regime of detection (Eq. (1.4)). The exact length used in the experiments described in this thesis will be given in the experiment-specific chapters.

The sensitivity of a CCD can be evaluated from a double logarithmic plot of the measured noise versus signal in evenly illuminated areas of the CCD chip [JKE87], as shown in Fig. 2.7. The

[‡]The dark count rate specified by the manufacturer was less than 1 e^-/pixel/hour or less than 0.19 digital units/pixel/hour.

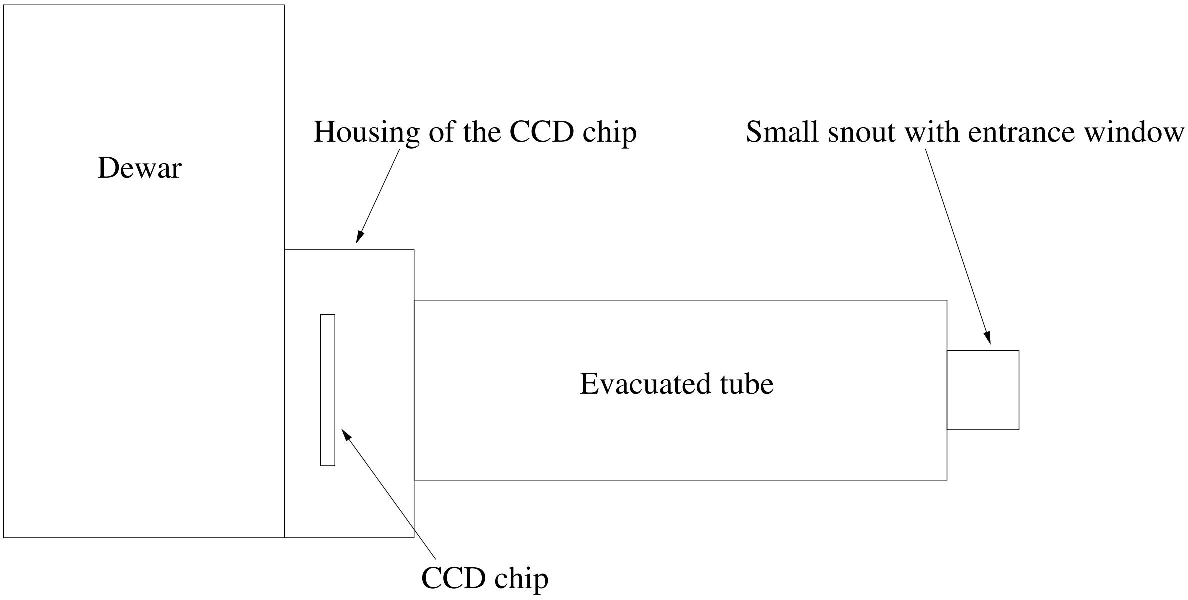

Figure 2.6: *CCD detector.*

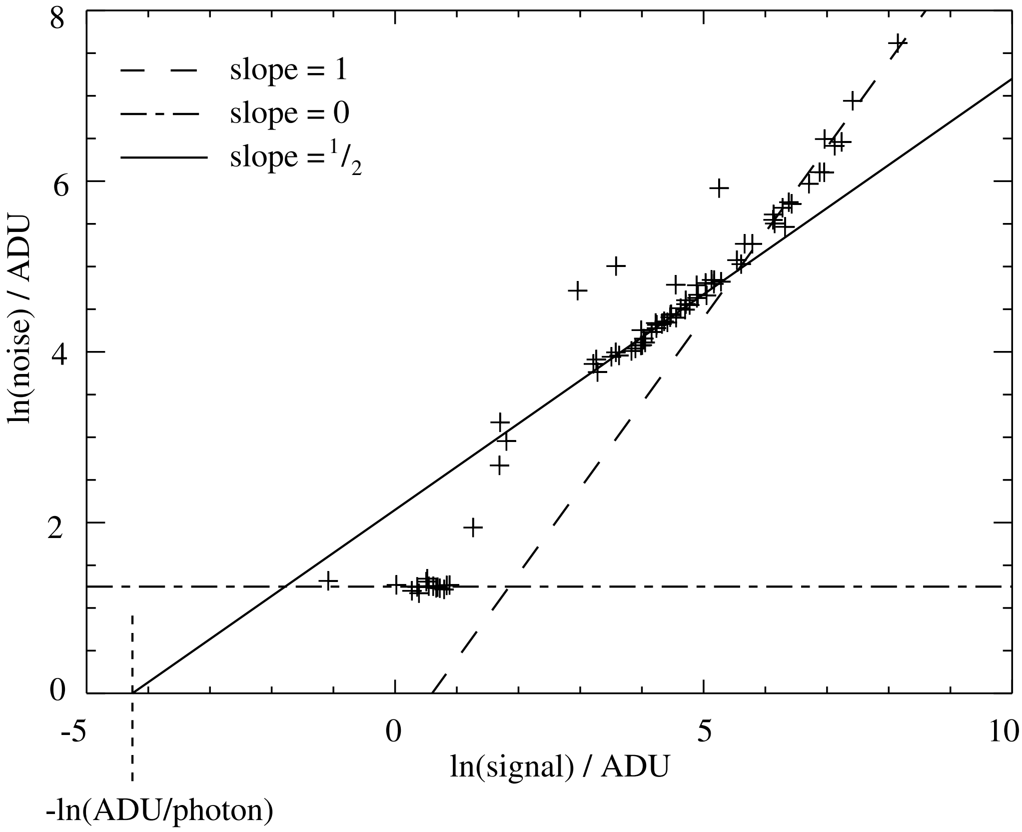

Figure 2.7: *Calibration of the CCD detector.*

CCD used produced 70.63 analog-to-digital units (ADU) per photon at 1750 eV. This number is taken from the intersection of the $\mathrm{slope} = \frac{1}{2}$ part of the plot (solid line) with the abscissa; this intersection falls onto $-\ln(\mathrm{ADU/photon})$.

The $\mathrm{slope} = 0$ part of the plot (dashed-dotted line) describes the root-mean-square CCD read noise, here 3.5 ADU. Compared to the number of ADU/photon, this read noise contribution introduces a small statistical error to the readout. For single photon detection, the error is less than 5% of the produced ADU. For the maximum detectable signal level of ~ 930 photons per pixel, the error is much less than 0.01%.

In addition to the read noise, there is a constant DC-offset arising from, e.g., the analog-to-digital converter or the readout preamplifier of the CCD. This offset is equivalent to $\gtrsim 70$ ADU and depends on the temperature of the CCD chip. The value of 70 ADU is achieved for a chip temperature of approximately -120 °C. The read noise contribution of 3.5 ADU is also small compared to this offset (only $\lesssim 5\%$). Thus, the readout without illumination is dominated by the constant DC-offset.

Towards higher signal levels, the noise-to-signal relation in Fig. 2.7 follows a $\mathrm{slope} = 1$ line (dashed line), which indicates that the CCD was not illuminated evenly at these levels (i.e., not following Poisson statistics), or the pixel response was not exactly uniform.

In order to protect the CCD from saturation, an in-vacuum beam stop was designed to be inserted at ~ 2 mm distance from the CCD chip using a vacuum feed-through. This beam stop consisted of a stick of 700-μm-thick stainless steel, thinned to about 300 μm thickness on approximately 3 mm length at the tip of the stick. This design serves as a beam stop of variable size that can be inserted from one side of the CCD chip until it just blocks the direct beam, which would otherwise damage the CCD.

Avalanche Photodiode (APD) The 5×5 mm^2 square APD made by EG&G [EGG] was covered by a 1×1 mm^2 sized 120-nm-thick free-standing silicon nitride membrane on a 12×12 mm^2 square silicon wafer [FaST]. This silicon nitride membrane, too, was coated with ~ 1000 Å aluminum, thus allowing for $\gtrsim 80\%$ x-ray transmission between 1 keV and 4 keV, while suppressing the intensity of visible light to less than 10^{-5} times the incident intensity. The APD was set up directly behind the sample next to the beam so that it could easily be moved into the beam for alignment purposes and close-up transmission measurements.

Chapter 3

Comparison of Pinhole and Zone Plate Setups

Pinhole setups as described in Chapter 2.2 are routinely used for x-ray speckle experiments. They are simple to align and provide a well-known intensity profile. The focusing zone plate setup is more complicated and not in wide use in this context. Zone plates can provide extremely high spatial resolution by focusing x-rays down to the submicrometer range, yielding a high flux density. However, as their diameter is larger than that of the pinholes usually used in a pinhole setup, they collect photons over a larger area and thus have higher spatial coherence requirements for the incident beam. In addition, for good focusing, a monochromaticity $k/\Delta k$ on the order of the number of zones of the zone plate is required [Mic86]. This requirement may be more stringent than that for good speckle contrast in the pinhole setup. In this chapter, the results of an experimental comparison between the pinhole and the zone plate setup (see Chapter 2.2, Fig. 2.2) are presented.

3.1 The Sample

A dried dispersion of latex (polystyrene) spheres was used as sample material in this experiment. It was made from a water dispersion of highly monodisperse latex spheres with 266 nm diameter [Duke]. The dispersion was provided by the IMM-CAT at the Advanced Photon Source. It had a volume fraction density of 8%. The sample was prepared by spreading the liquid dispersion over a sample cell type A (see Chapter 2.3) and letting it dry in air. Thus, an approximately 60-μm-thick random distribution of spheres within the beam was achieved.

3.2 Measurement Technique

A 5-μm-diameter pinhole was used for the pinhole setup. The zone plate was already described in Chapter 2.2. For both setups, the CCD camera detector was located 517 mm downstream of the sample in on-axis position. The scattering angle 2θ in this experiment was $\lesssim 20$ mrad. With this, the stringent criterion of quasi-monochromaticity (Chapter 1.2) is not satisfied, since the maximum optical path length difference exceeds the longitudinal coherence length $\lambda^2/\Delta\lambda$ by a factor of up to 1.4. Work by Tsui and Mochrie [TM98], however, showed that reasonable speckle contrast can be achieved with path length differences of at least up to 2.5 times the longitudinal coherence length.

Figure 3.1 shows speckle patterns recorded with the two setups with the CCD camera and the dried polystyrene latex sphere sample. All images were taken at a photon energy of 1820 eV. Besides the random arrangement of the spheres leading to speckles, the high degree of monodispersity led to a ring-like small-angle scattering structure in reciprocal space resulting from the sphere-form-factor of the spheres. This structure was easily recognizable in the pinhole case. The speckles were much smaller than the radial width of the rings. Their size was determined by the size of the pinhole used (Eq. (1.15)). In the pattern recorded with the zone plate setup, the sample was close to (but not at) the focal plane of the zone plate. Therefore, the beam on the sample was ~ 240 nm in FWHM diameter. This produced much larger speckles, approximately $^1\!/_6$ of the linear dimensions visible in Fig. 3.1. The ring pattern originating from the latex spheres could no longer be detected.

Speckle images to measure the speckle size and speckle contrast were recorded with the two setups. In the zone plate setup, the distance between the focal plane of the zone plate and the sample was varied in order to change the diameter of the illuminated area on the sample.

3.3 Data Reduction Method

The signal output of CCD area detectors, similar to most detectors, lies on a background level that is independent from the incident radiation and the counting time* but rather is due to DC offsets as they can, e.g., arise from the CCD pixel response, in the readout preamplifier or in the analog-to-digital converter. This background is called dark image $I_\mathrm{d}(\vec{p})$, where $\vec{p}$ indicates the position of a pixel on the area detector. The dark image usually exhibits a signal level that varies with a small standard deviation (read noise) from pixel to pixel and frame to frame on top of the signal due to the DC offsets. In addition to these statistical variations due to the readout process,

*In general, in addition to such a time-independent background level a time-dependent one might be observed. However, as was explained in Chapter 2.4, the detector of interest for this thesis showed an effectively exposure-time independent background level of digital units that is referred to here.

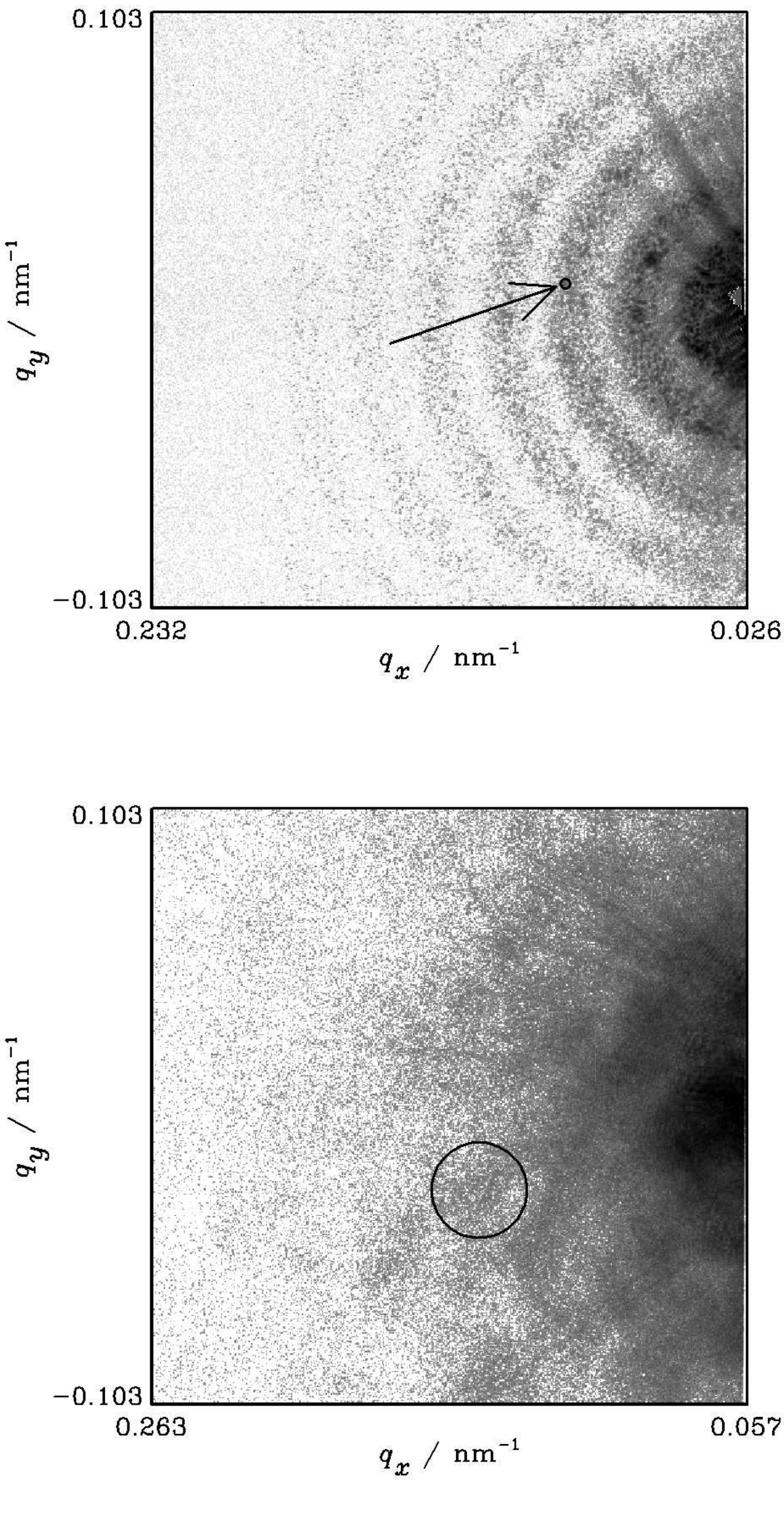

Figure 3.1: *Speckle patterns from polystyrene (latex) spheres recorded with a pinhole (top) and a zone plate (bottom) setup. The circles on the images indicate the approximate speckle size.*

nonrandom variations from pixel to pixel of the detector may occur in a systematic manner, e.g., due to fabrication difficulties or local damage of the CCD chip.

The two-dimensional raw data $I_0(\vec{p})$ in a detection frame had to be preprocessed in order to correct for this variable background. To get an estimate for a master dark image $I_{\mathrm{d_m}}(\vec{p})$, a series of dark images was recorded† and averaged on a pixel-by-pixel basis, to reflect nonrandom pixel dependencies of a typical dark image recorded with this particular area detector. This master dark image was then scaled to the background level of the data image using the average readout level in a small area A of the data image where almost no photon signal was detected:

$$I_{\mathrm{d}}(\vec{p}) = I_{\mathrm{d_m}}(\vec{p}) \frac{\left\langle I_0(\vec{p}) \right\rangle_{[\vec{p} \epsilon A]}}{\left\langle I_{\mathrm{d_m}}(\vec{p}) \right\rangle_{[\vec{p} \epsilon A_{\mathrm{det}}]}} \quad , \tag{3.1}$$

where A_{det} is the whole CCD-frame area. This derivation of a dark image corresponding to an image $I_0(\vec{p})$ accounts for drifts in the background level over the course of the measurements, e.g., due to warming of the detector. To correct the data for the background contribution, $I_{\mathrm{d}}(\vec{p})$ was subtracted from the raw data $I_0(\vec{p})$ on a pixel-by-pixel basis. Setting all negative values of this result to zero yielded the preprocessed data $I(\vec{p})$. The error introduced by this treatment is on the order of the read noise, usually far below the number of counts produced by a single detected photon.‡

After this background subtraction, the data were normalized to their q-dependence $S(q)$ and their total intensity I_{tot} to remove dependencies on the radial scattering strength, as well as on fluctuations in the incoming intensity over the time of the experiment. Then, the normalized spatial intensity autocorrelation function (Eq. (1.6)) was calculated within square areas around selected $\vec{q}$-positions with $0.05\ \mathrm{nm}^{-1} \leq |\vec{q}| \leq 0.17\ \mathrm{nm}^{-1}$. These square areas were chosen to have the size of approximately 10 speckles for good statistical averaging. They were placed in rings around the central beam location, overlapping by half of their area in order to provide information with fine step widths in reciprocal space. A two-dimensional Gaussian function was then fit to the normalized autocorrelation function to determine its width and height.

Afterwards, values from different squares belonging to the same $q = |\vec{q}|$ were averaged to yield the speckle contrast and speckle width as a function of q, with variances reflecting their azimuthal variations. For the purpose of comparing overall effects in this chapter, the data were subsequently averaged over all selected q-positions in the pattern. Thus, any q-dependence is included in the errors associated with the q-averaged quantities.

In the scope of this work, this whole data reduction method as described above has been coded in an IDL [IDL] computer program.

†To record a dark image, the CCD is read out without prior exposure to radiation.

‡For numerical values see Chapter 2.4.

3.4 Results and Discussion

3.4.1 Speckle Contrast

The speckle contrast derived from the measurements using the data reduction method described in the previous section is shown in Fig. 3.2. The open symbols are the zone plate data; the closed symbol is the pinhole data point. It is noticeable immediately that the level of speckle contrast in the pinhole case is much higher than that in the zone plate case. This can be explained by the degree of spatial coherence involved in the experiments: in the pinhole case, the exit and entrance slits of the monochromator were set to $\sim 400\ \mu$m in order to maximize the flux on the sample. Therefore, according to Eq. (1.3) and Chapter 2.1, the spatial degree of coherence $|\mu|$ across the $5\ \mu$m pinhole was about 94% in the horizontal direction and about 99.7% in the vertical direction, yielding an average of about 97%. The speckle contrast Γ_{corr} deduced from Eqs. (1.25) and (1.27) for the pinhole case is shown as a dotted line in Fig. 3.2. It agrees well with the measurement within the error bars.

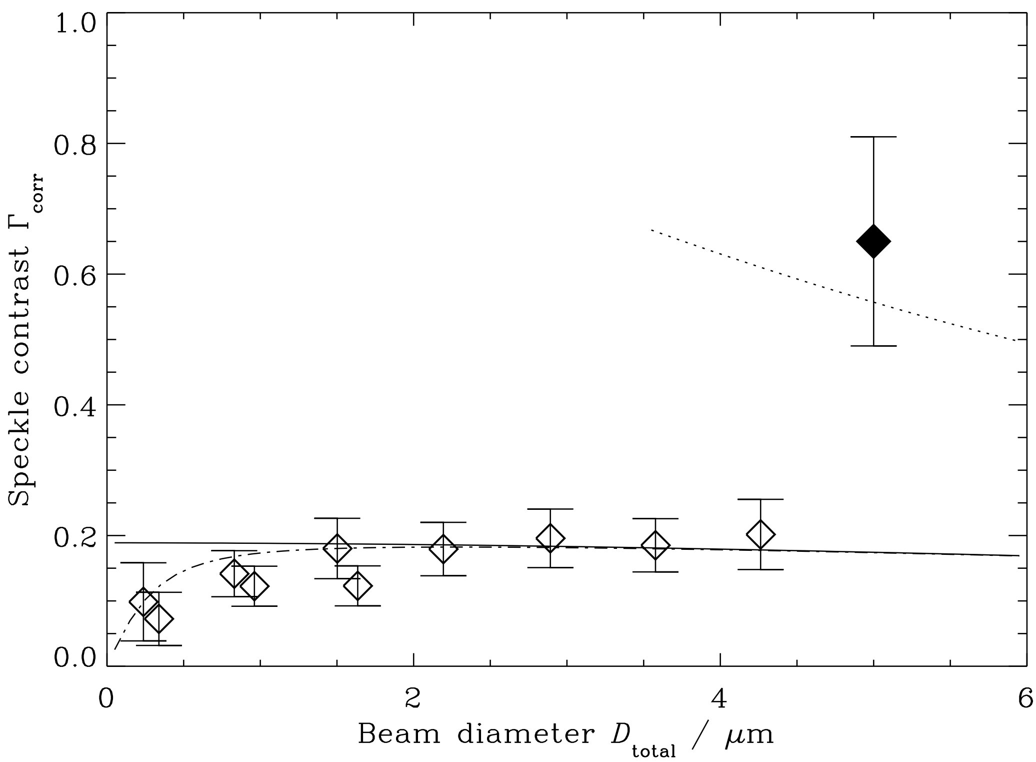

Figure 3.2: *Dependence of speckle contrast on focusing optics. The open symbols represent the data from the zone plate setup, the solid symbol, from the pinhole setup. All data have been averaged over a range of* $0.05\ \text{nm}^{-1} \leq q \leq 0.17\ \text{nm}^{-1}$. *Any dependence on* q *is reflected in the error bars. The lines show calculations of the speckle contrast* Γ_{corr} *as described in the text.*

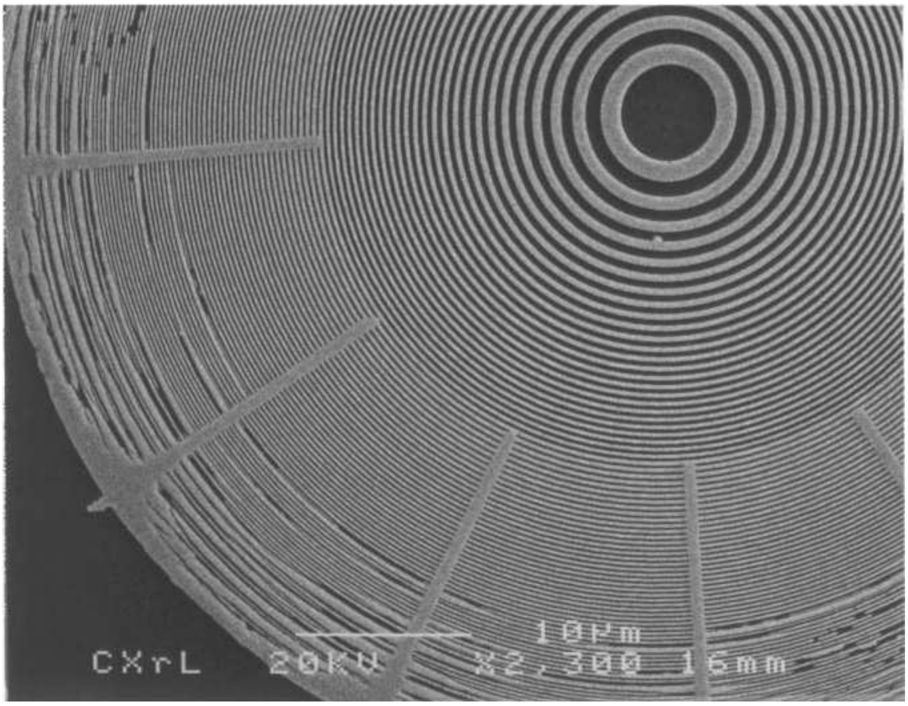

Figure 3.3: *Scanning electron microscope image of the zone plate used in the experiment.*

In the zone plate case, the entrance and exit slits of the monochromator were set to 50 μm to provide a high degree of spatial and temporal coherence across the zone plate. The transverse coherence length was therefore higher ($\sim$ 66 μm) than in the pinhole setup. However, the zone plate, with a diameter of $D_{\mathrm{ZP}} = 77$ μm, was less coherently illuminated ($|\mu| \approx 36\%$) than the 5 μm pinhole. Therefore, the speckle contrast should be lower. According to Eqs. (1.25) and (1.27), a speckle contrast of $\sim$ 12% would be expected. The measurements show a level of speckle contrast of $\sim$ 18%, which could mean that the zone plate was more coherently illuminated than predicted. This can be explained by looking at the quality of the zones near the rim of the zone plate. The outer zones are poorly defined as Figure 3.3 shows. This is due to difficulties in manufacturing extremely fine, high-aspect-ratio zones. These outer zones do not contribute to the focus with the same efficiency as the inner part of the zone plate. This effect has been observed frequently for high-resolution zone plates [SJT97]. Photons diffracted by the outer zones into areas outside of the first-order focus would reduce the overall speckle contrast measured in the two-dimensional image. As described in Chapter 2.2, the OSA blocks most of these photons. Thus for all practical purposes, the zone plate can be assumed to have smaller than nominal radius. Neglecting the contribution of the outer 3 μm of the zone plate radius (i.e., 29 zones or 15% of the area of the zone plate), the remaining part is illuminated more coherently ($|\mu| = 43.4\%$) , and the calculated general speckle contrast level (Eqs. (1.25) and (1.27)), shown as the solid line in Fig. 3.2, then agrees well with the data.

Assuming that the outer zones do not contribute to the focus, the resulting beam diameter on the sample was calculated from the distribution of the delivered energy in the vicinity of the focus of a lens (see Chapter 1.4). The contributing part of the zone plate still consisted of $N = D_{\mathrm{ZP}}/4\delta_{\mathrm{oz}} \approx 164$ zones, where $\delta_{\mathrm{oz}} = 108.4$ nm is now the width of the outermost contributing zone. Thus, N is large enough to justify calculations using the perfect-lens approximation outlined in Chapter 1.4.

According to the thin-lens law

$$\frac{1}{f} = \frac{1}{R_{\mathrm{sl}}} + \frac{1}{R_{\mathrm{li}}} \quad , \tag{3.2}$$

where $R_{\mathrm{sl}} = 8$ m is the distance from the source to the lens (see Chapter 2.1), R_{li} is the distance from the lens to the image of the source, and $f = 11.3$ mm is the first-order focal length; the source image was located $16\ \mu$m away from the focal plane. As the depth of focus of the zone plate, i.e., the axial position at which the intensity drops to 50% of its maximum, was calculated to be $\pm 61.5\ \mu$m [BW97], the source image could thus for all practical purposes be considered to be located directly at the focal plane of the zone plate. The image size D_{image} of the $D_{\mathrm{source}} = 50$-μm-sized virtual source at the exit slit of the monochromator was according to Eq. (1.60)

$$D_{\mathrm{image}} = D_{\mathrm{source}} \frac{R_{\mathrm{li}}}{R_{\mathrm{sl}}} \approx 71 \text{ nm} \quad , \tag{3.3}$$

which is not negligible compared to the FWHM diffraction-limited focal diameter of $D_{\mathrm{diffr}} = 1.03\,\delta_{\mathrm{oz}} \approx 112$ nm (Eq. (1.49)). Thus, the image size had to be considered as well in determining the size of the beam, as outlined in Chapter 1.4.

The two contributions D_{diffr} and D_{image} yield the total FWHM beam diameter D_{total} *exactly at* the focal plane via

$$D_{\mathrm{total}} = \sqrt{D_{\mathrm{image}}^2 + D_{\mathrm{diffr}}^2} \approx 132 \text{ nm}. \tag{3.4}$$

For beam diameters *near* the focal plane, D_{diffr} in Eq. (3.4) has to be substituted by the calculated diameter of the beam at the given distance from the focal plane (see Chapter 1.4). The effect of the size of the source image becomes negligible for distances larger than $\sim 250\ \mu$m away from the focus. Figure 3.4 shows the resulting beam diameter with varying distance from the focal plane of the zone plate. The solid line represents the diameter of the circle centered on the beam axis, containing 50% of the total delivered energy in a plane perpendicular to the beam axis at the given distance from the focal plane. The dashed line shows the boundary of the geometrical cone between the zone plate disk and a point-type focus, over-estimating the FWHM beam diameter in most of the region shown. The beam diameters for which the speckle contrast data are shown in Fig. 3.2 are the values corresponding to the focal distances indicated in Fig. 3.4 by the vertical dotted lines. Because the sample was approximately $60\ \mu$m thick, these beam diameters describe the diameter in the center of the sample, decreasing slightly toward the end of the sample that was closer to the focal plane and increasing toward that further away from the focal plane. The smallest beam diameter probed in this experiment was 237 nm at $\sim$ 60-μm-distance from the focal plane.

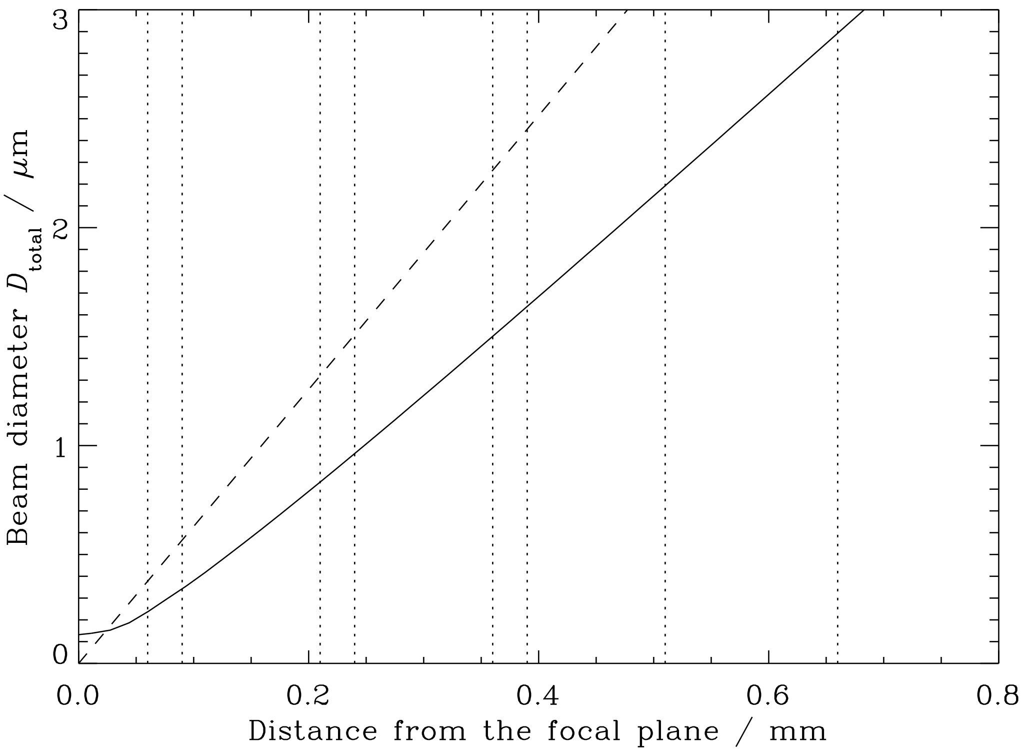

Figure 3.4: *Beam diameter as a function of distance from the focal plane of the zone plate. The solid line was calculated according to Eq. (3.4). The vertical dotted lines indicate the positions of the sample during the speckle measurements. The dashed line shows the boundary of the geometrical cone between the disk of the zone plate and the focal point. For small distances from the focal plane, the deviation from a point-like focus, due to diffraction limitation and the image size of the source, can clearly be seen.*

In microscopy, an oft-quoted number for a zone plate's performance is its Rayleigh-criterion resolution $1.22\,\delta_{\text{oz}}$ [Mic86]. It describes the distance from the center of the beam at the focus to its first intensity minimum. The FWHM focal diameter calculated here in Eq. (3.4) corresponds to a Rayleigh-criterion resolution of ~ 150 nm, where the size of the source image ($D_{\text{image}} = 71$ nm) has been taken into consideration as well. This number agrees with other experiments [MFFM97, SSX$^+$00] that measured the spatial resolution achieved with this zone plate. The Rayleigh criterion will not be used furthermore in this thesis. Instead, quoted sizes will represent FWHM quantities.

The observed decrease in speckle contrast towards very small beam diameters on the sample in Fig. 3.2 cannot be explained by Eqs. (1.25) and (1.27). They, in fact, predict a slight increase in speckle contrast with decreasing beam diameter on the sample, i.e., increasing speckle size (see solid line in Fig. 3.2). The reason for this is that instrumental resolution effects, as, e.g., resulting from limited temporal and spatial coherence, that are shifting part of the intensity from maxima to minima in the speckle pattern remain unchanged. Thus, their relative effect on the speckle

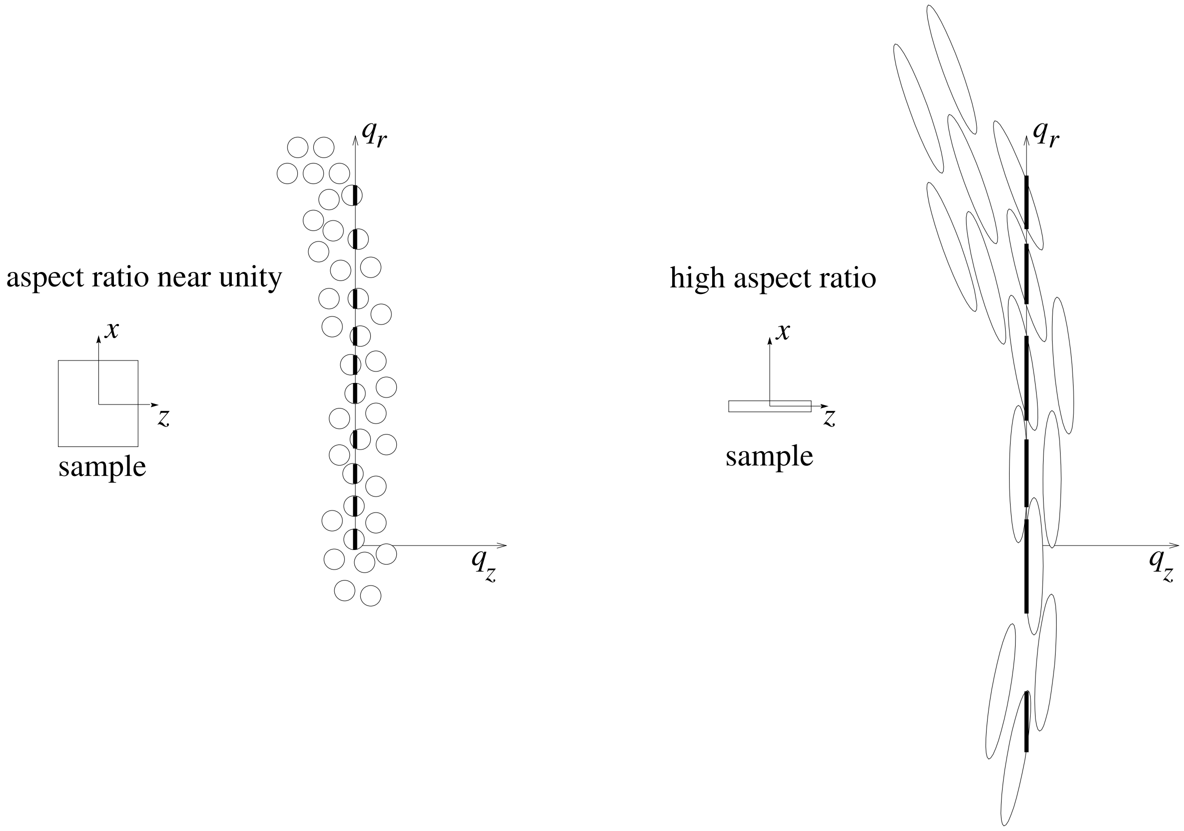

Figure 3.5: *Resolution effect of a sample illumination with an aspect ratio near unity or with high aspect ratio. Circles and ellipses represent speckles in q-space. Their position and orientation follow the curvature of the wave front. The detector plane is parallel to the q_r-axis. Bold lines indicate how the speckles are seen by the detector.*

pattern decreases with increasing speckle size, which relatively improves the speckle contrast.

This behavior, however, is clearly not observed in the data. On the contrary, the measured speckle contrast decreases. This is due to the high aspect ratio of sample thickness to beam diameter, combined with the effect of a planar detector recording a curved wavefront: the sample was $\sim 60\ \mu$m thick; the beam diameters near the focal plane of the zone plate were about a factor of 250 smaller. Figure 3.5 illustrates the case. The detection plane in reciprocal space was located at $q_z = 0$ (on-axis position). The locations of the speckles in q-space fall on the approximately spherical curve of $[q_r, q_z] = k[\sin(2\theta), \cos(2\theta) - 1]$.

For an aspect ratio near unity, the speckles in reciprocal space are approximately symmetric in beam direction q_z and perpendicular to it in direction q_r. As the speckles are approximately circular in this $[q_r, q_z]$-plane, the angle under which the detector plane cuts through a single speckle does not affect the measured intensity distribution to a large extent.

However, if the aspect ratio is very high, the speckles become ellipses, having a much bigger size perpendicular to the beam than parallel, i.e., $|\Delta q_z/\Delta q_r|_{\text{speckle}} \ll 1$. In addition, they are now clearly following the spherical wave front of the beam. If the local slope of this wave front in q-space $|\Delta q_z/\Delta q_r|_{\text{front}} = [1 - \cos(2\theta)]/\sin(2\theta) \approx 2\theta/2$ is comparable to the inverse aspect ratio of a speckle $|\Delta q_z/\Delta q_r|_{\text{speckle}} \approx \sigma_D/\sigma_T$, then the detector plane might cut through the next speckle before the first one is passed, i.e., the detected speckles appear closer to each other and start to overlap, which reduces the speckle contrast. Therefore, the ratio

$$r_{\text{asp}} = \frac{|\Delta q_z/\Delta q_r|_{\text{front}}}{|\Delta q_z/\Delta q_r|_{\text{speckle}}} \approx \frac{2\theta/2}{\sigma_D/\sigma_T} \tag{3.5}$$

washes out the detected speckles in radial direction. In addition to the resolution terms in Eq. (1.27), the speckle contrast now contains a contribution from Eq. (3.5), i.e.,

$$\Gamma_{\text{corr}} = \Gamma \frac{1}{\sqrt{1 + r_{\text{det}}^2 + r_{\text{source}}^2 + r_{\text{asp}}^2}} \ . \tag{3.6}$$

This additional contribution can explain the observed decrease of the speckle contrast function Γ_{corr} for small beam diameters. The dash-dotted line in Fig. 3.2 shows Γ_{corr} for the above-mentioned spatial coherence including the aspect-ratio correction. The data agree very well with this geometrical model.

In this analysis of the speckle contrast, it is important to notice that there is *no direct dependence* on the zone plate divergence of ~ 7 mrad. If this divergence smeared out the speckles (as any incoherent divergence accounted for in r_{source} would), speckles should not be seen anymore, once the sample is out of the focal plane and the intrinsic speckle size according to the beam diameter on the sample is reduced. But, the observed speckle contrast remains high. So, the high divergence introduced by the zone plate focusing does *not* smear out the speckles. The reason for this is the conservation of the information about the phase-space element of the incoming radiation throughout the focusing process.

The azimuthally averaged intensity versus q, i.e., the incoherent scattering from the sample, is plotted in Fig. 3.6. The open symbols again represent the zone plate data, the solid ones, the pinhole data, both being circular averages from the recorded speckle patterns shown in Fig. 3.1. The lines are calculations of the expected patterns originating from the form factor $\mathcal{F}(qR)$ of the spheres in the sample [GF55] convolved with a given resolution σ_{qR}:

$$I(q) = c \cdot \mathcal{F}(qR) \otimes \frac{1}{\sqrt{2\pi\sigma_{qR}^2}} \exp\left(-\frac{[qR]^2}{2\sigma_{qR}^2}\right) \ , \tag{3.7}$$

where

$$\mathcal{F}(qR) = \left[\frac{3\big[\sin(qR) - qR\cos(qR)\big]}{[qR]^3}\right]^2 \ , \tag{3.8}$$

with the radius R of the spherical particles in the sample. c is a proportionality constant. The Gaussian-shaped resolution σ_{qR} is given by the q-resolution σ_q and the monodispersity of the

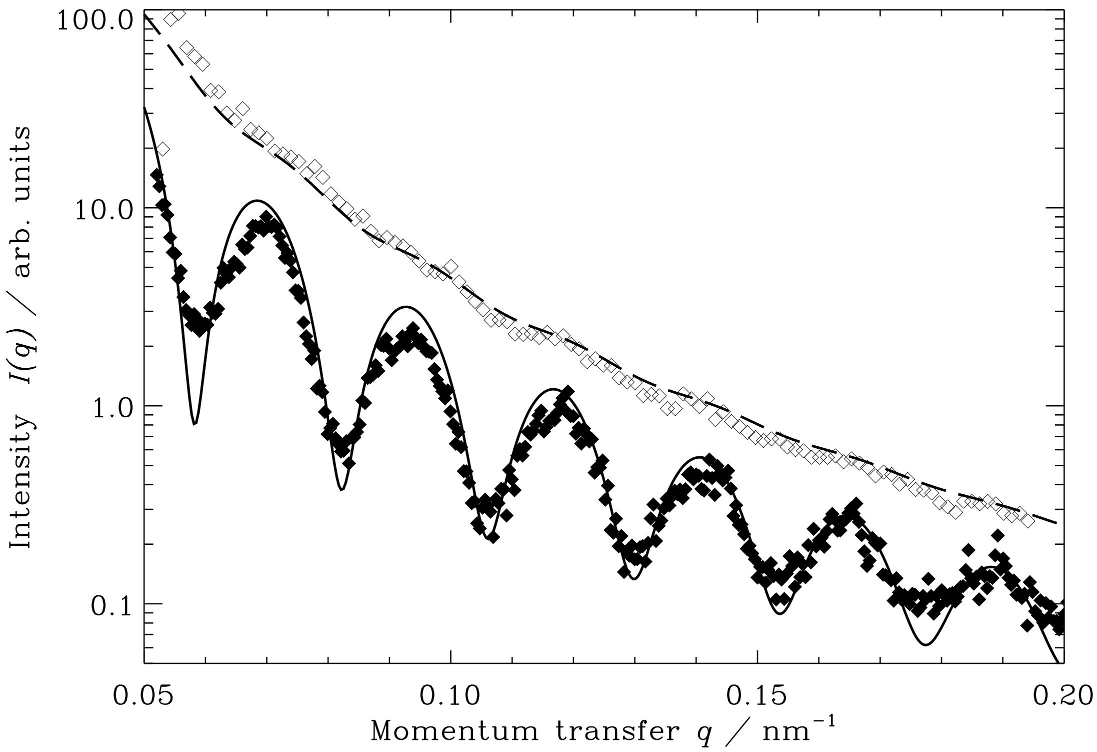

Figure 3.6: *Incoherent small-angle scattering from the sample. This plot shows the azimuthally averaged intensity of the two speckle patterns shown in Fig. 3.1. The open symbols represent zone plate data, the solid, pinhole data. The lines are calculations of the intensity $I(q)$ as described in the text.*

latex spheres, expressed by σ_R :

$$\sigma_{qR} = R\,\sigma_q \, + \, q\,\sigma_R \quad . \tag{3.9}$$

σ_q consisted of three parts: one being related to limited monochromaticity, $\sigma_{q,\mathrm{mono}}$, the second resulting from the limited spatial coherence of the beam, $\sigma_{q,\mathrm{coh}}$ [Goo85], and the third originating from the q-averaging property of the detector, $\sigma_{q,\mathrm{det}}$. These terms were added quadratically:

$$\sigma_q^2 = \sigma_{q,\mathrm{mono}}^2 + \sigma_{q,\mathrm{coh}}^2 + \sigma_{q,\mathrm{det}}^2 \quad . \tag{3.10}$$

$\sigma_{q,\mathrm{mono}}$ was derived according to

$$\sigma_{q,\mathrm{mono}} = \frac{\Delta q}{2\sqrt{2\ln(2)}} \quad , \qquad \frac{\Delta q}{q} = \frac{\Delta k}{k} \quad , \tag{3.11}$$

where Δk and Δq represent the FWHM of the variations in k and q, respectively. To convert the degree of spatial coherence $|\mu|$ as given on page 33 into a wave number spread, the following relations were used:

$$|\mu| = \frac{\sin\nu}{\nu} \quad , \qquad \Delta 2\theta = \frac{\Delta x}{R_{\mathrm{source}}} = \frac{2\nu}{ak} \quad , \tag{3.12}$$

where the notation is the same as in Chapter 1.1, and $\Delta 2\theta$ is the so-called FWHM *coherence angle* of the beam. Here, a refers to the beam diameter on the sample ($5\ \mu$m in the pinhole case and 237 nm in the zone plate case). The degree of coherence $|\mu|$ was determined from the diameter of the beam accepted by the experiment[§] ($5\ \mu$m for the pinhole and $71\ \mu$m for the zone plate). Because of the small angles involved, the following simplification could be made:

$$q \approx k\ 2\theta \quad , \quad \sigma_{q,\mathrm{coh}} \approx -\frac{k\ \Delta 2\theta}{2\sqrt{2\ln(2)}} \quad . \tag{3.13}$$

For the detector contribution, the pixel size D_{det} was related to a resolution in q-space:

$$\sigma_{q,\mathrm{det}} = \frac{k}{2\sqrt{2\ln(2)}} \frac{D_{\mathrm{det}}}{R_{\mathrm{det}}} \quad . \tag{3.14}$$

In order to achieve good agreement with the data, σ_R was assumed to be 2.55 nm, which gives a small FWHM particle size distribution of 4.5% of the radius of the spheres.

Note that the calculations of the curves in Fig. 3.6 according to Eq. (3.7) involved no fitting of the q-resolution. The proportionality factor c used to match the measured intensities with the calculations was the same for the two setups after correcting for the different flux. This means that the overall smaller degree of spatial coherence in the zone plate case can explain the loss in *incoherent* q-resolution, observed in the scattering pattern, as well. The q-resolution in the pinhole case is slightly overestimated by the equations above (as can be seen in Fig. 3.6 from the small deviation of the calculated curve from the measured one at the positions of the scattering minima). This may be due to a combination of camera read noise, and poor statistics at low signal levels.

3.4.2 Speckle Width

Figure 3.7 shows the speckle widths measured with the two setups as a function of the beam diameter on the sample. As before, the open symbols are data from the zone plate; the solid symbols correspond to the pinhole data. The beam diameters are the same as derived above. Diamonds represent the speckle widths in radial direction, circles, in azimuthal direction. The lines show the calculations for the speckle widths Ω_{corr} as described in Chapter 1.2, including the additional correction term r_{asp} for the radial speckle widths introduced by the high aspect ratio of the illuminated volume (compare to Eq. (1.26)):

$$\Omega_{\mathrm{corr,rad}} = \Omega_{\mathrm{rad}} \cdot \sqrt{1 + r_{\mathrm{det}}^2 + r_{\mathrm{source}}^2 + r_{\mathrm{asp}}^2} \quad , \tag{3.15}$$

with r_{asp} given by Eq. (3.5). The solid line shows the calculated azimuthal speckle widths (Eqs. (1.15) and (1.26)), which are independent of monochromaticity and aspect ratio; the

[§] See Eq. (1.3) and Chapter 2.1 for details.

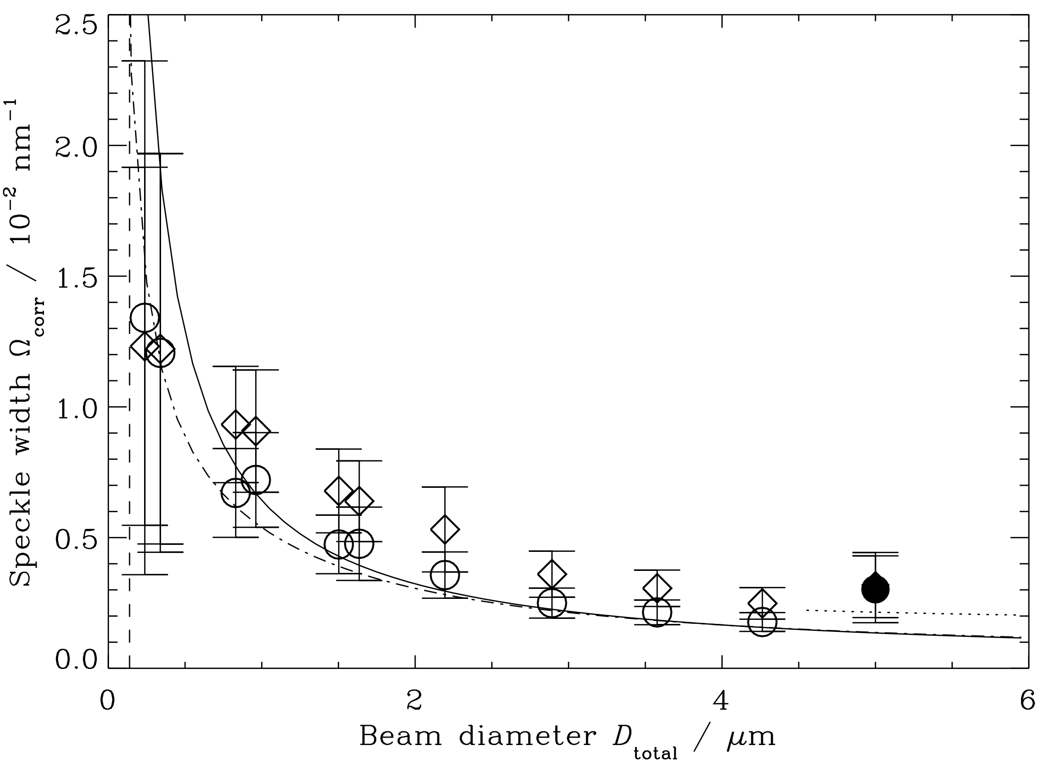

Figure 3.7: *Dependence of speckle widths on the focusing optics. The open symbols show the speckle widths with the zone plate setup; the solid ones show the results from the pinhole setup. Circles are azimuthal widths, diamonds are radial widths. The lines show calculations of* Ω_{corr} *as discussed in the text.*

dashed-dotted line shows the calculated radial widths (Eqs. (1.24) and (3.15)) in the zone plate case; and the dotted line shows the calculated radial widths (Eqs. (1.24)) and (3.15)) in the pinhole case. Both data and calculation have been averaged over q, as previously discussed. The error bars in the plot contain the variance of the data with q. The experimental results agree well with the calculations.

With the exception of the data point at the smallest beam diameter, in the zone plate case the radial widths are systematically larger than the azimuthal widths. This systematic difference may result from the focusing by the zone plate, which is also a radial effect.¶ However, the theory applied does not explain this behavior so far. The reduction of the radial width relative to the azimuthal one for small beam diameters on the sample, predicted by the calculations, was reflected in the data. This can be understood by looking at Fig. 3.5: especially for larger q-values, the speckles are detected under an angle that lets them appear smaller in radial direction, thus reducing the q-averaged speckle width.

¶It can be excluded that this systematic increase of the radial speckle widths is caused by anisotropies in the sample, as they could only affect q_x/q_y but not $q_{\mathrm{rad}}/q_{\mathrm{azim}}$ over the range of interest in reciprocal space.

Again, it can be seen that the speckles were not smeared out by the zone plate divergence. A divergence of 7 mrad would have smeared out the speckles to a size of 9.0×10^{-2} nm^{-1}. This was clearly not the case. The reason is that the zone plate preserves the phase-space volume of the incoming beam. The degree of coherence is not lost due to the focusing. Therefore, the various illumination diameters on the sample in the zone plate setup (controlled by moving the sample to different off-focus positions) behave in the same way as those produced by pinholes, provided the degree of coherence of the radiation used for the measurements is the same in the two cases. If the degree of coherence varies between the two setups, as was the case during this experiment, the information about the coherence in the experiment can be employed to explain the observed speckle widths and speckle contrast.

3.5 Summary

The performances of a pinhole setup and a focusing Fresnel zone plate setup have been compared with respect to speckle contrast, speckle size, and q-resolution. It was found that the pinhole setup is advantageous when high resolution in reciprocal space is needed and sufficient coherent flux is available. On the other hand, a zone plate setup can yield excellent results in experiments aiming for high real-space resolution or suffering from low count rates. As the speckle size is inversely proportional to the beam diameter on the sample, the speckle size can easily be controlled in the zone plate setup by varying the distance between the sample and the zone plate focus. As a consequence of the small beam diameters achievable with focusing by state-of-the-art zone plates, the experimental sample-to-detector distance can be reduced for the same detection-area-per-speckle resolution. Speckle contrast, width and distribution in reciprocal space are not affected by the focusing by the zone plate but rather behave like in a pinhole setup of comparable pinhole size. As the speckle contrast is proportional to the square of the spatial degree of coherence of the radiation used in the experiment, the speckle contrast achieved with the zone plate setup may be lower than that with the pinhole setup if the zone plate is larger and therefore less coherently illuminated than the pinhole. A decrease in speckle contrast for small beam diameters on the sample was observed and could be attributed to the high aspect ratio of the illuminated volume in the sample. This decrease in speckle contrast presents a fundamental limit for highly localized sample studies using speckle experiments.

Chapter 4

Speckle Contrast Variation at Absorption Edges

The energy region of interest, 1 keV to 4 keV, contains many absorption edges of common materials (see Fig. 2). These edges will have influence on the scattering process and thus may also have influence on the contrast in speckle experiments. Speckle contrast variations at sample-specific absorption edges may be of interest, e.g., when samples composed of two or more elements are investigated. With a variation in speckle contrast at a sample-specific absorption edge, it is possible to enhance or suppress speckles originating from one or more of the constituent elements. Recently, absorption edges were used in resonant magnetic speckle experiments, [YLL$^+$99, PVM$^+$00] in order to enhance the magnetic scattering cross section. Still, standard speckle contrast theory as presented in Chapter 1.2 does not account for any speckle contrast effect at absorption edges since it neglects anomalous scattering. In this chapter, edge-dependent x-ray speckle contrast measurements and a theoretical description of the observations are presented.

4.1 The Sample

A zinc powder sample was used for the measurements described in this chapter. This sample material, bought from Aldrich [Ald], consisted of nanometer-sized powder, dissolved in hexanes. The manufacturer characterized it as a metastable, energetically activated powder of ~ 100-nm-diameter grains that may agglomerate to approximately 1 to 2 μm, having a highly defective structure. The samples were prepared by sprinkling the powder on a sample cell type A (see

Chapter 2.3) and shaking off the excess. Thus, a thin, random distribution of powder adhering to the supporting membrane of the holder was achieved.

4.2 Measurement Technique

Speckle contrast was studied across the zinc $2p^{3/2}$ (L_{III}) absorption edge at 1021.8 eV using the metallic zinc powder sample described above. For this experiment, the pinhole setup (see Chapter 2, Fig. 2.2 (a)) with a 10-μm-sized pinhole was used in order to provide high initial speckle contrast. The criterion of quasi-monochromaticity given in Chapter 1.2 was satisfied by not exceeding scattering angles of 5 mrad, which resulted in maximum optical path length differences of less than 0.23 times the longitudinal coherence length $\lambda^2/\Delta\lambda$.

Series of speckle patterns were acquired with the CCD camera detector set up at 973 mm distance from the sample in on-axis position, while the incident photon energy was varied across the absorption edge. The measurements were done at three different energy-resolution settings: 1.8 eV, 3.5 eV, and 6.1 eV. These energy resolutions were produced by different sizes of the monochromator entrance and exit slits. The chosen slit settings were 100 μm, 200 μm, and 400 μm, from which the above energy resolutions were calculated according to diffraction grating theory (see, e.g., [MFFM97, HHH86]). The degree of coherence $|\mu|$ during the experiment was 99.8% in the vertical plane (Eq. (1.3)) for all of the three different energy resolutions, as the vertical source size was not affected by the slit settings. In the horizontal plane, $|\mu|$ was determined by the different source size in the three cases, yielding 98.2%, 92.8%, and 92.1% for the three different energy-resolution settings, respectively (see Eq. (1.3) and Chapter 2.1).

As an example, speckle patterns recorded at 1000 eV and at 1030 eV with an energy resolution of 3.5 eV are shown in Fig. 4.1. The images are plotted on a logarithmic intensity scale with the maximum of the gray scale adjusted to the maximum intensity in the pattern, so that the effect of reduced speckle contrast above the absorption edge is visible and not hidden in the overall decrease in intensity dominating the raw data images.

4.3 Data Reduction Method

The two-dimensional CCD images were analyzed by calculating the normalized spatial intensity autocorrelation functions at various locations in the patterns after normalizing to the q-dependence of the signal $S(q)$ in each pattern. This was done in the way already described in Chapter 3.3. The normalization to the total intensity in each single image of an energy series removed the effect of the decrease in intensity due to attenuation by the sample. Since the speckle

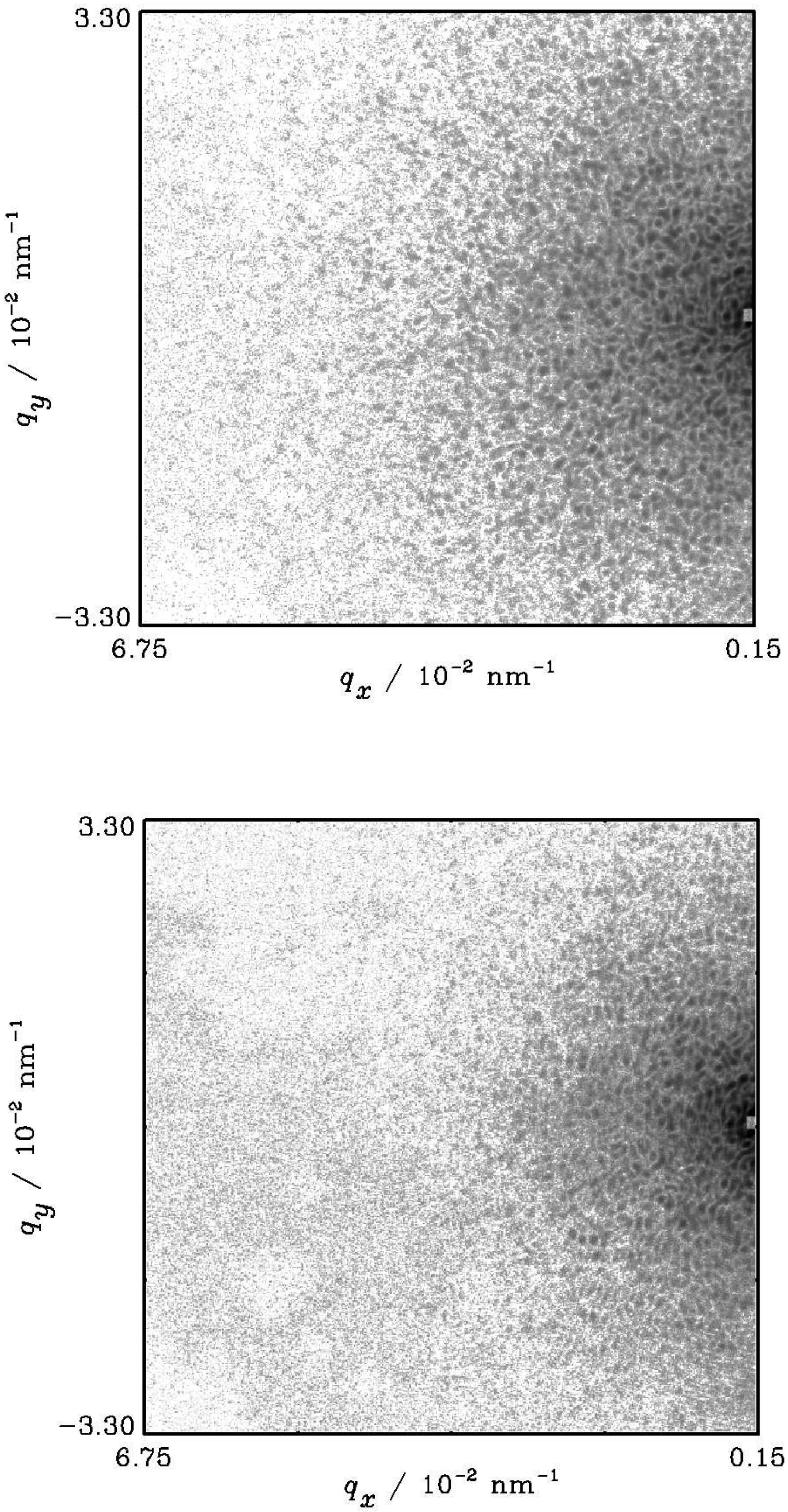

Figure 4.1: *Speckle patterns from a zinc powder sample at an energy resolution of* $3.5\ eV$ *as recorded with a CCD camera: data obtained below the* L_{III} *absorption edge at an energy of* 1000 *eV (top) and above the edge at an energy of* 1030 *eV (bottom). Intensities are plotted on a logarithmic scale adjusted to the maximum intensity in each pattern in order to visualize the effect of reduced speckle contrast otherwise hidden in the overall intensity reduction at the absorption edge.*

contrast as defined in Eqs. (1.6) and (1.7) is *independent* of the total intensity I_{tot} in the patterns, this normalization did not affect the results. The calculation of the autocorrelation function was subsequentially carried out for all images in the energy series. Data and theory functions presented in this chapter were not averaged over q as was done in Chapter 3. Error bars shown indicate azimuthal standard deviations.

4.4 Results and Discussion

Figure 4.2 shows the total transmitted intensity as measured with the APD for the three different energy-resolution settings. The measured speckle contrast in the image series, evaluated as a function of energy at various q-positions in the pattern for the three different energy resolutions is shown in Fig. 4.3 (a) and (b). The speckle contrast decreases at the absorption edge for all q-values probed in this measurement. It shows an energy dependence similar to that of the total transmitted intensity (Fig. 4.2).

The observed variation of the speckle contrast cannot be explained from the spatial autocorrelation function given by Eq. (1.22). The derivation of this equation was based on the assumption that $\langle I(k,r)\rangle_r$ varies slowly with k. Considering this term to be constant over the

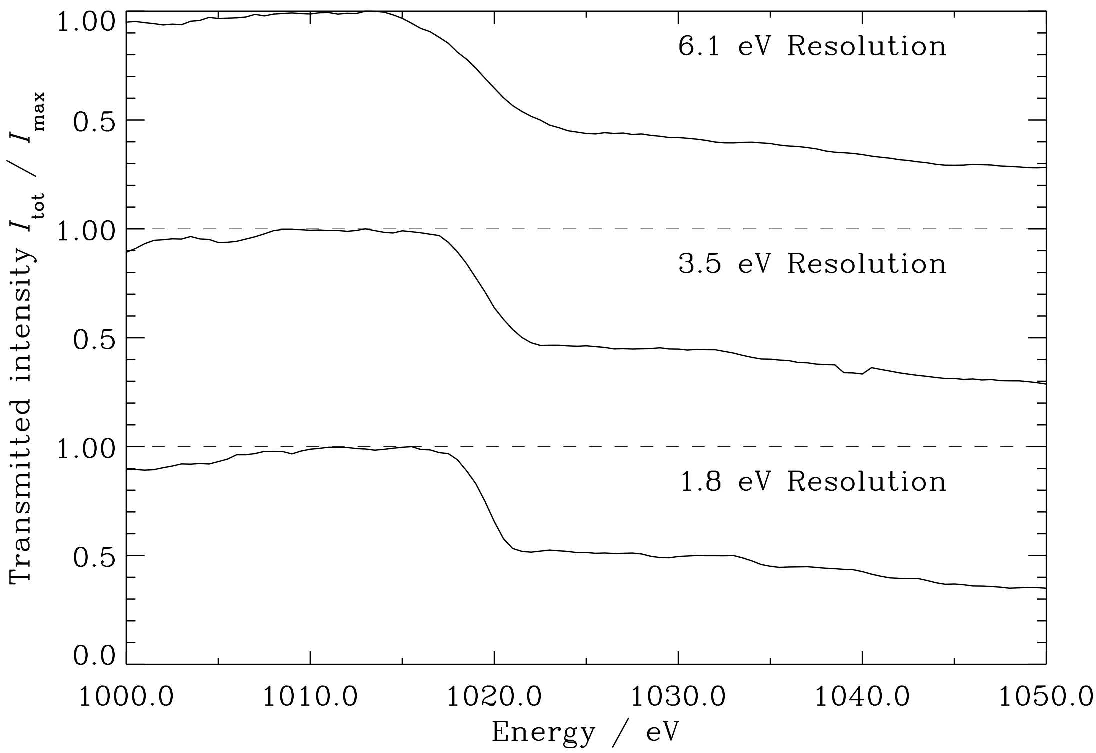

Figure 4.2: *Total transmitted intensity measured with different energy resolutions as a function of the incident energy.*

(a)

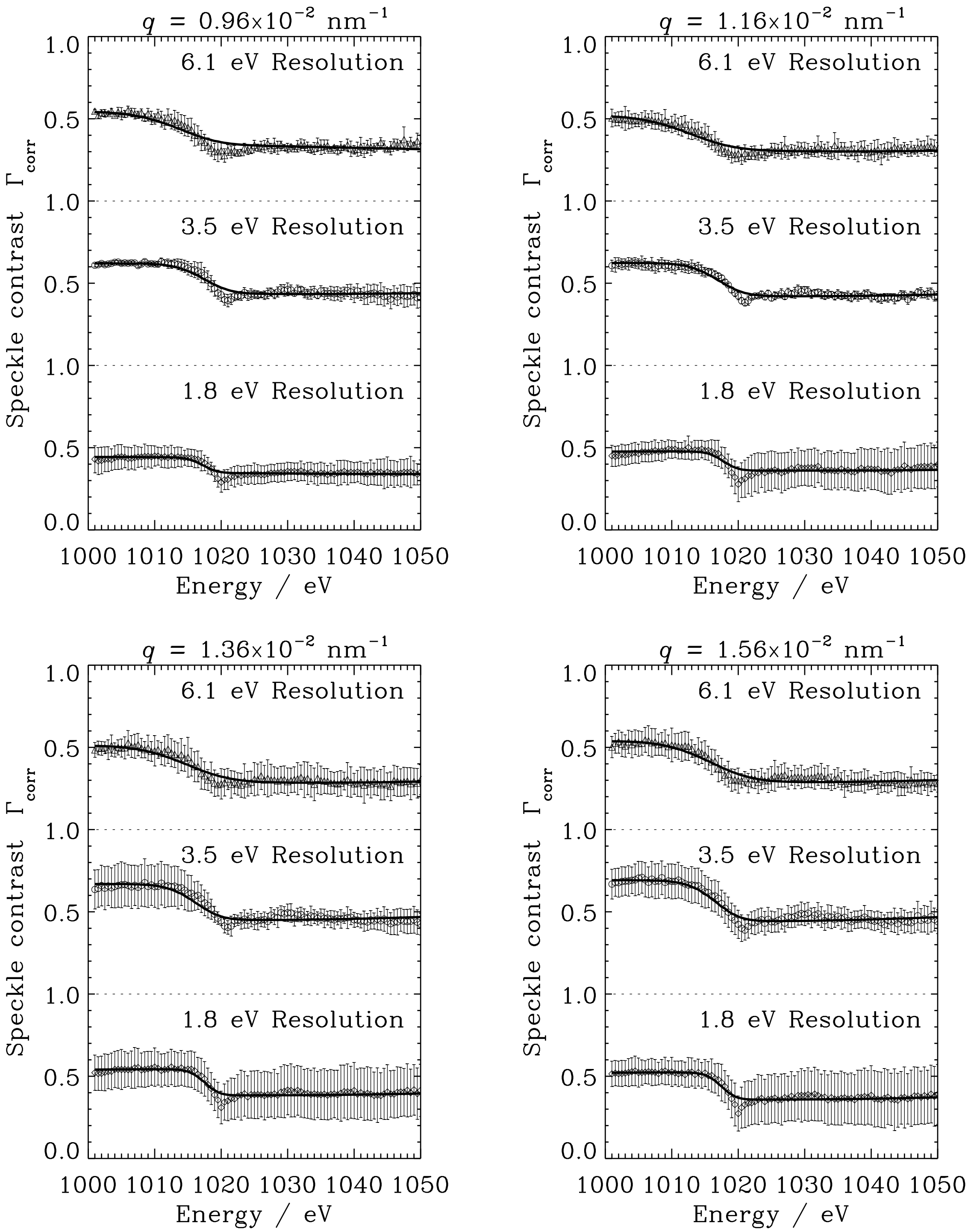

Figure 4.3: *(a) Speckle contrast as a function of energy at different* q*-positions for various energy resolutions. The symbols represent the measured speckle contrast. The solid lines are fits according to Eqs.* (4.1) *and* (3.6)*.*

(b)

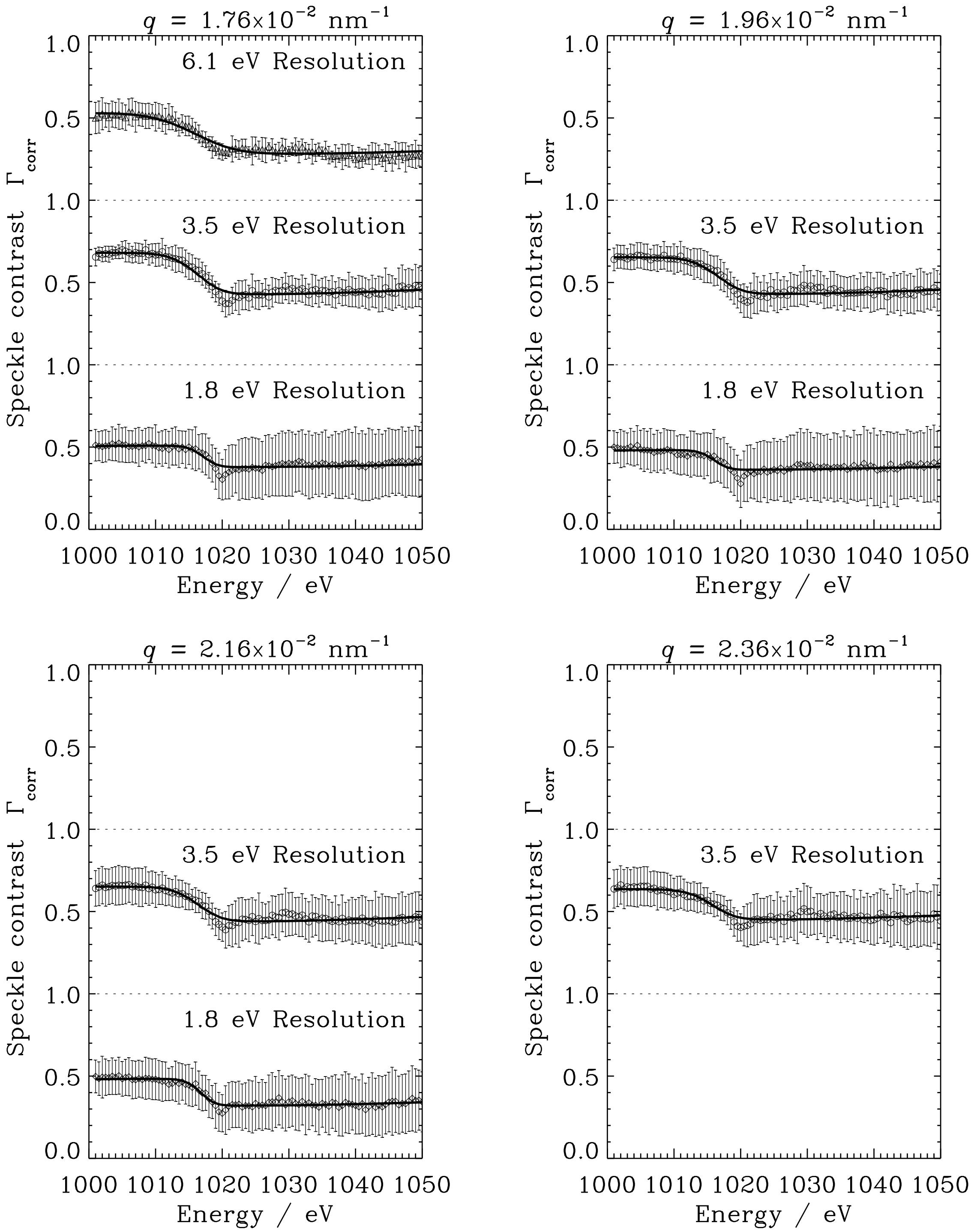

Figure 4.3: *(b) Speckle contrast as a function of energy at different q-positions for various energy resolutions. The symbols represent the measured speckle contrast. The solid lines are fits according to Eqs.* (4.1) *and* (3.6).

width of the integral, it was removed fom the integrals in Eq. (1.21), yielding Eq. (1.22). Using Eqs. (1.25) and (1.27) derived from Eq. (1.22) to calculate the speckle contrast, no variations at an absorption edge are expected. Near absorption edges however, $\langle I(k,r)\rangle_r$ may vary significantly with k. Thus, all the terms in Eq. (1.21) have to be taken into account to calculate the speckle contrast $\Gamma_W(r)$ of the isotropic speckle patterns, without further simplifications:

$$\Gamma_W(r) = \frac{\iint W(k_1)W(k_2)\,\left|\gamma_A(k_1,k_2,r)\right|^2\,\left\langle I(k_1,r)\right\rangle_r \left\langle I(k_2,r)\right\rangle_r\,\mathrm{d}k_1\,\mathrm{d}k_2}{\left[\int W(k)\,\left\langle I(k,r)\right\rangle_r\,\mathrm{d}k\right]^2} \quad . \tag{4.1}$$

Up to now, no analytical solution has been found for Eq. (4.1). Therefore, the speckle contrast was calculated numerically.

Eq. (4.1), evaluated at the different values of q and corrected for resolution effects by means of Eq. (3.6), was fit to the data, allowing for just three free parameters: E_0, an energy offset to allow for an energy miscalibration; ΔI, an intensity offset to allow for a spectral background level, due to parasitic scattering or higher order spectral contamination from the beamline monochromator; and T, the mean thickness of the sample. To account for the energy dependence of k in the sample, the usual expression $n = 1-\delta-i\beta$ for the complex index of refraction was used. Thus, the strongly energy-dependent part of $\langle I(k,r)\rangle_r$ had the simple form of

$$\left\langle I(k,r)\right\rangle_r \propto \exp(-2\beta kT) \quad , \tag{4.2}$$

and the normalized mutual amplitude correlation function

$$\gamma_A(k_1,k_2,r) \quad \longrightarrow \quad \gamma_A\big([1-\delta_1]k_1,[1-\delta_2]k_2,r\big) \quad . \tag{4.3}$$

δ and β are functions of k and were taken from the literature [HGD93, HVB$^+$75]. For the spectral response function $W(k)$, a Gaussian function around k_0 with standard deviation σ_k was used, where $2\sqrt{2\ln(2)}\,\sigma_k$ was the energy resolution of the beamline, i.e., 1.8 eV, 3.5 eV, or 6.1 eV. E_0 and ΔI were accounted for in the spectral response function via:

$$W(k) = \Delta I + \exp\left(\frac{[k-k_0-hc_0\,E_0]^2}{2\sigma_k^2}\right) \quad , \tag{4.4}$$

where $hc_0 = 1.2398\times10^{-6}$ eV·m, the product of Planck's constant and the speed of light, is needed to convert energies into wave numbers. A parallel processing algorithm was developed to fit the data (see Appendix D). The fits are in good overall agreement with the data. More detailed structure in the measured speckle contrast data may originate from near-edge fine structures in β, which are not reflected in the tabulated data of Henke and Hubbell [HGD93, HVB$^+$75].

Table 4.1 shows the resulting fit parameters. The q-dependence of these parameters can be seen in Figs. 4.4 through 4.6. The parameter E_0 can be considered as q-independent. $\Delta I/I_{\max}$ tends

(a)

$\frac{q}{10^{-2}\ \mathrm{nm}^{-1}}$	$\frac{E_0}{\mathrm{eV}}$	$\frac{\Delta I/I_{\max}}{\%}$	$\frac{T}{\mu\mathrm{m}}$	χ^2
0.96	4.2 ± 1.2	2.9 ± 0.2	0.12 ± 0.02	5.5
1.16	3.9 ± 1.2	1.8 ± 0.1	0.10 ± 0.02	5.2
1.36	4.5 ± 1.1	1.2 ± 0.1	0.12 ± 0.02	2.3
1.56	4.4 ± 1.1	1.3 ± 0.1	0.12 ± 0.02	2.1
1.76	4.7 ± 1.5	1.2 ± 0.1	0.09 ± 0.02	1.5
1.96	5.7 ± 2.2	1.3 ± 0.1	0.08 ± 0.02	1.6
2.16	5.2 ± 1.3	1.3 ± 0.1	0.11 ± 0.02	1.4

(b)

$\frac{q}{10^{-2}\ \mathrm{nm}^{-1}}$	$\frac{E_0}{\mathrm{eV}}$	$\frac{\Delta I/I_{\max}}{\%}$	$\frac{T}{\mu\mathrm{m}}$	χ^2
0.96	5.6 ± 0.5	1.8 ± 0.1	0.16 ± 0.01	38
1.16	5.8 ± 0.3	1.5 ± 0.1	0.16 ± 0.01	59
1.36	7.1 ± 1.0	1.1 ± 0.1	0.18 ± 0.03	15
1.56	7.1 ± 1.0	0.9 ± 0.1	0.21 ± 0.02	9.4
1.76	7.3 ± 0.7	0.9 ± 0.1	0.21 ± 0.01	7.7
1.96	6.9 ± 1.0	0.9 ± 0.1	0.18 ± 0.02	4.2
2.16	7.1 ± 0.9	0.9 ± 0.1	0.18 ± 0.02	3.2
2.36	7.4 ± 1.1	0.9 ± 0.1	0.15 ± 0.03	3.1

(c)

$\frac{q}{10^{-2}\ \mathrm{nm}^{-1}}$	$\frac{E_0}{\mathrm{eV}}$	$\frac{\Delta I/I_{\max}}{\%}$	$\frac{T}{\mu\mathrm{m}}$	χ^2
0.96	9.7 ± 0.6	5.1 ± 0.2	0.40 ± 0.01	68
1.16	11.4 ± 1.0	3.9 ± 0.2	0.21 ± 0.02	22
1.36	8.8 ± 1.3	3.6 ± 0.2	0.21 ± 0.02	7.5
1.56	9.0 ± 1.0	2.7 ± 0.2	0.23 ± 0.02	11
1.76	9.2 ± 0.9	2.5 ± 0.2	0.23 ± 0.02	18

Table 4.1: *Fit parameters for the speckle contrast measurements across the Zn L_{III} absorption edge as shown in Fig. 4.3. The values correspond to an energy resolution of (a)* 1.8 *eV, (b)* 3.5 *eV, and (c)* 6.1 *eV.* χ^2 *is the sum of the squares of the residuals weighted with the error of the measurement and the number of degrees of freedom in the fit.*

to be higher for small angles (low q) than for larger angles (high q). This can be due to the effect of higher order spectral contamination from the monochromator [JN87]. These higher-energy x-rays would be scattered at smaller angles 2θ, producing smaller speckles that cannot be resolved by the detector. Thus, an increased background at low q is expected. Except for the thickness derived for the smallest q-value in the measurement with the energy resolution of 6.1 eV, T can be considered as q-independent as well. For $q = 0.0096$ nm^{-1} in the low-energy-resolution measurement, T is significantly higher than the other values in this series. The quality of fit for this speckle contrast curve however was the worst of all fits (see Table 4.1 and Fig. 4.3 (a)). It is therefore difficult to judge the significance of this data point. An explanation for this value may be found in the performance of the CCD. For high signal levels, as especially expected for low energy resolution and low q, charge can leak from one pixel to the neighboring ones, thus apparently reducing the speckle contrast. Such an effect is not included in the parameter ΔI, since this parameter only accounts for an additional bias but not for reduced count rates close to saturation. A speckle contrast reduced due to this mechanism could be accounted for by the fit program via an increased thickness.

Table 4.2 gives the averages and variances of the fit parameters, averaged over the investigated q-space for each energy resolution. From these values, one can easily see that the energy calibration of the monochromator depends on the chosen energy resolution. As the energy resolution is determined by the size of the entrance and exit slits of the SGM, a slight offset in the center

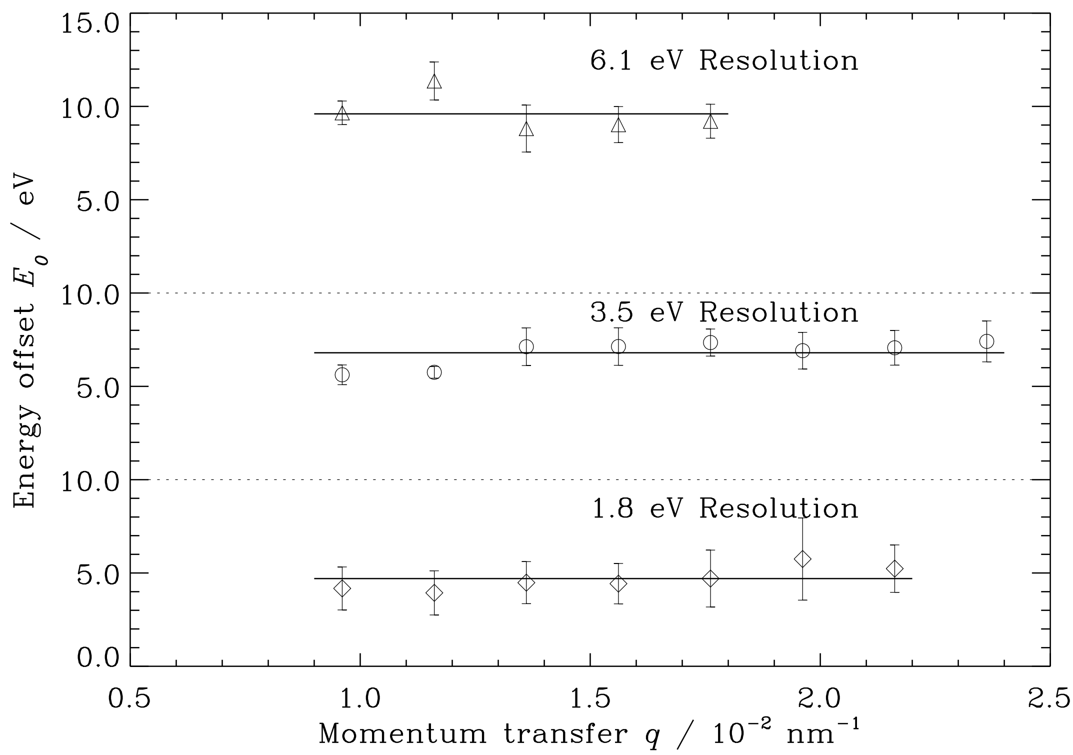

Figure 4.4: *q-dependence of the fit parameter E_0 from Table 4.1 for different energy resolutions. The solid lines indicate the average value.*

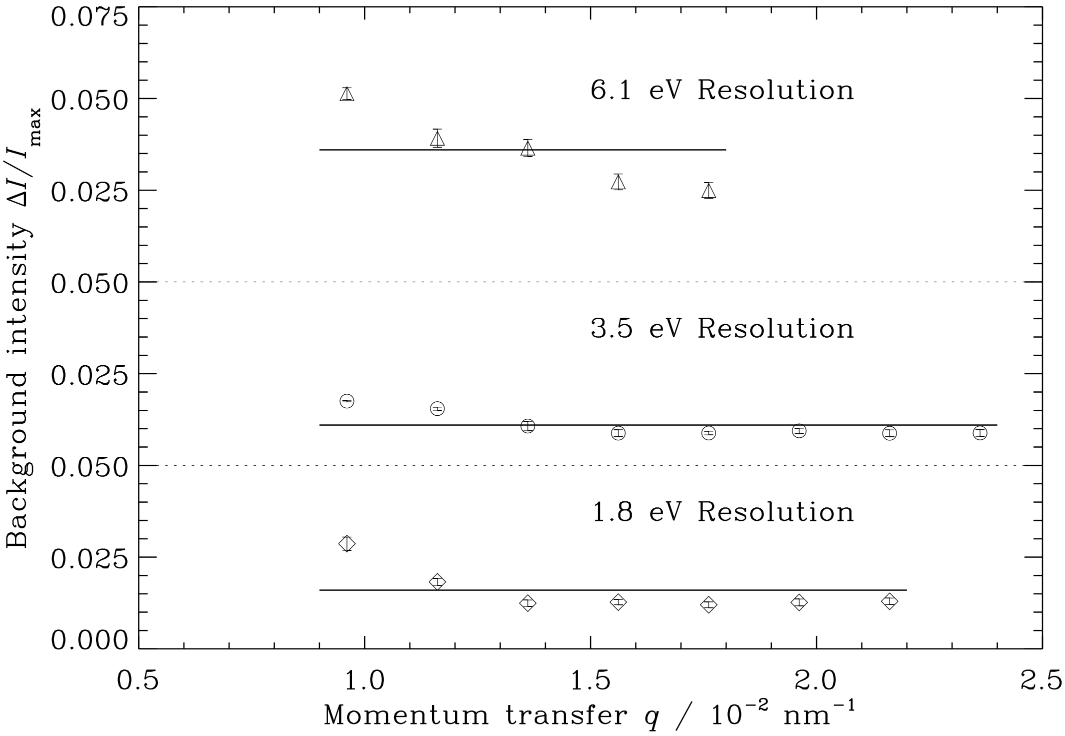

Figure 4.5: *q-dependence of the fit parameter $\Delta I/I_{\max}$ from Table 4.1 for different energy resolutions. The solid lines indicate the average value.*

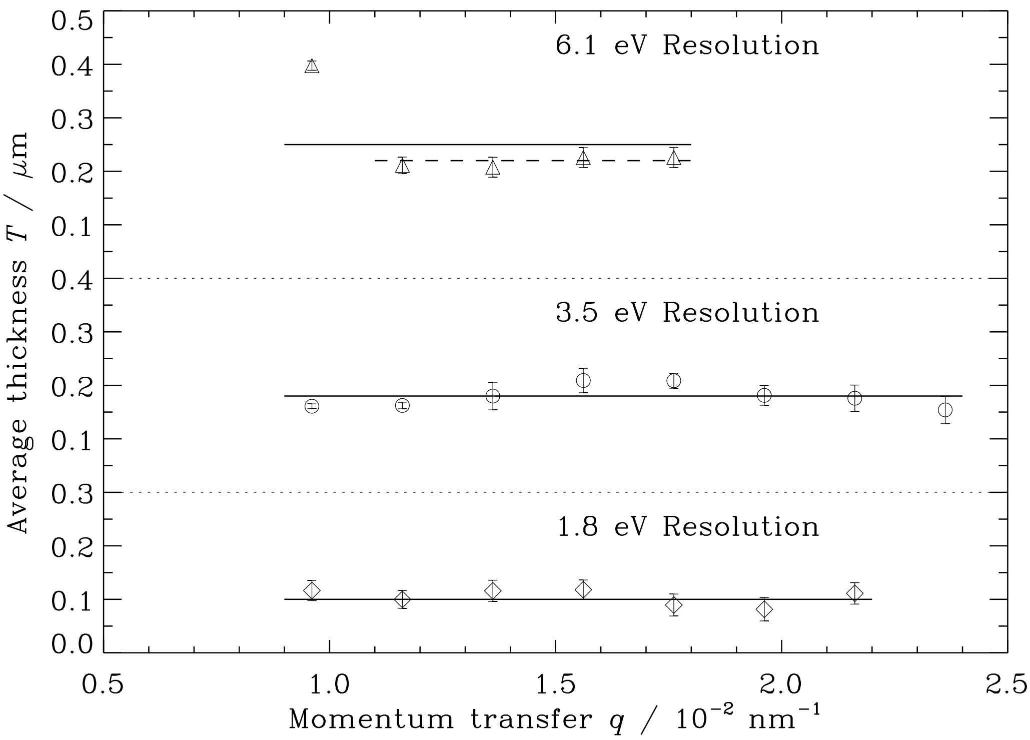

Figure 4.6: *q-dependence of the fit parameter T from Table 4.1 for different energy resolutions. The solid lines indicate the average value. The dashed line shows the average value for the energy resolution of* 6.1 *eV when the value for lowest q is neglected.*

Resolution / eV	q / 10^{-2} nm^{-1}	T / μm	E_0 / eV	$\Delta I/I_{\max}$ / %
1.8	1.6 ± 0.4	0.10 ± 0.01	4.7 ± 0.6	1.6 ± 0.6
3.5	1.7 ± 0.5	0.18 ± 0.02	6.8 ± 0.7	1.1 ± 0.3
6.1	1.4 ± 0.3	0.22 ± 0.02[a]	9.6 ± 1.0	3.6 ± 1.1

Table 4.2: *Averages and variances in q of the fit parameters from Table 4.1.*

[a]The value for lowest q was excluded from this average.

position of the beam axis with respect to the location of these slits can easily cause such a miscalibration. Since the x-ray energy is not distributed homogenously across the slits of an SGM [Mic86], such a miscalibration may be enhanced for larger slit settings, i.e., poorer energy resolution. The energy miscalibration derived from the fit lies between 4.7 eV and 9.6 eV, which is larger than the respective energy resolution.

The background intensity ΔI was less than 4% of the maximum intensity. The largest values are found for lower energy resolutions. This may be understood as originating from an increased contribution of parasitic scattering admitted by the larger slit settings to pass through the experiment or from a higher degree of higher-order contamination from the monochromator passing these larger slits.

The measurements with different energy resolutions were taken at different sample positions. Therefore, the fitted thicknesses T differ slightly from each other. Still, the values for the measurements at the three different energy resolutions are similar, being approximately 0.11 to 0.23 times the absorption length in Zn below and approximately 0.8 to 1.7 times the absorption length above the edge,* which agrees well with the total transmitted intensity measurement (Fig. 4.2).

A dependence on the real part of the complex index of refraction δ was not found in the measured speckle contrast. This, as well as the dependence on β, can be understood by considering Young's double-slit experiment with different levels of transmission through each of the two slits. Figure 4.7 shows the geometry of this experiment. The time-averaged intensity $I(P)$ at a point P in the plane of observation is given by:

$$\begin{aligned} I(P) &= I^{(1)}(P) + I^{(2)}(P) \\ &\quad +2\sqrt{I^{(1)}(P) + I^{(2)}(P)}\left|\mu_{12}\left(\frac{r_2 - r_1}{c_0}\right)\right| \\ &\qquad \times \cos\left(kc_0\left[\frac{r_2 - r_1}{c_0}\right] - \alpha_{12}\left(\frac{r_2 - r_1}{c_0}\right)\right) \quad , \end{aligned} \tag{4.5}$$

*The thickness value at $q = 0.96 \times 10^{-2}$ nm^{-1} for the energy resolution of 6.1 eV was excluded in this comparison.

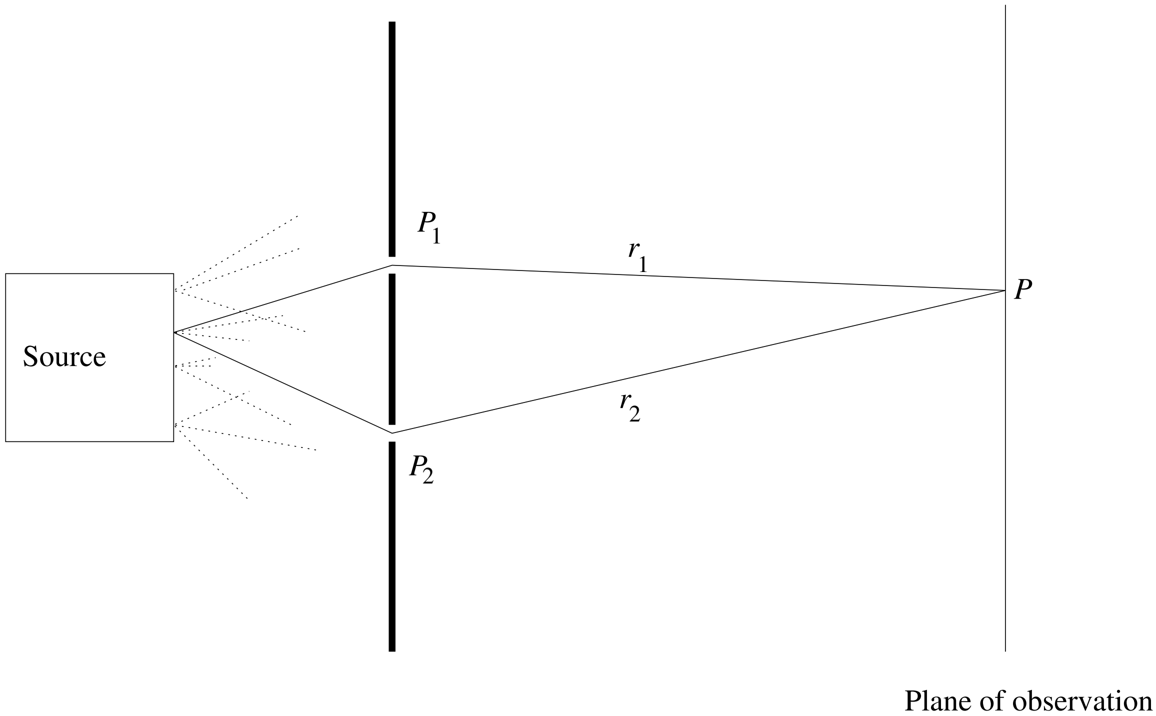

Figure 4.7: *Notation used to describe Young's double-slit experiment.*

where $I^{(1)}(P)$ and $I^{(2)}(P)$ are the intensities at P produced by slit 1 or slit 2 alone, respectively. $|\mu_{12}(\tau)|$ is the complex degree of coherence across the distance between S_1 and S_2, with the time retardation $\tau = \frac{r_2 - r_1}{c_0}$ between the two rays. α_{12} is a phase factor related to the fields at S_1 and S_2. r_1 and r_2 are the paths from one point of the source to the plane of observation as indicated in Fig. 4.7. Goodman [Goo85] defines the visibility $\mathcal{V}$ of this fringe pattern as:

$$\mathcal{V} \equiv \frac{I_{\max} - I_{\min}}{I_{\max} + I_{\min}} = \frac{2\sqrt{I^{(2)}/I^{(1)}}}{1 + I^{(2)}/I^{(1)}} \mu_{12}(0) \quad . \tag{4.6}$$

From this, one can see that different phase shifts across the two slits may result in a positional shift of the fringe pattern due to α_{12}, with no effect on the visibility. However, different intensities at the two slits result in decreased visibility.

In the speckle experiments presented here, the differences in transmitted intensities between optically thicker and optically thinner parts of the sample are smaller on the transmissive side of the edge than on the absorptive side. In other words, the increased absorption on the absorptive side of the edge enhances the effect of the different optical thicknesses in the disordered sample. Therefore, the ratios between the transmitted intensities are closer to 1 on the transmissive than on the absorptive side:

$$\frac{\exp(-2k\beta_1 \Delta T)}{\exp(-2k\beta_2 \Delta T)} < 1 \quad , \quad \text{for} \quad \beta_1 > \beta_2 \quad , \tag{4.7}$$

where ΔT denotes an optical thickness difference. This change in relative intensities, originating from a change in β, dominates the speckle contrast. In all the measurements, a decrease in speckle contrast at the absorption edge was observed, consistent with the variation in transmitted intensity across the sample being more pronounced on the absorptive side of the edge (Eq. (4.7)).

Note that the optical thickness *variation* over the disordered sample and the intensity distribution produced thereof is the driving factor for the speckle contrast variation. Control measurements to investigate the Zn-powder speckle contrast across the Al K-absorption edge (1559 eV) of a uniform ~ 700-nm-thick Al filter introduced into the beam did not show any edge-like variation in speckle contrast (Fig. 4.8). There is some variation in q (different values of q are plotted with different symbols); the energy dependence, however, is flat overall, even though the intensity in the recorded speckle images changed, consistent with the changing absorption by the Al filter. This is in agreement with the earlier statement that the analysis is independent of the intensity incident on the sample.

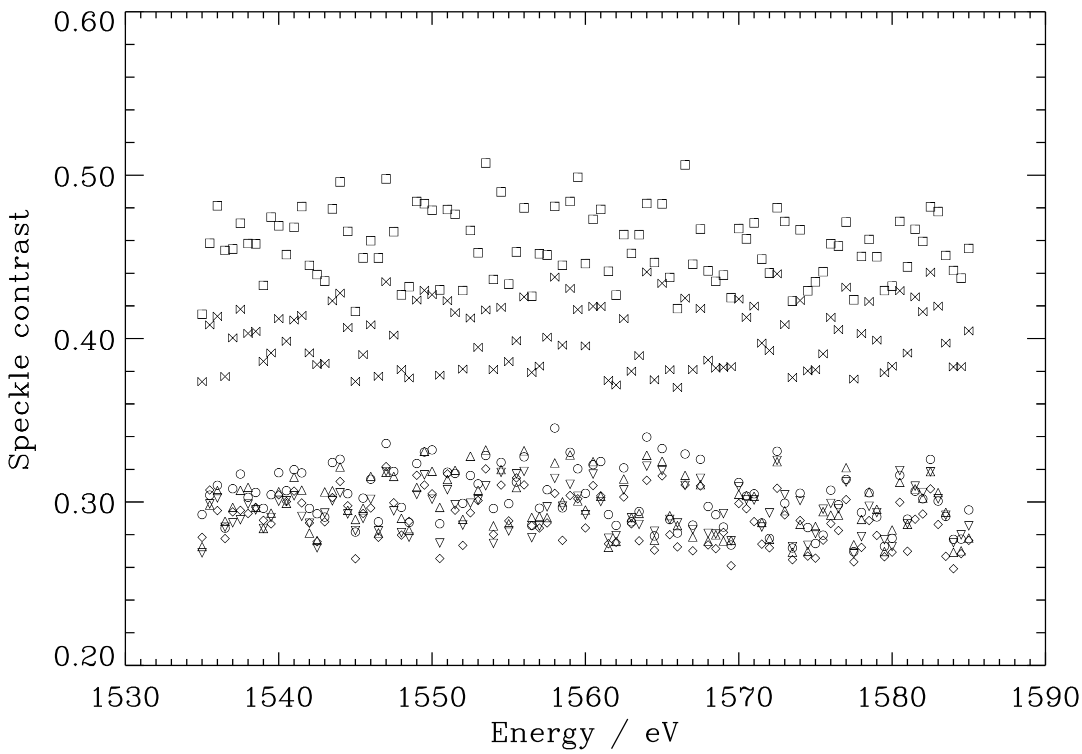

Figure 4.8: *Speckle contrast from the Zn sample across the Al K-edge at different values of q. The symbols* $[\square, \bowtie, \bigcirc, \Diamond, \triangledown, \triangle]$ *correspond to values of* $q = [0.91, 1.39, 1.87, 2.36, 2.84, 3.32] \times 10^{-2}$ *nm*$^{-1}$.

4.5 Summary

The speckle contrast as a function of the incident energy was found to be reduced at a sample-specific absorption edge. Measurements were done at different energy-resolution settings. A commonly made simplification in the calculation of speckle contrast neglects the influence of the dependence of the transmitted intensity on the wave number. Following this approach, as presented in Chapter 1.2, the observed speckle contrast variations could not be explained. Thus, fits according to a more fundamental model of speckle contrast calculation were presented. They agree well with the data, relying on only three fit parameters of which two described instrumental properties of the experiment, such as energy calibration and background scattering, and one was the average sample thickness. The q-dependence and energy-resolution dependence of these fit parameters could be explained. The accuracy of the fits relied however on the accuracy of tabulated values for the index of refraction. Therefore, the overall behavior of the data is well understood, whereas the reconstruction of finer structural details in the measured speckle contrast curves requires a more precise knowledge of the index of refraction. A qualitative understanding of the measured speckle contrast was given in terms of Young's double-slit experiment: in the same way fringe visibility in Young's double-slit experiment is influenced by the ratio of the transmitted intensities in the two slits, the speckle contrast is influenced by the distribution of the transmitted intensity across the randomly absorbing sample. This distribution changes its variance with varying imaginary part β of the complex index of refraction $n = 1 - \delta - i\beta$. With increasing β, the variation in transmitted intensity across the sample increases, therefore decreasing the speckle contrast. Thus, the energy dependence of β dominates the speckle contrast. In order to verify that the overall absorption observed at the edge was not responsible for the speckle contrast reduction, control measurements were done in which the speckle contrast was measured across the absorption edge of a filter material introduced into the beam. The filter material was not present in the sample. No speckle contrast variation could be observed. This result agrees with the prediction by the theory.

Chapter 5

Dynamics of Low-Density Aerosil Dispersed in Octylcyanobiphenyl

The use of speckle methods to probe the dynamics of a sample is already well established in the visible light regime. In Chapters 3 and 4 it was demonstrated that the speckle contrast achieved in the experiments at the 2-ID-B beamline is high, which is essential for obtaining meaningful results when measuring sample fluctuations. This chapter presents measurements of the silica dynamics in an octylcyanobiphenyl liquid-crystal – silica-aerosil dispersion. Such systems constitute good physical models of quenched random disorder effects for a variety of phase transitions. They have attracted considerable theoretical [RT99] and experimental [PLB$^+$01, BRTC01, HBT01] efforts. The presented measurements allow in particular a better understanding of the known cross-over behavior in low-density-aerosil dispersions towards $3d$-XY universality.

5.1 Samples

As indicated in Chapter 1.3, the temporal fluctuations observed in a series of speckle images may not only reflect sample dynamics but also fluctuations present in the experimental setup. Thus, a careful analysis of the latter had to be done. In this chapter, measurements using a reference sample in order to characterize the setup are described, as well as measurements on the octylcyanobiphenyl – aerosil dispersion.

5.1.1 Reference Sample

Aerosil type-300 from Degussa [Deg] was used as a reference sample material. This aerosil consisted of 7-nm-diameter SiO_2 spheres with a high density of hydroxyl groups covering their surfaces. The surface area, derived from the BET method of nitrogen adsorption isotherms

[BET38, Hil46, Hil49], was given by the manufacturer as $a = 300\ \mathrm{m^2/g}$, and the FWHM particle size distribution as ~ 7.5 nm. However, Iannacchione *et al.* [IGMR98] found by SAXS studies that the spheres of this aerosil do not exist individually. Instead, 7 nm was probably the size of basic spherical nodules that were weakly fused together during the manufacturing process. The smallest observed actual building block had a size of ~ 20 nm, or 3 fused nodules. These building blocks agglomerated by hydrogen bonds to sizes of up to ~ 400 nm. The sample was prepared, similar to the sample in Chapter 4, by sprinkling the aerosil on a sample cell of type A (see Chapter 2.3) and shaking off the excess. Thus, a thin, self-supporting, random distribution of aerosil-gel electrostatically adhering to the silicon-nitride membrane of the holder was achieved. The coverage appeared uniform but the density of silica for this sample was not known.

5.1.2 Octylcyanobiphenyl – Aerosil Dispersion

This sample was based on a dispersion of aerosil in a liquid-crystal. Liquid-crystals are materials that do not show a single transition from the crystalline to the liquid state but rather a cascade of transitions involving intermediary phases. A very brief introduction to liquid-crystals will be given here, for more information see, e.g., [GP95, Cha92].

A crystal has long-range order in three dimensions, both in position and orientation. The occurrence of the elementary building blocks (atoms, molecules, ...) in space is generally fixed with respect to location and orientation within some margins. On the other hand, in an isotropic liquid, positions as well as orientations of such building blocks are not strictly fixed in space. Hence, there is no long-range order. Knowing the pattern at one point does not necessarily help in predicting the pattern at another point in space.

The phases assumed by liquid-crystalline materials have symmetry properties that lie between those of the crystalline and the liquid state, so-called mesomorphic states. Liquid-crystals behave like liquids in some respects and like crystals in others. For example, a liquid-crystal can exhibit:

- anisotropy without translational symmetry with two different correlation lengths in perpendicular directions. For asymmetric molecules, this can, e.g., be given by an orientational alignment of the molecules. Such a phase is called the *nematic* phase (Fig. 5.1).
- translational symmetry in one direction of space but not in the others. This phase can be imagined as a stack of liquid layers. Such a phase is called the *smectic* phase.
- translational symmetry in two dimensions but not in the third. This can be described as an ensemble of tubes containing liquid aligned in a two-dimensional array. Such a phase is called the *columnar* phase.

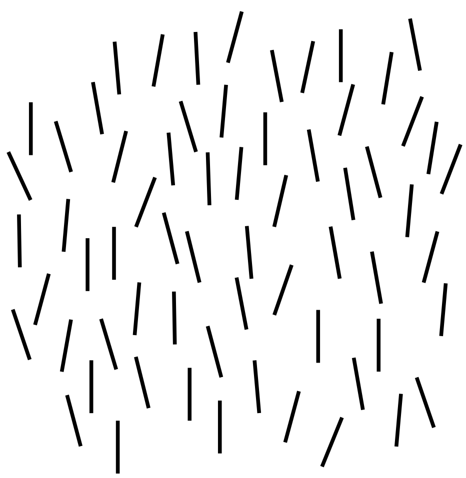

Figure 5.1: *Nematic phase.*

In most cases, different liquid-crystal states can be achieved by changing the temperature (*thermotropic* liquid-crystals), in other cases, by changing the concentration of the molecules (*lyotropic* liquid-crystals). Substances known to form liquid-crystals are mostly organic.

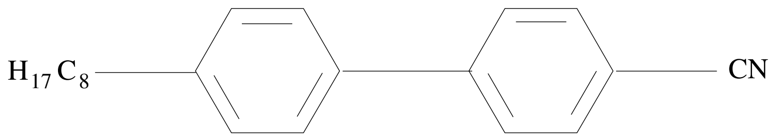

Figure 5.2: *Octylcyanobiphenyl (8CB).*

The chemical structure of the organic liquid-crystal used for the measurements described in this chapter, octylcyanobiphenyl (8CB), can be seen in Fig. 5.2. The molecule is approximately $l = 2$ nm long and 0.5 nm wide, the cyanobiphenyl part being hydrophilic and rigid, while the alkyl chain is hydrophobic and flexible, like a wiggling tail. Pure 8CB is a thermotropic liquid-crystal and shows the following phase transitions*:

$$\mathrm{Cr} \xleftrightarrow{22.0\ ^\circ\mathrm{C}} \mathrm{SmA_d} \xleftrightarrow{33.8\ ^\circ\mathrm{C}} \mathrm{N} \xleftrightarrow{40.8\ ^\circ\mathrm{C}} \mathrm{I},$$

where Cr stands for crystalline, $\mathrm{SmA_d}$ for smectic type $\mathrm{A_d}$, N for nematic, and I for the isotropic phase. These phase transitions occur at temperatures not too far above room temperature, thus facilitating sample temperature control. The smectic phase is of type $\mathrm{A_d}$, which is one special form of smectic ordering among many possible smectic phases. $\mathrm{SmA_d}$ (see Fig. 5.3) has the following properties:

*These values were obtained by measuring the heat capacity and the enthalpy in the liquid-crystal [TMD82].

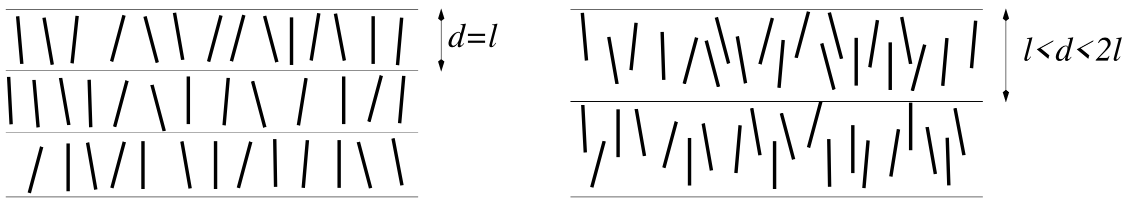

Figure 5.3: *Smectic*-A_1 *phase,* $d = l$*, (left) and smectic*-A_d *phase,* $l < d < 2l$*, (right).*

- a layer structure with a layer spacing d, here $d = 3.2$ nm, greater than the molecular length l, here $l = 2$ nm, but less than the thickness $2l$ of a bilayer;†
- no long-range order of the centers of gravity within each layer;
- optical uni-axiality with an optical axis, z, normal to the plane of the layers, and rotational symmetry around this axis, i.e., the layer normal is parallel to the average orientation axis of the molecules; this orientation defines the director $\vec{n}$ of the molecule;
- equivalent directions z and $-z$.

According to the mean-field theory [GP95, Cha92], the width of the temperature range over which the liquid-crystal exists in the nematic phase influences the nature of the smectic-A-to-nematic phase transition. In 8CB, the nematic phase exists over a range in temperature of ~ 7 °C. A second-order phase transition from the smectic-A_d to the nematic phase is predicted as well as observed experimentally [TMD82]. Mathematically, this can be explained by the coupling between the complex smectic order parameter (the density wave of the material) and the real nematic ordering parameter (the average quadrupole moment of the alignment [GP95]). A second-order phase transition is expected to exhibit a critical *slowing down* of thermal fluctuations, i.e., increased relaxation times [BCS95, Chu85, GK80]. Still, the majority of relaxation processes in the system is expected to happen on subsecond time scales. The crystalline-to-smectic-A_d transition and the nematic-to-isotropic phase transitions are known to be of first order [TMD82]. No slowing down is expected at these transitions.

Because smectic liquid-crystals can be thought of as two-dimensional liquids in three dimensions, they should belong to the $3d$-XY universality class of critical phenomena [GP95]. For a phase transition belonging to the $3d$-XY universality class, such as the smectic-A-to-nematic phase transition, which is dominated by ordering of the smectic phase, the Landau theory [GK80] predicts a critical exponent α for the heat capacity $\Delta C_p \propto |t|^{-\alpha}$ with $\alpha = -0.0079$. 8CB however, exhibits a critical exponent of $\alpha \approx 0.3$. This indicates the presence of large fluctuations of the smectic order parameter, which have to be small for the Landau theory to be valid.

†If $d = l$, the phase is called SmA_1, for $d = 2l$, SmA_2.

The investigated system was a dispersion of this liquid-crystal with particles of silica aerosil. It was provided by G. S. Iannacchione from the Department of Physics at Worcester Polytechnic Institute [Ian]. It was prepared by dissolving the 8CB [Mer] in acetone, adding the desired amount of aerosil powder, and then sonicating the mixture to achieve a good dispersion. The solvent was then evaporated off slowly, first at 60 °C and then at 90 °C at slightly subatmospheric pressure. More details about the preparation method can be found in [HG97, IGMR98]. The same aerosil type 300 from Degussa [Deg] as described above was used and an aerosil density of $\rho = 0.06$ g(sil)$/$cm^3(total) was chosen. For this density, a volume fraction of 'pores' (i.e., of 8CB between the aerosil chains) of $1 - \rho/\rho_{\mathrm{SiO_2}} = 0.973$, where $\rho_{\mathrm{SiO_2}} = 2.2$ g/cm^3 is the density of bulk SiO_2, and an average pore size (i.e., 8CB length scale) of $\frac{2}{a}[\rho^{-1} + \rho^{-1}_{\mathrm{SiO_2}}] = 108$ nm are expected. The fraction of 8CB molecules anchored on the aerosil particles should be 0.036 [IGMR98].

Aerosil systems are particularly interesting since random disorder is introduced in a controlled manner. The aerosil forms a weakly connected, thixotropic[‡] network gel. Because of its high surface density of hydroxyl groups, the aerosil can easily form long hydrogen-bonded strands in an organic medium, such as 8CB [Deg, SS87]. These chains can break under stress and reform quickly on time scales < 1 s when the stress is removed. Still, without stress, the aerosil gel is very stable for densities as low as 0.022 g(sil)$/$cm^3(total), even in the isotropic phase of 8CB [IGMR98].

Static elastic strains in the smectic and nematic phases and strains due to dislocations, arising from the random distribution of silica strands, are expected to partially anneal spontaneously in these systems without a change in the average distribution of the aerosil. As the aerosil is covered with hydroxyl groups, the 8CB molecules orient perpendicular to its surface, forming hedgehog-like configurations. This coupling between the aerosil strands and the director of the 8CB molecules directly adjacent to the hydrophilic aerosil particles produces a surface field. Local orientational disorder related to this surface field cannot be annealed by local rearrangement of the aerosil particles.

Recently, the observation of a cross-over behavior in 8CB – aerosil dispersions was reported for $\rho \lesssim 0.1$ g(sil)$/$cm^3(total) [IGMR98]. For larger densities, the dispersion forms a *stiff* gel with the aerogel-like behavior of forcing more-or-less rigid boundariy conditions onto the liquid-crystal. The system under study here forms a *soft* gel. The following effects of this type of aerosil dispersion on the liquid-crystal are known:

- At the smectic-$\mathrm{A_d}$-to-nematic phase transition, a quenched random surface field with quasi-annealed elastic strain is found. The critical behavior evolves towards $3d$-XY universality, i.e., the critical exponent α approaches zero with increasing

[‡]Thixotropic means density-dependent.

$\rho < 0.1$ g(sil)/cm^3(total). The phase transition temperature for $\rho = 0.06$ g(sil)/cm^3(total) is lowered to ~ 33.0 °C.

- At the nematic-to-isotropic phase transition, the effects of a quenched random surface field and long-range elastic strain deformations are observed. The phase transition temperature for $\rho = 0.06$ g(sil)/cm^3(total) is lowered to ~ 40.0 °C.

- In silica aero*gel*[§] systems with a density comparable to that used here, the crystalline-to-smectic-A$_\mathrm{d}$ transition is substantially suppressed and shifted to lower temperatures [CBM$^+$93]. Therefore, a significant decrease in the phase transition temperature is expected for aerosil systems as well. Initial measurements of the freezing temperature in low-density 8CB – aerosil systems indicate that a suppression of the phase transition down to $\lesssim 17$ °C for $\rho = 0.06$ g(sil)/cm^3(total) can be expected [Ian01].

Samples were prepared with cells of type B and C (see Chapter 2.3) in order to prevent the hydrophilic system from absorbing water. Of interest for the present study is the effect of the low-density aerosil on the long time-scales (minutes) corporative-mode dynamics in the system as those have not yet been studied in these systems. Some years ago, visible-light scattering studies were done on 8CB trapped in rather high-density aero*gel* [WGLX92]. The reported results show temperature-dependent slow relaxations of high complexity with relaxation times on the order of at least seconds. Such relaxation modes were not found in pure 8CB. Similar slow dynamics in 8CB – aero*sil* systems might reveal the underlying mechanism for the known cross-over behavior.

5.2 Measurement Technique

The sample holder (see Chapter 2.3) was connected to a recirculating chiller for temperature control. Time series of CCD images (frames) were recorded at different temperature settings. The calibration of the temperature settings and the accuracy to which the temperature at the sample could be determined has already been described in Chapter 2.3. Temperatures chosen for the dynamics measurements on the 8CB – aerosil sample are given in Table 5.1.

In addition, two reference time series were recorded with the pure, self-supporting aerosil-gel sample: one series with the chiller switched off, and one series with the chiller operating at room temperature ($\sim$ 22 °C). At the start and end of each time series, a dark image was acquired to allow for the appropriate dark count correction throughout the complete series as described in the following section.

[§] Aero*gel*, compared to aero*sil*, does not consist of hydroxyl-covered spheres building hydrogen bonds but is a dried gel of oxide particles that are directly linked in three dimensions.

t_{sample}	17.2 °C	21.4 °C	26.6 °C	32.0 °C	35.0 °C	38.6 °C	42.5 °C
Phase	Cr $\leftrightarrow$ SmA_d	SmA_d	SmA_d	SmA_d $\leftrightarrow$ N	N	N $\leftrightarrow$ I	I

Table 5.1: *Chosen temperature settings and the corresponding phases of the 8CB – aerosil dispersion. Temperatures were labeled as phase transition temperatures if they were within ~ 1 °C from the expected phase transition in the dispersion.*

An x-ray energy of 1830 eV, just below the Si K-absorption edge (1839 eV), was chosen for the experiments in order to achieve high speckle contrast from the silica in the system. As the upper limit for fluctuation contrast is given by the speckle contrast (see Chapter 1.3), the pinhole setup, shown to produce high-contrast speckles, was used. A 10-μm-diameter pinhole was chosen. The detector was placed near on-axis position with a sample-to-detector distance of 975 mm. The calculated energy resolution used for this experiment was 14 eV. With this, the maximum optical path length difference was on the order of the longitudinal coherence length $\lambda^2/\Delta\lambda$. Therefore, the stringent criterion of quasi-monochromaticity (see Chapter 1.2) was not satisfied. Still reasonable speckle contrast was expected [TM98].

A q-range of 0.02 nm^{-1} to 0.05 nm^{-1} was probed. This relates to length scales of 126 nm to 314 nm in the system. These length scales are significantly bigger than the molecular and crystalline length scales of pure 8CB, ensuring that relaxations on lengths scales corresponding to the aerosil rather than the liquid-crystal were probed. As a further indication that the speckles measured with the dispersion sample originated from the aerosil, a pure 8CB sample was investigated. No speckles were detected from this sample. This indicates that the scattering cross section of the organic material was relatively much smaller. Only with extremely long exposures of the CCD (20 minutes) could the signal arising from the 8CB layer spacing in the smectic phase (at $q \approx 1.96$ nm^{-1}) be detected with an average count of one photon per pixel of the CCD camera. Therefore the data presented in the following sections result almost exclusively from the scattering of the aerosil.

5.3 Data Reduction Method

Extending the method of intensity fluctuation spectroscopy to x-rays, longer correlation times, and area detectors introduces new challenges of low signal levels and short data batches (limited amount of data). Collecting two-dimensional data sets with area detectors is adventageous if nonergodic systems are studied because ensemble averages can be approximated by azimuthal averages of the recorded signal. Efficient data reduction methods were developed to extract meaningful information within a reasonable amount of time from the huge amount of data resulting from recording time series of 10^5 or more detector channels in parallel. The treatment presented here will follow suggestions found in [LLMS00, Sch90].

The background correction of the recorded images $I_{0,f}(\vec{p})$ $(0 \leq f < N)$ in a time series of N images was done in a way similar to that described in Chapter 3.3. Here, two single dark images $I_{\mathrm{d_{start}}}(\vec{p})$ and $I_{\mathrm{d_{end}}}(\vec{p})$, recorded directly before and after the time series of N data frames, respectively, were used to relate the master dark image $I_{\mathrm{d_m}}(\vec{p})$ to a dark image $I_{\mathrm{d}_f}(\vec{p})$ corresponding to the data image $I_{0,f}(\vec{p})$:

$$I_{\mathrm{d}_f}(\vec{p}) = \frac{I_{\mathrm{d_m}}(\vec{p})}{\langle I_{\mathrm{d_m}}(\vec{p})\rangle_{[\vec{p}\,\epsilon A_{\mathrm{det}}]}} \frac{1}{N} \left[[N-f] \left\langle I_{\mathrm{d_{start}}}(\vec{p}) \right\rangle_{[\vec{p}\,\epsilon A_{\mathrm{det}}]} + f \left\langle I_{\mathrm{d_{end}}}(\vec{p}) \right\rangle_{[\vec{p}\,\epsilon A_{\mathrm{det}}]} \right] \quad , \tag{5.1}$$

where again A_{det} is the area of the whole detector and $\vec{p}$ indicates the position of a pixel on the area detector. Thus, a dark image corresponding to each recorded image $I_{0,f}(\vec{p})$ in the series was derived, essentially by linear combination of the two measured dark images. This dark image $I_{\mathrm{d}_f}(\vec{p})$ was subtracted from the corresponding data image on a pixel-by-pixel basis yielding the dark-corrected image $I_f(\vec{p})$.

For the time analysis, first the average size of a speckle D_{speckle} in real space in the images $I_f(\vec{p})$ $(0 \leq f < N)$ was determined using the formalism described in Chapter 3.3. Then, square boxes, denoted with an index b, with area $A_b \approx D^2_{\mathrm{speckle}}$ were selected to cover the preprocessed speckle image in rings centered on the direct beam location ($q = 0$). The calculation of the spatial mean value $\mathcal{I}_f(\vec{p}_b) = \langle I_f(\vec{p})\rangle_{[\vec{p}\,\epsilon A_b]}$ in each box led to a reduction of the pre-processed data since the resulting data set contained approximately only one value per speckle-sized area. $\vec{p}_b$ is the location of the center pixel within the area A_b. This reduced data set $\mathcal{I}_f(\vec{p}_b)$ was then correlated across the time series of N images with spacing of Δt in time.

The normalized and baseline-subtracted temporal autocorrelation function $g_2(\tau, \vec{q})$ is given by Eq. (1.29):

$$g_2(\tau, \vec{q}) = \frac{\left\langle I(t, \vec{q})\, I(t+\tau, \vec{q}) \right\rangle_t}{\left[\left\langle I(t, \vec{q}) \right\rangle_t \right]^2} - 1 \quad . \tag{5.2}$$

In the present notation for the area detector, this transforms into

$$g_2(\tau_j, \vec{p}_b) = \frac{\dfrac{1}{N-j} \displaystyle\sum_{f=0}^{N-1-j} \mathcal{I}_f(\vec{p}_b)\mathcal{I}_{f+j}(\vec{p}_b)}{\mathcal{N}_{\mathrm{l}}(j, \vec{p}_b)\; \mathcal{N}_{\mathrm{r}}(j, \vec{p}_b)} - 1 \quad , \tag{5.3}$$

where $\mathcal{N}_{\mathrm{l}}(j, \vec{p}_b)$ and $\mathcal{N}_{\mathrm{r}}(j, \vec{p}_b)$ are the symmetric normalization factors given by [Sch90]

$$\begin{aligned} \mathcal{N}_{\mathrm{l}}(j, \vec{p}_b) &\equiv \tfrac{1}{N-j} \textstyle\sum_{f=0}^{N-1-j} \mathcal{I}_f(\vec{p}_b) \quad , \\ \mathcal{N}_{\mathrm{r}}(j, \vec{p}_b) &\equiv \tfrac{1}{N-j} \textstyle\sum_{f=j}^{N-1} \mathcal{I}_f(\vec{p}_b) \quad . \end{aligned} \tag{5.4}$$

j indexes the lag time $\tau_j = j\Delta t$, and $\vec{p}_b = [p_{b,x}, p_{b,y}]$ can be transformed into a position $\vec{q}_b$ in reciprocal space by

$$\vec{q}_b = \frac{k}{\sqrt{|\vec{p}_b|^2 + R_{\rm det}^2}} \left[p_{b,x}\ ,\ p_{b,y}\ ,\ R_{\rm det} - \sqrt{|\vec{p}_b|^2 + R_{\rm det}^2} \right] \ . \tag{5.5}$$

The symmetric normalization given by Eq. (5.4) was shown to produce better results for finite averaging (or recording) time Δt, especially in the regime of short data batches¶ [LLMS00, Sch90]. Therefore, the standard normalization of $\mathcal{N}_{\rm l}(\vec{p}_b) = \mathcal{N}_{\rm r}(\vec{p}_b) = \frac{1}{N}\sum_{f=0}^{N-1} \mathcal{I}_f(\vec{p}_b)$ was not used in the data analysis.

As an additional way to improve the statistical analysis of the results, the *multiple-tau* method [Sch90] was employed. This method predicts optimum signal-to-noise ratios if the recording time Δt is increased logarithmically with the lag time τ_j. In conjunction with the symmetric normalization scheme, introduced above, the use of increasing recording times leads to greatly enhanced accuracy in the detection of slow components with low intensity. It also helps to establish a reliable baseline of the time autocorrelation function. The increase in recording time causes a proportional increase in the mean number of photons counted per recording time and thus quickly reduces the photon detection noise contributions. The multiple-tau method was implemented by replacing $\mathcal{I}_f(\vec{p}_b)$ in Eqs. (5.3) and (5.4) with the average

$$\mathcal{I}_{\bar{f}(n)}(\vec{p}_b) \equiv \frac{1}{2^n} \sum_{\phi=f}^{f+2^n-1} \mathcal{I}_\phi(\vec{p}_b) \ , \tag{5.6}$$

so that the effective recording time equaled $\Delta t_n = 2^n\,\Delta t$. Schätzel [Sch90] suggested doubling the recording time every $L = 8$ channels: The first $2L$ channels of the autocorrelation function (lag times τ_j from 0 to $[2L-1]\Delta t$) were thus calculated with $\mathcal{I}_{\bar{f}(n)}(\vec{p}_b) = \mathcal{I}_f(\vec{p}_b)$, i.e., $n = 0$. The other channels of the autocorrelation function were calculated for lag times $\tau_j = j\,\Delta t_n$ with $L\,\Delta t_n < j\Delta t_n < [2L-1]\Delta t_n$ and sample times Δt_n, $(n \geq 1)$, i.e., $\mathcal{I}_{\bar{f}(n)}(\vec{p}_b)$ as given in Eq. (5.6). Thus, a quasi-logarithmic lag time scale with uniform average density in $\log(\tau)$ was achieved.

The above procedure yielded an autocorrelation function for every single speckle-sized box b in the recorded image. To avoid problems resulting from possible nonergodicity of the sample system and to improve statistics, azimuthal averages of the autocorrelation functions were calculated according to

$$\bar{g}_2(\tau_j, \bar{p}) \equiv \sum_{b\,\epsilon A_{p_l,p_m}} g_2(\tau_j, \vec{p}_b) \ , \tag{5.7}$$

where A_{p_l,p_m} is a ring-shaped region between two radial distances from the direct beam, p_l and p_m. The sum extends over all boxes b within this region. The resulting average was asigned to

¶ ‘Short’ in this context means up to only a few hundred collected data frames.

the average distance within A_{p_l,p_m} from the direct beam, which was $\bar{p} = [p_l + p_m]/2$. p_l and p_m were chosen such that the total recorded intensity

$$\mathcal{I}_{A_{p_l,p_m}}(\bar{p}) \equiv \sum_{f=0}^{N-1} \sum_{b \, \epsilon A_{p_l,p_m}} \mathcal{I}_f(\vec{p}_b) \tag{5.8}$$

was approximately constant for each pair of $[p_l, p_m]$.

This data reduction method has been coded in an IDL computer program [IDL]. Tiny artificial jumps in the autocorrelation function occur at the power-of-two boundaries introduced by the discrete multiple-tau method. These jumps are well below 10^{-3} in absolute height and therefore had no effect on the resulting fit of the relaxation process.

5.4 Results and Discussion

5.4.1 Reference Measurements

In order to characterize the instrumental setup and the behavior of the pure aerosil-gel, time correlation measurements were done using the reference sample described in Chapter 5.1.1. Two series of images were recorded at room temperature: one without the recirculating chiller connected to the sample and one with the chiller connected and operating, with the temperature set to approximately 22 °C at the sample. Figure 5.4 shows the measured autocorrelation data $g_2(\tau)$ for different values of q.

The *fluctuation* contrast Γ_{fl} in these measurements was very low: less than 1.2% in the case without the chiller and less than 4.4% in the case with the chiller operating. This may mean that either (a), there were fast dynamics present in the system of which only the tail of the relaxation was visible in these autocorrelation functions, or that (b), the sample was mostly static with only occasional fluctuations taking place. In order to distinguish between these two possibilities, a comparison of the measured *speckle* contrast, analyzed as described in Chapters 3 and 4, with the calculated values of Γ_{corr} calculated according to Chapter 1.2 is helpful.

Static analysis of the speckle patterns recorded with and without the chiller revealed that the measured speckle contrast in a single frame of the series was essentially the same as Γ_{corr} calculated according to Eqs. (1.25) and (3.6). Thus, the probability for the occurrence of strong fluctuations in the sample, that were too fast to fully detect them in this experiment, is significantly reduced. It is very reasonable to conclude that the experiment was mostly static with only occasional fluctuations taking place.

Figure 5.5 shows the sum of all the images in each of the two series. Speckles are clearly visible. In the series recorded without the chiller, the speckle contrast of the sum of images was the same

(a)

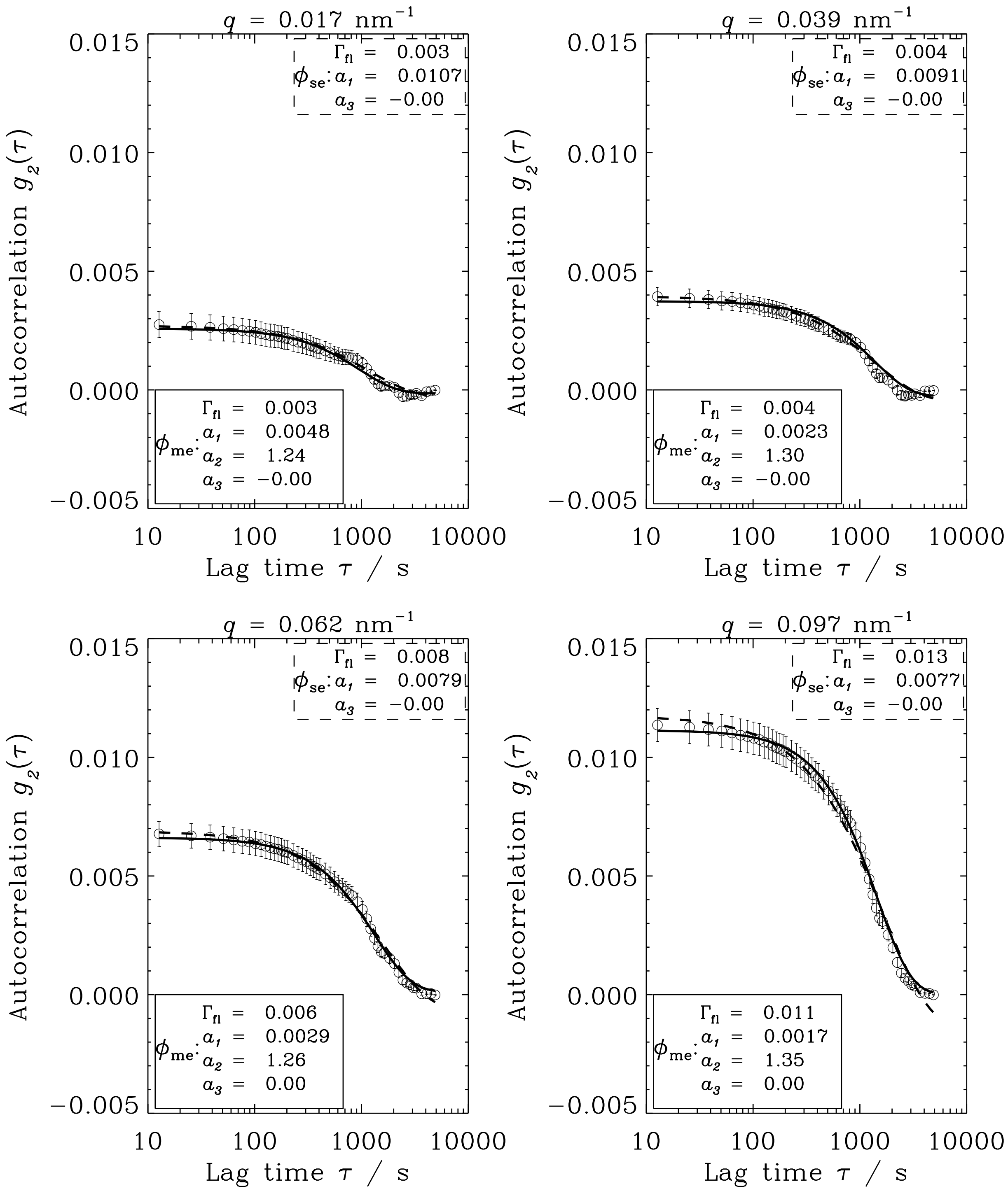

Figure 5.4: *(a) Time correlation data from the pure aerosil sample recorded without recirculating chiller. The dashed lines show single-exponential fits to the data (Eq.* (5.9)*), the solid lines represent fits of the modified-exponential function (Eq.* (5.10)*).*

(b)

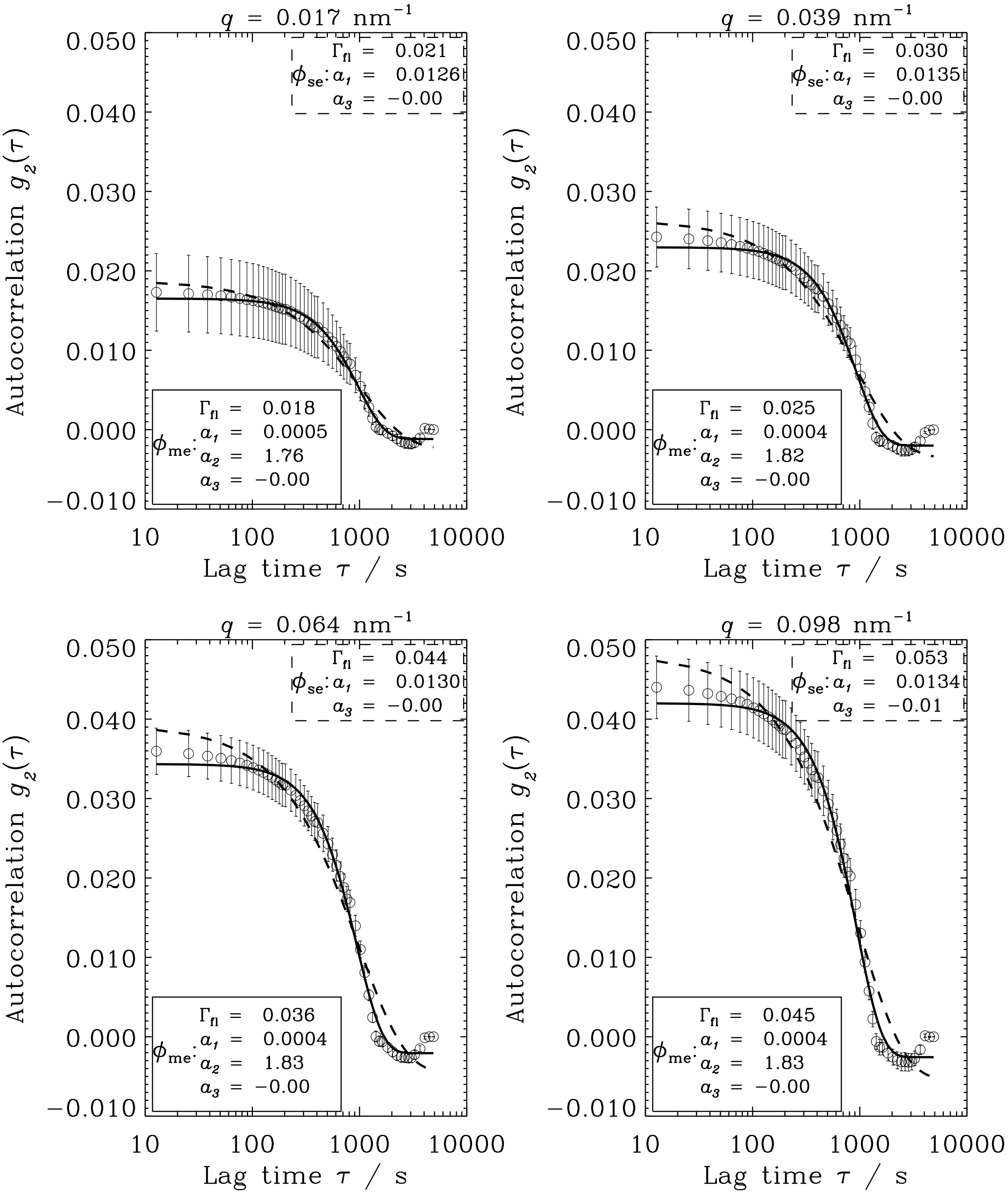

Figure 5.4: *(b) Time correlation data from the pure aerosil sample recorded with the recirculating chiller operating (~ 22 °C). The dashed lines show single-exponential fits to the data (Eq.* (5.9)*), the solid lines represent fits of the modified-exponential function (Eq.* (5.10)*).*

as the speckle contrast of a single image from this series. For a dynamic system with strong relaxations on time scales shorter than the longest lag time accessed in the experiment (here ~ 5200 s), such a sum of images should look like small-angle scattering data in an incoherent experiment, i.e., speckles should not be visible. The existence of such relaxations can thus be excluded. With the chiller operating, the speckle contrast of the sum of images was reduced by 25% compared to the measured speckle contrast in a single image of this series. In combination with the increase in fluctuation contrast $\Gamma_{\rm fl}$ in this series compared to the other reference series, this indicates the presence of fluctuations in the aerosil-gel introduced by the operation of the recirculating chiller.

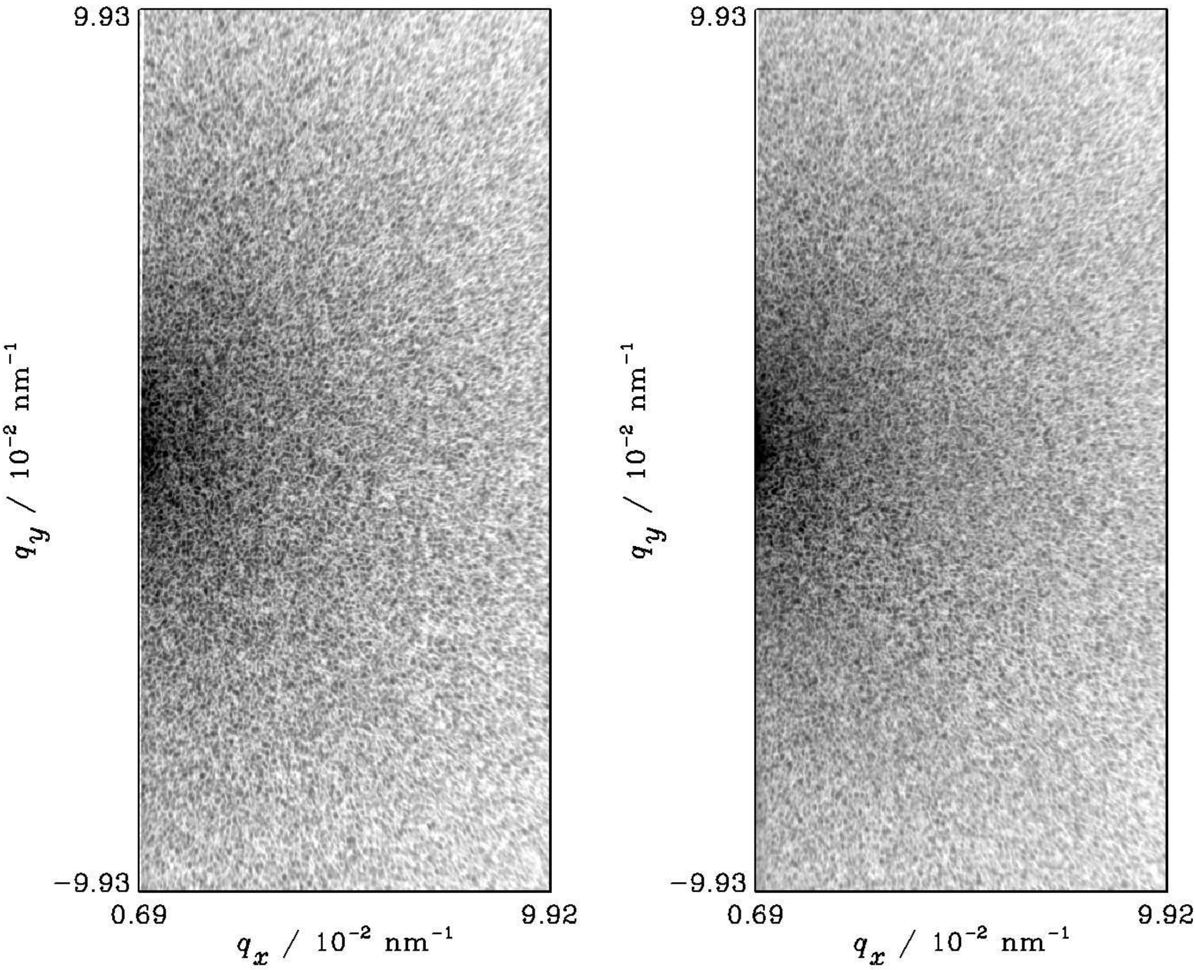

Figure 5.5: *Sum of* 400 *speckle patterns recorded with the pure aerosil sample without recirculating chiller (left) and with recirculating chiller operating (right).*

In both data sets, $g_2(\tau)$ was fit with two different versions of exponential functions: a single-exponential function $\phi_{\rm se}(\tau)$,

$$\phi_{\rm se}(\tau) = \Gamma_{\rm fl} \exp(-a_1\tau) + a_3 \quad , \tag{5.9}$$

chiller	χ^2_{se}	χ^2_{me}	a_2
off	4.9	4.7	1.2 ± 0.1
on	12	2.5	1.8 ± 0.1

Table 5.2: *Average fit quality and exponential parameter a_2 of the modified-exponential function. All values are averaged over q. χ^2_{se} and χ^2_{me} describe the sum of the squares of the residuals weighted with the estimated measurement error and the number of degrees of freedom, in the case of the fit with ϕ_{se} and ϕ_{me}, respectively.*

and a modified-exponential function $\phi_{\mathrm{me}}(\tau)$,

$$\phi_{\mathrm{me}}(\tau) = \Gamma_{\mathrm{fl}} \exp(-a_1 \tau^{a_2}) + a_3 \quad . \tag{5.10}$$

Note that Eq. (5.9) is a special case of Eq. (5.10) for $a_2 \equiv 1$. If a data set is fit best with $a_2 \neq 1$, there is more than one relaxation process present in the system. For parameters $a_2 \leq 1$ (i.e., the case of the Williams-Watts function), the overall relaxation process in the system can be modeled as a superposition of several single-exponential functions as described in Chapter 1.3. For values of a_2 larger than 1, the dynamics involve more complicated processes than single-exponential relaxation functions, as, e.g., quadratic-exponential (Gaussian) functions (see Table 1.1 for examples). A straight-forward interpretation of the nature of the relaxation processes in the system is then no longer possible. Thus, the value of a_2 is an indicator for the complexity of the fluctuations in the system.

Table 5.2 shows the q-averaged χ^2-values for both fit functions and the exponential parameter a_2. A χ^2 closer to 1 indicates a better (higher quality) fit. In the measurement without the recirculating chiller, the fit of the single-exponential funtion $\phi_{\mathrm{se}}(\tau)$ to the autocorrelation function $g_2(\tau)$ yielded good results (see dashed lines in Fig. 5.4 (a)). The obtained values for a_2 were just slightly larger than 1. For the data series recorded with the recirculating chiller operating, significantly better fit results were obtained using the modified-exponential function $\phi_{\mathrm{me}}(\tau)$ (see solid lines in Fig. 5.4 (b)). The fit resulted in values of $a_2 \approx 1.8$, independent of q. Thus, the observed relaxation process exhibits a high degree of complexity.

Figure 5.6 shows the q-dependence of the fluctuation contrast and the relaxation times retrieved from both fits. Here, the relaxation time $\tau_{0.5}$ is the lag time in which the temporal autocorrelation $g_2(\tau, q)$ assumes half of its zero-lag-time value:

$$\tau_{0.5} = \left[\frac{\ln(2)}{a_1}\right]^{\frac{1}{a_2}} \quad , \tag{5.11}$$

with $a_2 = 1$ in the case of the single-exponential function ϕ_{se}. The solid symbols in Fig. 5.6 represent the parameters obtained from the fit of ϕ_{me}. The open symbols show the results from the fit of ϕ_{se}. The lines plot the linear regression to the parameters. Linear regression values

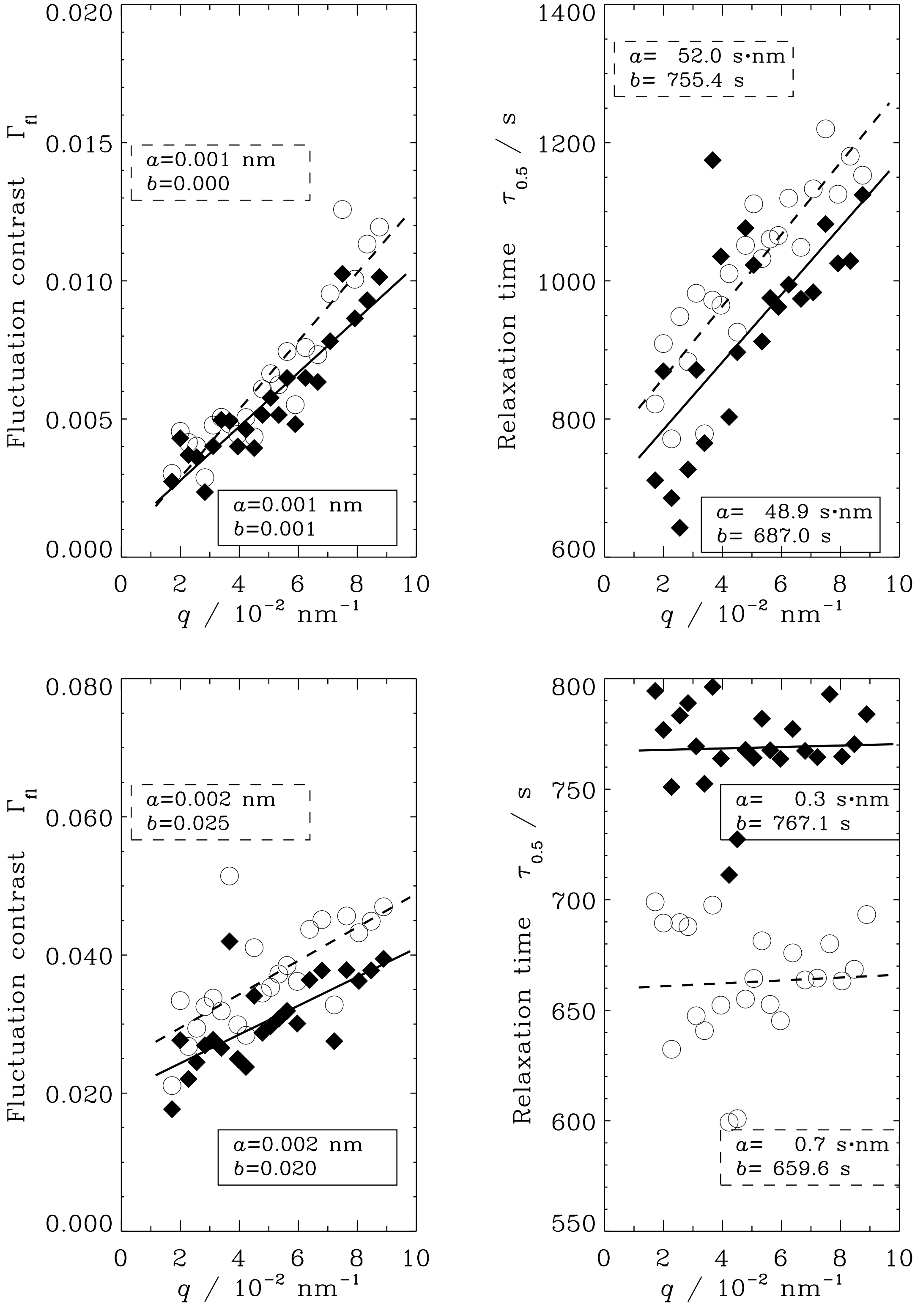

Figure 5.6: *q-dependence of fluctuation contrast (left) and relaxation time (right) for the reference measurements without chiller (top) and with chiller operating at room temperature (bottom). The solid and open symbols represent the results obtained from the fits of $\phi_{\rm me}$ and $\phi_{\rm se}$, respectively. The lines plot the linear regression $aq + b$ to these results.*

are given in the boxes in the figure. For both measurements, an increase in fluctuation contrast Γ_{fl} with increasing q could be seen, which indicates that fluctuations were more pronounced on smaller length scales than on larger length scales. The relaxation time increased linearly with q from ~ 700 s to ~ 1200 s in the measurement without the chiller. With the chiller operating, relaxation times scattered around a value of 660 s were found from the fit of ϕ_{se}, clearly underestimating the relaxation time as can be seen in Fig. 5.4 (bottom). The values resulting from the fit of ϕ_{me} in this case also scattered in q-space. The average value however was ~ 770 s, more closely fitting the measured behavior. These relaxation times again indicate that there were fluctuations or oscillations introduced by the recirculating chiller to which the aerosil sample responded in a complex way. The time correlation of these fluctuations decayed independent of q with a relaxation time of about 13 minutes. The q-dependence observed in the correlation data recorded without the chiller disappeared when the recirculating chiller was switched on. It was masked by the dynamics introduced by the chiller, affecting all length scales in the system equally. What is important to notice here, is the fact that the loosely bonded aerosil-gel was in fact a dynamic system by itself and did *wiggle* in the way of a forced spring system when activated. The aerosil can thus not only break and reform to anneal static stress. Here the external driving force was provided by the recirculating chiller.

Also seen in the autocorrelation data from the measurement without chiller are the above-mentioned jumps at the steps introduced by the quasi-logarithmic lag-time scale of the multiple-tau method. They do not have any physical significance.

For measurements of dynamics with this setup, it has to be concluded that observed relaxation times on the order of 750 s to 800 s cannot be separated from the fluctuations introduced by the chiller.

5.4.2 Dynamics of the Low-Density Aerosil-Gel Trapped in Octylcyanobiphenyl

After characterizing the dynamic behavior of the setup and the pure aerosil-gel by means of the reference sample, the dynamics of the aerosil-gel trapped in the 8CB liquid-crystal were probed. These properties are expected to be influenced by the liquid-crystalline matrix in which the gel is held. Therefore, measurements were done at the different temperatures shown in Table 5.1 in Chapter 5.2, corresponding to the different liquid-crystal phases in the dispersion. Remarkably, the sample did not show any signs of radiation damage in the measurements, even though being exposed to an average dose rate of approximately 10^5 Gy/s for 17 hours. The time correlation data $g_2(\tau, q)$ for the measurements discussed in this section are given in Appendix E.

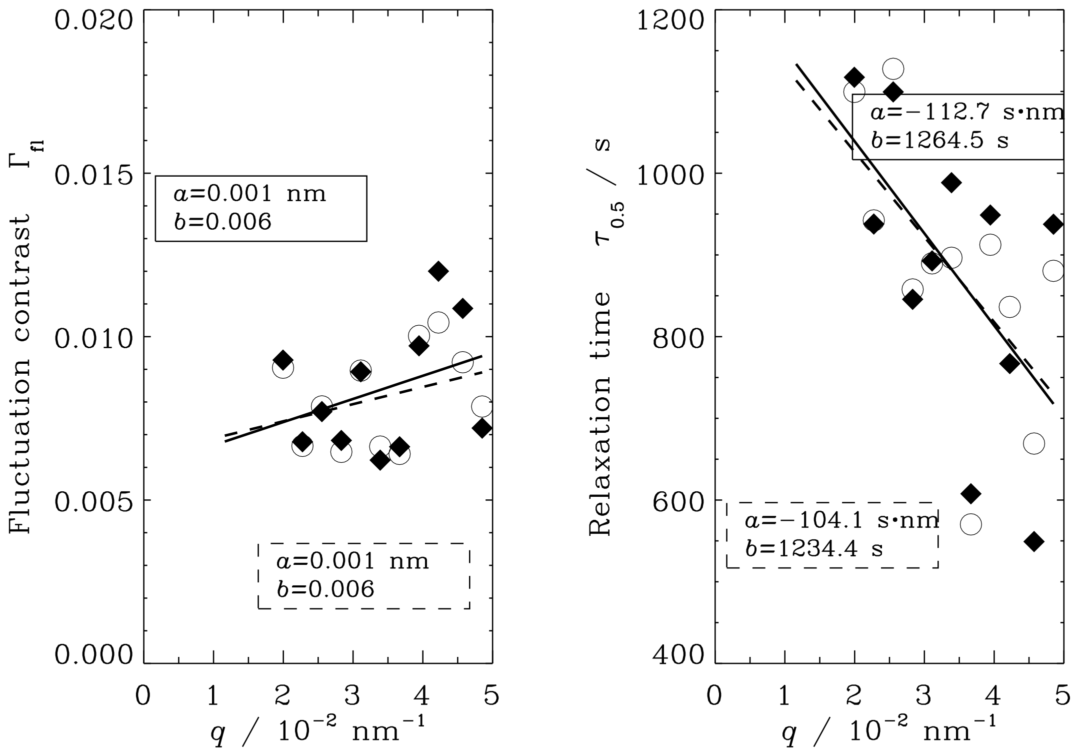

Figure 5.7: *q-dependence of fluctuation contrast (left) and relaxation time (right) at the crystalline-to-smectic-A$_{\rm d}$ phase transition ($17.2\,°$C). The solid and open symbols represent the parameters obtained from the fits of $\phi_{\rm me}$ and $\phi_{\rm se}$, respectively. The lines plot the linear regression $aq + b$ to these results.*

Crystalline-to-Smectic-A$_{\rm d}$ Phase Transition At the crystalline-to-smectic-A$_{\rm d}$ phase transition (17.2 °C), the fluctuation contrast $\Gamma_{\rm fl}$ was between 0.6% and 1.2% with no easily recognizable dependence on q. These values were smaller than the fluctuation contrast observed in the static reference sample with operating chiller. This might have had one of two origins, either (a) the system under investigation was even more static than the reference sample, i.e., responding less to the fluctuations introduced by the chiller, or (b) the relaxations in the system were faster than could be observed in this experiment. By comparing the speckle contrast in the images of this time series with the calculated $\Gamma_{\rm corr}$ according to Eqs. (1.25) and (3.6), it was found that the speckle contrast was reduced by about 32% compared to this calculation indicating the presence of relaxation processes in the system that were faster than the recording time for a single image ($\sim$ 30 s). The sum of all the images in this series still shows approximately the same speckle contrast as a single image from the series. It can be concluded that most of the relaxations in the system happened on time scales shorter than the recording time. Fitting $\phi_{\rm me}$ or $\phi_{\rm se}$ to the measured autocorrelation function did not yield large differences in the quality of the fit or in the derived parameters.[||] The resulting fluctuation contrast and relaxation times for both fit functions are shown in Fig. 5.7. The solid and open symbols represent the parameters obtained from the fit of $\phi_{\rm me}$ and $\phi_{\rm se}$, respectively. The lines indicate the linear regression to the parameters. Linear regression values are given in the boxes in the figure. The fits of $\phi_{\rm se}$ and $\phi_{\rm me}$ to the autocorrelation data yield very similar values for the relaxation times. The parameter a_2 in the fit of the modified-exponential function had values of ~ 1.0, indicating that the measured relaxation consisted of essentially one single-exponential relaxation. The relaxation time $\tau_{0.5}$ as defined above (Eq. (5.11)) decreased for both fits from ~ 1150 s for low q to ~ 700 s for high q. This means that the dynamics on smaller length scales relaxed faster than those on larger length scales. As the aerosil at this temperature is likely to be surrounded by solid crystals of 8CB (at least partially), this behavior can be imagined as aerosil-'balls' rattling in a crystalline cage. The relaxation time for thermal fluctuations, such as Brownian motion, particle diffusion, etc., is predicted to be proportional to $1/q^2$ [PT85, GP95]. Verifying this dependence with the data presented here is difficult. However, the observed decrease in relaxation time with increasing q is consistent with this prediction. Due to the dynamics introduced by the chiller, the observed relaxation times for $0.04\ \mathrm{nm}^{-1} \lesssim q \lesssim 0.045\ \mathrm{nm}^{-1}$ may be caused externally since they coincide with the time scales observed with the reference sample.

Smectic-A$_{\rm d}$ Phase The properties found in the smectic-A$_{\rm d}$ phase change with temperature. At 21.4 °C, the dynamic behavior is still similar to that at 17.2 °C. Figure 5.8 (top) shows the resulting fluctuation contrast and relaxation times. In spite of the lower number of free parameters for $\phi_{\rm se}$, the quality of the fit of $\phi_{\rm se}$ was significantly better than that of $\phi_{\rm me}$ (see Table 5.3), which very likely indicates a shallow minimum of the fit parameter space for this data set. Still, the two fits yielded comparable results with a_2 very close to 1.0 . The fluctuation contrast was below 1% and slightly decreased with increasing q. Thus, fluctuations at large length scales in the sample (small q) became more pronounced than fluctuations on small length scales, which can be interpreted as an indication for macroscopic melting of the system. In general, these values, in connection with a $\sim$ 30% reduction in the speckle contrast compared to the calculation of $\Gamma_{\rm corr}$, indicate the presence of fast-decaying correlation processes that were not probed by this experiment. Again, the sum of all images in this series yielded a speckle contrast close to that of a single image from this series; thus most of the relaxation processes in the system were faster than the time range accessible in the measurements. The relaxation times derived from the fits of Eqs. (5.9) and (5.10) both decreased with increasing q. Thus, similar to the situation at 17.2 °C, dynamics at smaller length scales were dampened more strongly than those at larger length scales. However, compared to the situation at 17.2 °C, the relaxation times were shorter. Values of $\sim$ 950 s for low q and $\sim$ 400 s for high q were derived from the fits. Again, it is

[||] Table 5.3 on page 83 shows the average values for the quality of fit and the exponent a_2 for all temperatures investigated.

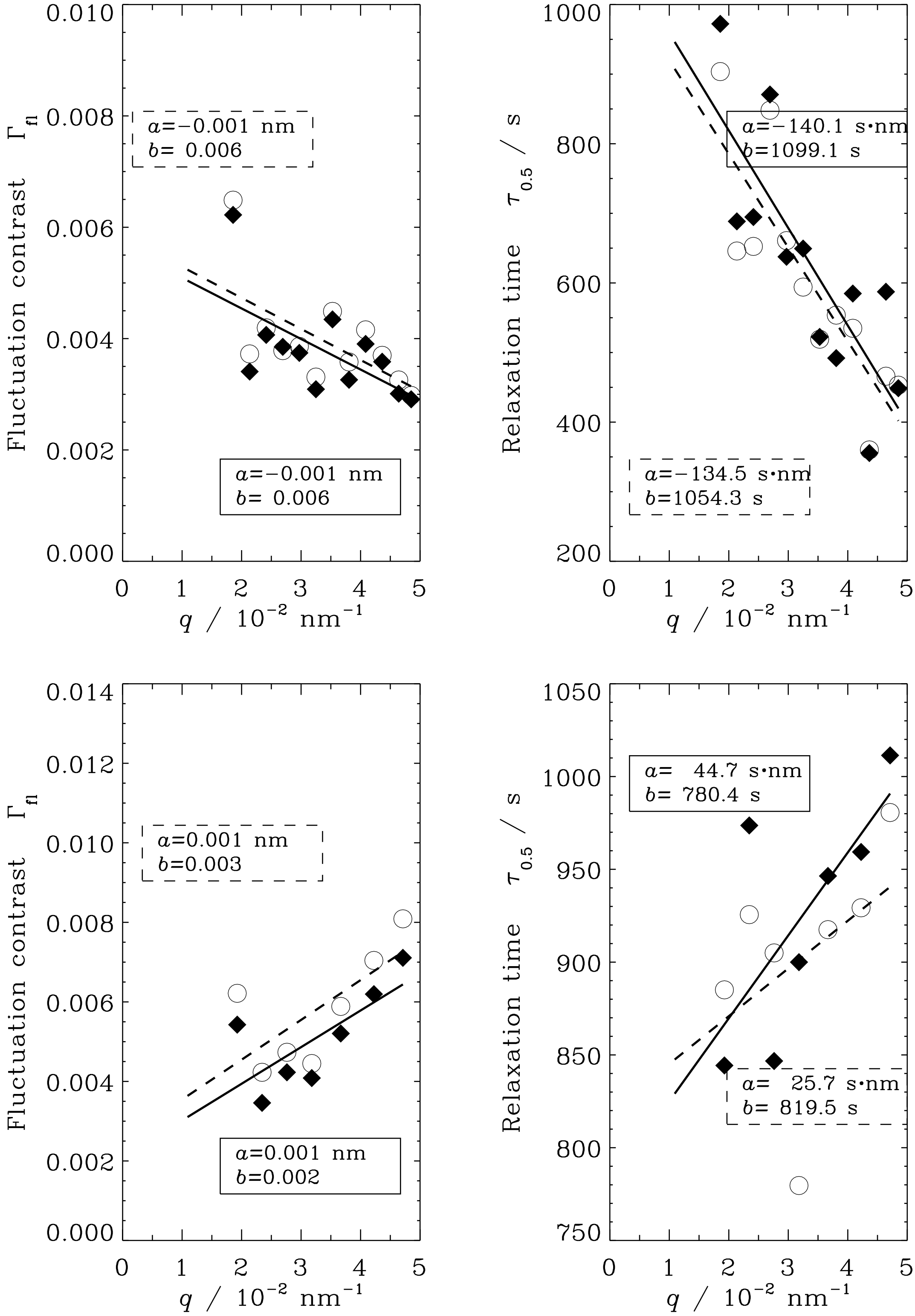

Figure 5.8: *q-dependence of fluctuation contrast (left) and relaxation time (right) in the smectic-A_d phase at $21.4\ °C$ (top) and at $26.6\ °C$ (bottom). The solid and open symbols represent the parameters obtained from the fits of ϕ_{me} and ϕ_{se}, respectively. The lines plot the linear regression $aq + b$ to these results.*

difficult to verify a $1/q^2$ dependence with this data, but the observed decrease in relaxation time with increasing q is consistent with thermal fluctuations. The low-q range 0.019 nm$^{-1} \lesssim q \lesssim 0.025$ nm^{-1} may also be affected by the dynamics introduced by the chiller.

In the smectic-A$_{\mathrm{d}}$ phase at 26.6 °C, the relaxation processes tended to become more complex, which is seen in the increase of a_2 to 1.3 and the better quality of fit of ϕ_{me} compared to ϕ_{se} (see Table 5.3). Qualitatively, the results were different from the results obtained at 17.2 °C and 21.4 °C in the way that relaxation times tended to *increase* with q rather than decrease. The fluctuation contrast and relaxation time can be seen in Fig. 5.8 (bottom). Γ_{fl} was again very low, but it increased from around 0.4% for low q to around 0.8% for high q, which points towards increased fluctuations on smaller length scales in the system.** The speckle contrast in a single frame was still reduced by about 30% from the value of Γ_{corr} calculated according to Eqs. (1.25) and (3.6). The relaxation times derived from the fits to the data have values of ~ 850 s to ~ 1000 s. These values are larger than those found in the reference experiment with operating chiller. The observed relaxations are slower than those introduced by the chiller. This means that the aerosil-gel takes energy away from the dispersion, which prolongs the relaxations of the aerosil dynamics. Additional faster relaxations are very likely present as well but could not be quantified using this data.

Smectic-A$_{\mathrm{d}}$-to-Nematic Phase Transition At the smectic-A$_{\mathrm{d}}$-to-nematic phase transition (32.0 °C), the fluctuation contrast was significantly higher than that of the previous data series. It showed values between 2.5% and 4% (Fig. 5.9). In addition, the speckle contrast in this series was higher. It was only reduced by 23% compared to the calculated Γ_{corr}. This indicates that there were still faster relaxation processes than could be detected, but their characteristic time was not that much shorter than the integration time used in this series. Clearly, much slower relaxations could also be seen in this measurement. At this temperature, the modified-exponential function yielded distinctly better fit results than the single-exponential function (see Table 5.3), resulting in parameters a_2 that were around 1.7, significantly larger than 1.0. This indicates the high complexity of the observed relaxation process. The resulting relaxation times were scattered around 2200 s (Fig. 5.9). The speckle contrast evaluated in the sum of all images in this series was reduced by 63% compared to that of a single image in this series. These results show clearly that the onset of the expected slowing down of the dynamics at the smectic-A$_{\mathrm{d}}$-to-nematic phase transition in a liquid-crystal [BCS95, Chu85, GK80] was reflected in the dynamics of the aerosil-gel embedded in the liquid-crystalline matrix and that the time scales of this slowing down were clearly accessible in this experiment. Fluctuations were more pronounced at high q-values than at low q-values. The relaxation times observed at this temperature were clearly not masked by the dynamics of the chiller, as they were about three times as large. The fluctuations

**Even though the Landau-Peierls instability [GP95] does predict a logarithmic divergence of the mean fluctuations with the size of a smectic system, a connection to this effect cannot be established at this point.

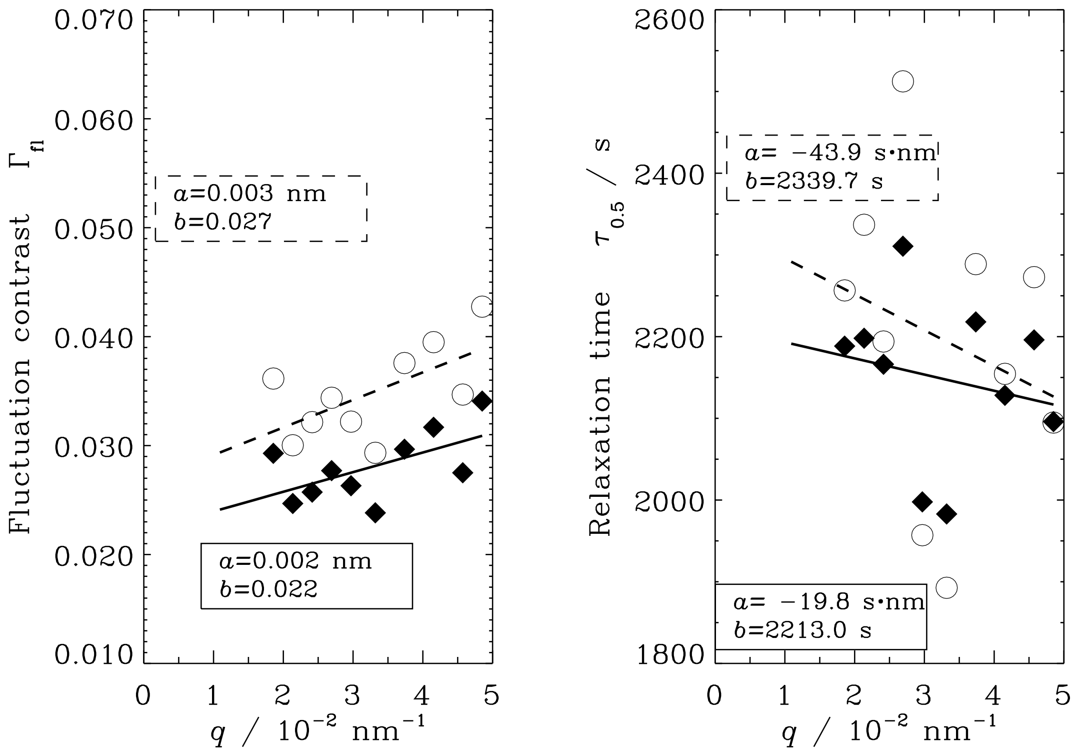

Figure 5.9: *q-dependence of fluctuation contrast (left) and relaxation time (right) for the smectic-A_d-to-nematic phase transition ($32.0\ ^\circ C$). The solid and open symbols represent the parameters obtained from the fits of ϕ_{me} and ϕ_{se}, respectively. The lines plot the linear regression $aq + b$ to these results.*

introduced by the chiller may have stimulated part of the observed relaxation process. However, the observed slow relaxation suggests that the aerosil-gel was activated not only by the chiller. An additional driving force must have come from the 8CB.

A slowing down of dynamics in a system of 8CB trapped in an aero*gel* of density 0.36 g/cm^3 was reported earlier by Bellini *et al.* [BCS95]. In those experiments, however, the ordering of the liquid-crystal within the pores of the rather high-density aerogel was studied, which would be equivalent to a stiff aerosil-gel, and the observed relaxation times were $\lesssim 1.0$ s. Wu *et al.* [WGLX92] reported complex slow dynamics of 8CB trapped in $\rho = 0.289$ g(sil)/cm^3(total) aero*gel*, approaching the smectic-A_d-to-nematic phase transition from above. The observed relaxation times were on the order of seconds or longer. In contrast to these two experiments, here the dynamics of the low-density soft aerosil-gel inside the liquid-crystal were of interest. Similar to the experiments presented here, previous work found that the measured autocorrelation function near the phase transition temperature could not be described by either a single-exponential or the Williams-Watts function ($a_2 \leq 1.0$). Bellini *et al.* attributed the observed behavior to thermal motion of nematic defects in the smectic phase within the spatial limits defined by the aerogel.

Wu *et al.* stress the similarity to a random-field behavior, without further theoretical description. In the experiment presented here, the situation is different, because the soft aerosil-gel does not provide rigid boundaries for the liquid-crystal, and the measured relaxation times were several orders of magnitude larger than those found with the aerogel. However, nematic defects building in the smectic-A_d matrix could clearly affect the ordering of the aerosil-gel, which can easily break and reorder its network. Such a *static annealing* of strains should influence the aerosil-gel's dynamics in the present case as well, is however most likely occurring on subsecond time scales.

Other experiments by Iannacchione *et al.* [IGMR98] indicated that the presence of the low-density aerosil-gel forces the system to approach the $3d$-XY universality class. Iannacchione *et al.* explained this behavior with *static* annealing as well. However, the *dynamics* of the gel observed here can be understood as the underlying interaction process for this cross-over behavior: The measurements indicate that the aerosil-gel, coupling to the director of 8CB, mimics the director fluctuations in the liquid-crystal and, at the same time, takes free energy away from the liquid-crystal, thus relaxing more slowly. The mechanism can be thought of as a system of coupled springs, where part of the potential energy of the liquid-crystal is lost to the gel network. This dampening of the fluctuations in the liquid-crystal entails the cross over to a $3d$-XY universality class. As a result, large relaxation times were observed for the aerosil-gel with relaxation processes that were of higher order than single-exponential ($a_2 \approx 1.7$).

Usually, the influence of the *director* fluctuations on the behavior at the smectic-A-to-nematic phase transition is not paid much attention [GP95]. No theory explaining the coupling of the director fluctuations to the complex smectic order parameter is available to date even though the observation of in-plane director fluctuations in smectic 8CB was already reported [MMCLM93]. The present data suggest the effect of this coupling should be further investigated. The director fluctuations seem to have a fundamental effect on the universality of the system.

Nematic Phase In the nematic phase (35.0 °C), the fluctuation contrast was as low as at temperatures below 30 °C, with values around 0.8%. An increase with q was seen similar to that observed in the smectic-A_d phase at 26.6 °C and at the smectic-A_d-to-nematic phase transition. Again, fluctuations on short length scales were more pronounced than at larger length scales. The observed relaxation times were higher than those related to the operating chiller, ranging from ~ 1000 s for low q to ~ 1250 s for high q, though not as high as at the smectic-A_d-to-nematic phase transition. The parameter a_2 in the fit of ϕ_{me} decreased from the value found at 32.0 °C but was still significantly higher than 1.0 (see Table 5.3). The temperature of 35.0 °C was ~ 2 °C above the expected smectic-A_d-to-nematic phase transition at 33 °C, whereas the measurement at 32.0 °C was done at ~ 1 °C below it. In both cases, a slowing down of relaxations in the system was observed. These data suggest that within a wide temperature range of up to ± 2 °C around the smectic-A_d-to-nematic phase transition, slowing down of relaxations, i.e., the

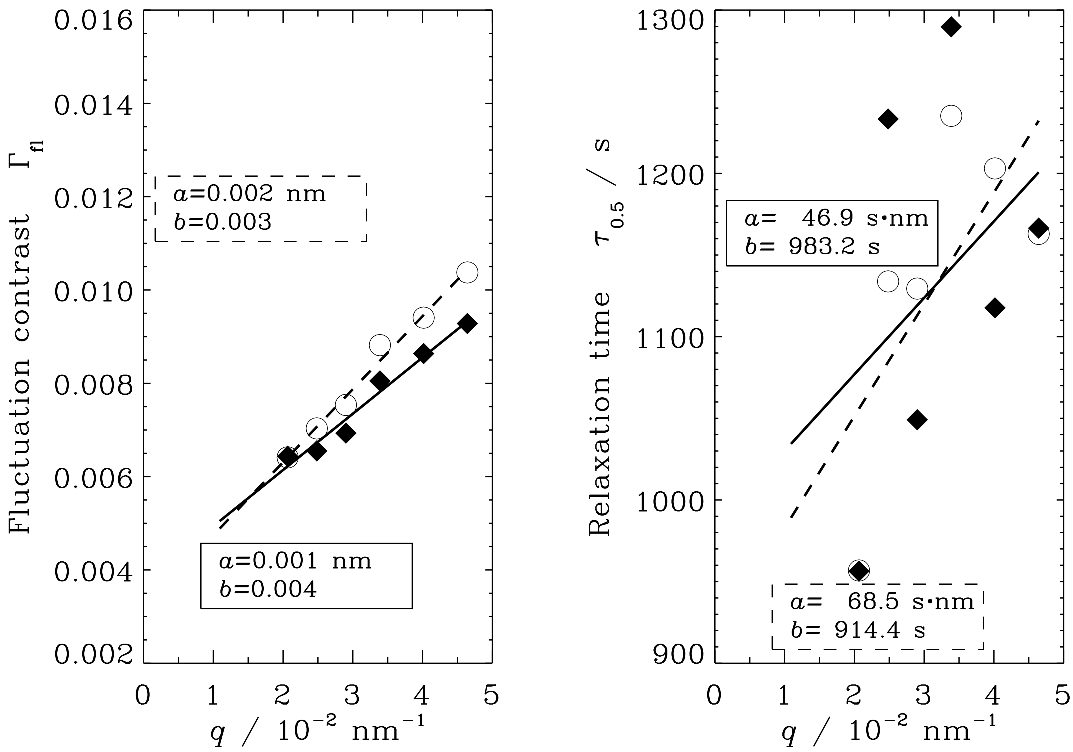

Figure 5.10: *q-dependence of fluctuation contrast (left) and relaxation time (right) for the nematic phase (35.0 °C). The solid and open symbols represent the parameters obtained from the fits of ϕ_{me} and ϕ_{se}, respectively. The lines plot the linear regression $aq + b$ to these results.*

transfer of free energy from the liquid-crystal to the aerosil-gel, can be observed. With increasing temperature difference from the phase transition however, the strength of the fluctuations, i.e., the fraction of scattering centers participating in the dynamics, decreased, which reduced the fluctuation contrast Γ_{fl}.

Nematic-to-Isotropic Phase Transition At the nematic-to-isotropic phase transition (38.6 °C), the fluctuation contrast exhibited values around 2%. Fluctuations at this temperature were more pronounced than in the crystalline, smectic-A_{d}, or nematic phases of the liquid-crystal but less pronounced than at the smectic-A_{d}-to-nematic phase transition. The parameter a_2 had values just below 1.0, indicating a narrow distribution of superimposed single-exponential relaxations. Besides one value observed at low q, the relaxation times were scattered around 690 s (Fig. 5.11). A $1/q^2$-dependence of the relaxation time could not be observed, indicating that the fluctuations in the system were not exclusively caused by simple thermal processes. However, the observed relaxation times were very close to the time structure imposed by the recirculating chiller, which may thus have dominated the data.

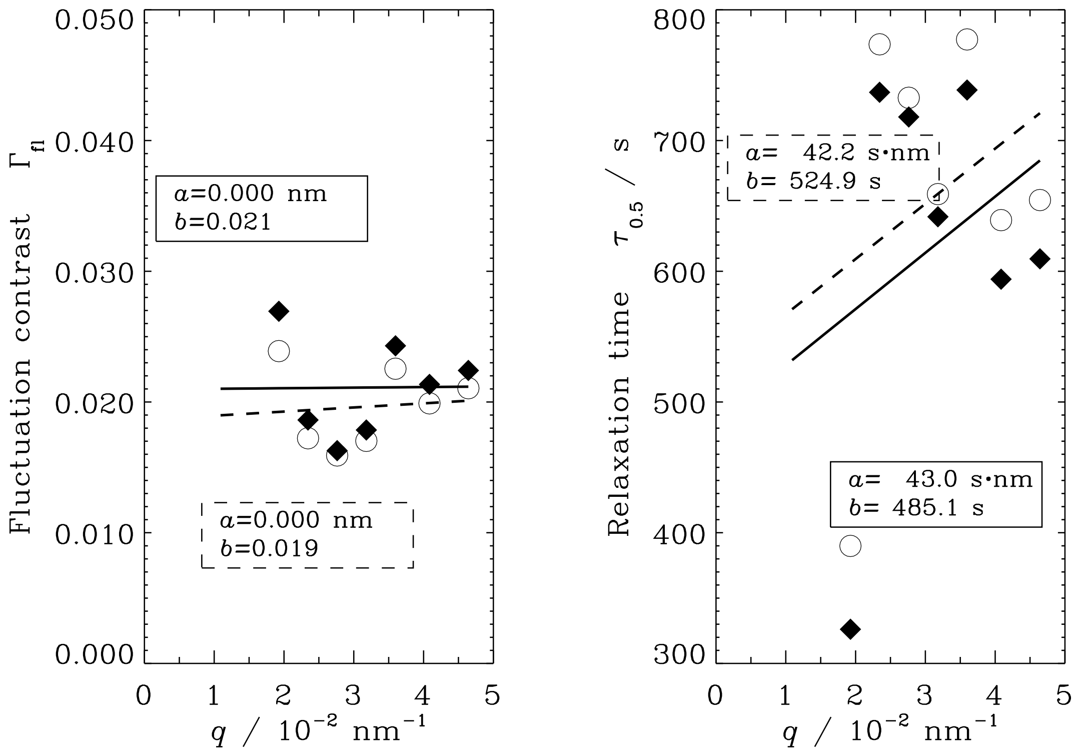

Figure 5.11: *q-dependence of fluctuation contrast (left) and relaxation time (right) for the nematic-to-isotropic phase transition (38.6 °C). The solid and open symbols represent the parameters obtained from the fits of ϕ_{me} and ϕ_{se}, respectively. The lines plot the linear regression $aq + b$ to these results.*

Isotropic Phase The measurement at the temperature of the isotropic phase (42.5 °C) again shows low fluctuation contrast between 0.7% for low q and 1.5% for high q (see Fig. 5.12) showing stronger fluctuations on smaller length scales. The relaxation times were increased and rather q-independent with values around ~ 1000 s. These values are larger than those affected by the chiller. The fit of the modified-exponential function to the data yielded significantly better results (see Table 5.3), and the parameter a_2 resulted in values significantly above 1.0. This again indicates the presence of complicated relaxation processes.

Temperature Dependence Figure 5.13 shows the average fluctuation contrast Γ_{fl}, the relaxation time $\tau_{0.5}$, and the exponential parameter a_2 of the 8CB – aerosil system derived from the fits at various temperatures. The open and solid symbols represent the parameters derived from the fits of ϕ_{se} and ϕ_{me}, respectively. The values shown are averages over q. The lines in the plot simply connect the average results, and the dashed region indicates the range of relaxation times affected by the operation of the recirculating chiller. The temperature dependence showed

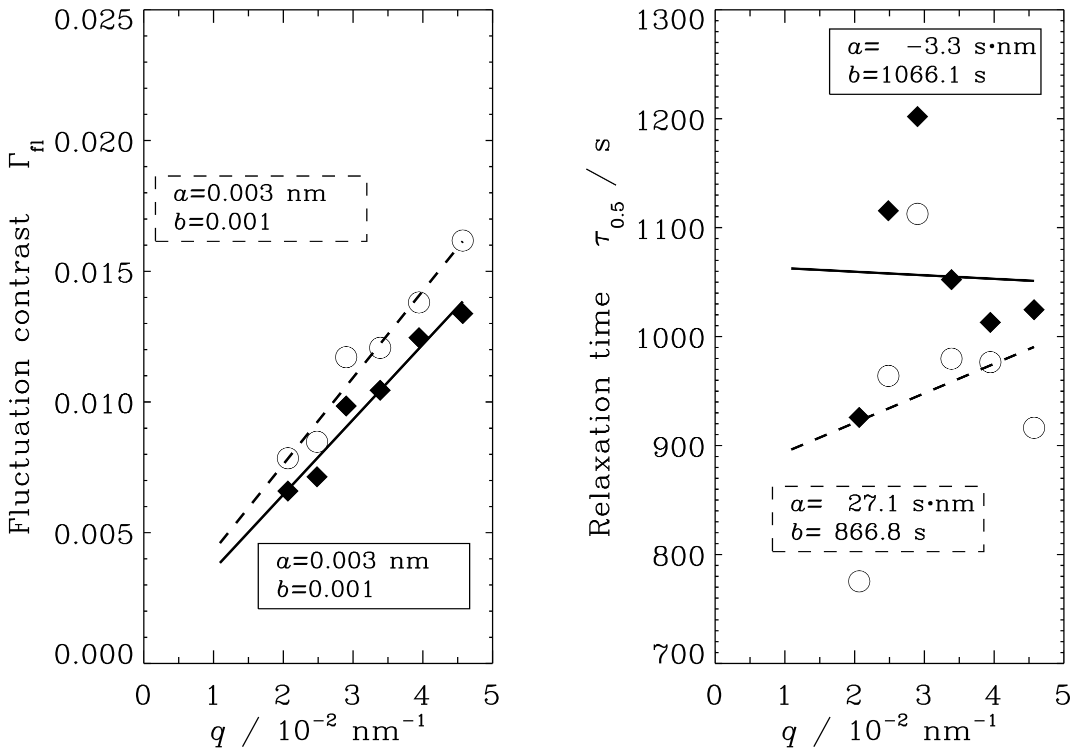

Figure 5.12: *q-dependence of fluctuation contrast (left) and relaxation time (right) for the isotropic phase* ($42.5\ ^\circ$*C). The solid and open symbols represent the parameters obtained from the fits of* ϕ_{me} *and* ϕ_{se}*, respectively. The lines plot the linear regression* $aq + b$ *to these results.*

very similar behavior for both fits. The fit of ϕ_{se} to the data systematically yielded longer relaxation times than that of the modified-exponential function. For the measurements at 26.6 °C, 32.0 °C and 42.5 °C, the fit of ϕ_{me} was significantly better resulting from the use of the extra parameter a_2, which assumed values very different from 1.0. For all the other temperatures investigated with this sample, the fit quality was very similar for both functions (see Table 5.3).

A significant slowing down was observed for the relaxation times measured in a wide temperature range around the smectic-A$_{\mathrm{d}}$-to-nematic phase transition temperature. At the same transition, the fluctuation contrast, being a measure for the fraction of the system participating in the dynamics on the probed time scales, was increased as well, even though the peak was not as wide as that observed for the relaxation times. The temperature dependence of the fit parameter a_2 clearly showed the increase in complexity of the relaxation processes observed at the smectic-A$_{\mathrm{d}}$-to-nematic phase transition. The affected temperature range seemed to span at least a range of ± 2 °C around the phase transition temperature, being consistent with the development of a very complex corporative relaxation mode at the phase transition. More measurements on a finer

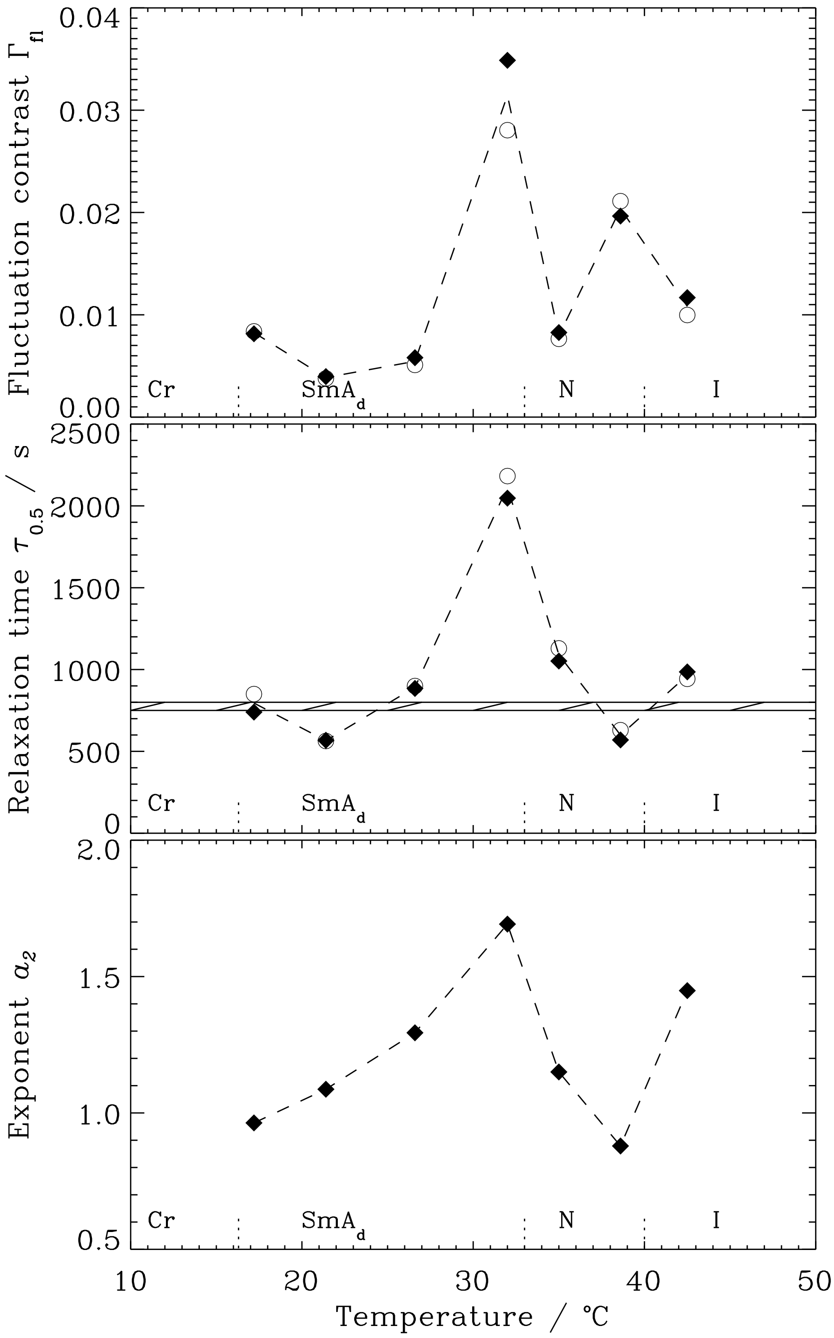

Figure 5.13: *Temperature dependence of the fluctuation contrast (top), relaxation time (center), and exponential parameter a_2 (bottom). The solid and open symbols represent the parameters obtained from the fits of $\phi_{\rm me}$ and $\phi_{\rm se}$, respectively. The lines connect the averages of both sets of parameters as guides to the eye. The dashed region (center) indicates the time range affected by the operation of the chiller. Vertical dotted lines show the expected phase transition temperatures of the system.*

phase	T / °C	χ^2_{se}	χ^2_{me}	a_2
Cr $\leftrightarrow$ SmA$_\mathrm{d}$	17.2	4.4	4.5	1.0 ± 0.1
SmA$_\mathrm{d}$	21.4	15	16	1.1 ± 0.1
SmA$_\mathrm{d}$	26.6	5.4	3.8	1.3 ± 0.1
SmA$_\mathrm{d}$ $\leftrightarrow$ N	32.0	5.0	0.7	1.7 ± 0.1
N	35.0	3.9	3.3	1.2 ± 0.1
N $\leftrightarrow$ I	38.6	2.1	1.7	0.9 ± 0.1
I	42.5	5.1	1.2	1.4 ± 0.1

Table 5.3: *Average fit quality and exponential parameter a_2 of the modified-exponential function. All values are averaged over q. χ^2_{se} and χ^2_{me} describe the sum of the squares of the residuals weighted with the estimated measurement error and the number of degrees of freedom, in the case of the fit with ϕ_{se} and ϕ_{me}, respectively.*

temperature grid are necessary to evaluate the exact behavior.

5.5 Summary

The feasibility of x-ray intensity fluctuation spectroscopy at an x-ray energy of 1830 eV has been demonstrated on a pure self-supporting aerosil-gel and a low-density dispersion of silica aerosil in an octylcyanobiphenyl liquid-crystal. The temporal autocorrelation curves were fit by a single-exponential function and a modified-exponential function that, as an extension of the Williams-Watts function found in the literature, was not restricted to exponential parameters less than 1.0. The value of the exponential parameter can be used to gauge the complexity of the observed relaxation processes.

The pure self-supporting thixotropic aerosil-gel exhibited dynamic relaxations. When connected to the recirculating chiller used for temperature control of the dispersion sample, the pure aerosil-gel sample was found to show a complex response to the vibrations introduced by the chiller. The measurements presented here are the first to demonstrate the aerosil's capability of dynamically responding to an activating force.

Then, the dynamics of the gel trapped in the structure of the liquid-crystal were probed. This organic dispersion did not show any signs of radiation damage. Different dynamic behavior was detected, depending on the phase of the dispersion. At the smectic-A$_\mathrm{d}$-to-nematic phase transition, the dynamics in the gel slowed down. A large temperature range around the phase transition temperature was affected (at least ± 2 °C). The exponential parameter in the modified-exponential function yielded values significantly larger than 1.0 within this temperature region around the transition. This indicates that there were complex corporative modes of relaxation contributing to the observed dynamics. The average relaxation times were scattered around a value of 2200 s close to the transition temperature and decreased to around 600 s deep in the smectic-A_d phase, as well as towards the nematic-to-isotropic phase transition. In the isotropic phase of the dispersion, the relaxation times of the aerosil increased again to values around 1000 s. This study is the first to probe directly the dynamics of the aerosil in an 8CB – aerosil dispersion by any method including XIFS. The enormous slowing down of the dynamics at the second-order smectic-A_d-to-nematic phase transition indicates that the aerosil, most likely coupling to the director of the 8CB molecules, not only mimics an expected slowing-down of thermal fluctuations at such a phase transition but also takes away energy from the 8CB dynamics, which results in prolonged relaxation times of the gel. The data suggest that by this the gel network of the aerosil provides a random dampening field for the director fluctuations at this phase transition. One consequence of this could be the known cross-over behavior of low-density 8CB – aerosil systems to the $3d$-XY universality class of critical phenomena observed elsewhere [IGMR98]. In this class, order parameter fluctuations are suppressed. This cross-over behavior was previously not understood.

Chapter 6

Concluding Remarks and Future Directions

Coherent x-rays allow for a new approach to the investigation of materials, as well as of the fundamental properties of light. The advent of third-generation synchrotron sources opened this field of physics. The common technique of investigating dynamics of disordered materials by spectroscopy of the intensity fluctuations after illumination with coherent light, originally developed in the visible-light regime using lasers, is experiencing growing interest in the x-ray regime. Since the first demonstration of x-ray speckle in 1991 using synchrotron radiation [SMG$^+$91], an ever increasing number of x-ray experiments involving speckle have been reported. Mostly, high x-ray energies above 5 keV are used for these experiments. In the soft x-ray energy region below 1 keV in energy, speckle techniques have been demonstrated and applied. But up to now, x-ray energies between 1 keV and 4 keV were underrepresented among the speckle measurements, even though this energy region has advantages, such as increased spatial coherence lengths compared to higher energy x-rays and better penetration power compared to lower energies. In addition, the absorption edges of important elements for biology and industry, such as Ca, P, S, Si, Al, and the rare earths, just to name a few, can be found in this energy region.

Commonly, pinhole setups are used to select the desired coherent fraction of the beam. However, for technical reasons, beam diameters achievable with pinholes find their lower limit at the level of several micrometers. Achieving smaller beam diameters with pinholes is difficult and may be wasteful of coherent flux. A focusing setup could produce much smaller beam diameters and significantly increase the flux density on the sample. The excellent beam coherence properties available at x-ray undulator beamlines allow the x-ray beam to be focused to submicrometer-sized spots using state-of-the-art Fresnel zone plates. To compare the relative advantages of pinholes and zone plates, the two types of experimental setups were tested in a transmission geometry.

It was found that the divergence introduced by the zone plate does not affect the speckle contrast, size, or distribution in reciprocal space. The observed speckle patterns show the same characteristics as those observed in a pinhole setup with a pinhole size comparable to the beam size on the sample produced by the zone plate. Due to conservation of phase space, the degree of coherence across the focal spot of a zone plate is the same as that of the radiation incident on the full aperture of the zone plate. As the zone plate diameter is usually larger than that of the pinholes used in a pinhole setup, the radiation used in the experiment may have less spatial coherence. Because the speckle contrast is proportional to the square of the spatial degree of coherence, the speckle contrast achieved with the zone plate setup may be lower than that with the pinhole setup. In addition, for good focusing, a degree of monochromaticity $k/\Delta k$ of approximately the number of zones of the zone plate is required [Mic86]. This requirement may exceed the monochromaticity required for good speckle contrast in the pinhole setup. On the other hand, the pinhole setup is of advantage when high resolution in reciprocal space is needed and sufficient coherent flux is available. A q-resolution of better than $\sim 10^{-2}$ nm^{-1} was achieved with a 5 μm pinhole. For high real-space resolution or in the case of low count rates, a zone plate setup yields excellent results. The focusing by the zone plate down to submicrometer-sized beam diameters allows targeting of small sample areas. This can be useful if reduction of the sensitivity of the experiment to correlation length scales larger than the chosen beam size is desired, as, e.g., in experiments that investigate structures in single domains. For a systematic sample investigation, it is therefore advisable to start with a pinhole setup to gain spatially averaged information and a clear picture of the sample properties in reciprocal space, before the resolution in real space is improved by means of a zone plate setup.

Up to now, no investigation of the influence of x-ray absorption edges on the speckle contrast has been reported. Such an effect was studied in this thesis by measuring speckle data as a function of energy across the L_{III} $(2p^{3/2})$ absorption edge of a powdered Zn sample (1021.8 eV). It was found that the speckle contrast decreases at the absorption edge as the energy is increased. This was explained by modeling the results with a normalized two-dimensional spectral convolution of the mutual amplitude correlation function of the sample illumination with the product of the beamline spectral response function and the average scattered intensity at a given wavelength. However, the oft-made simplification found in the standard literature, that the average scattered intensity is mostly independent of the wave number, had to be dropped because it neglects anomalous scattering. The contrast was found to be strongly influenced by the imaginary part β of the complex index of refraction $n = 1 - \delta - i\beta$ of the sample. Good fits to the data were achieved using numerical computer code running on a cluster of 4 parallel-processing workstations connected via a network. Explanations for the observed q-dependence and energy resolution dependence of the fit parameters were given.

In order to understand the qualitative behavior of the findings, a comparison with Young's double-slit experiment was helpful. In Young's double-slit experiment, the fringe visibility decreases with increasing difference in transmission through the two slits. In the speckle experiment, the distribution of the transmitted intensity across the randomly absorbing sample increases its variance with an increase in β. This caused the speckle contrast to decrease in a similar way. The accuracy of the fits, especially close to the absorption edge, relies on the accuracy with which the index of refraction is known. Close to the absorption edge, the tabulated values for n generally are not very reliable. This explains why finer structural details in the speckle contrast are not described by the fits, whereas the overall behavior of the data is explained. Detailed information about the imaginary part of the index of refraction may be gained by more careful measurement and analysis of speckle contrast at absorption edges. However, such an analysis requires a very high computational effort. There already exist more practical ways to do this. A careful analysis of the variation of speckle locations in the energy series may give insight into the behavior of the real part of the index of refraction across the absorption edge. Such an investigation, however, was beyond the scope of this thesis.

Recently, absorption edges were used in resonant magnetic speckle experiments, [YLL$^+$99, PVM$^+$00] to enhance the magnetic scattering cross section. A detailed analysis of the edge effects on the speckle contrast in these cases could help in optimizing the experiments and understanding the observed scattering strengths. The speckle contrast effect demonstrated in this thesis will be of use when, e.g., samples containing multiple elements are investigated with the aim of determining element-specific structural information. The variation in speckle contrast at a sample-specific absorption edge makes it possible to enhance or suppress speckle originating from one or more of the constituent elements.

After exploring the special features accessible in the x-ray energy region of 1 to 4 keV, this knowledge was employed in experiments that probed the dynamics of a randomly disordered sample. The system of interest was a dispersion of silica aerosil in a liquid-crystal. The liquid-crystal used was octylcyanobiphenyl (8CB), a system that exhibits a crystalline phase, a smectic-A$_\mathrm{d}$ phase and a nematic phase between 15 °C and 40 °C. This system is particularly interesting because disorder is introduced in a controlled way, tunable by the density of the aerosil, forming a thixotropic gel. Prior to this thesis work, questions have been raised about the influence of the aerosil on the cross-over behavior to $3d$-XY universality observed at the smectic-A$_\mathrm{d}$-to-nematic phase transition of the dispersion as a function of aerosil density [IGMR98]. In order to address this question, time series of speckle images from a low-aerosil-density dispersion sample were recorded at different temperatures using a pinhole setup to study the average behavior in real space. The measurements were done below the silicon K-absorption edge in order to achieve high contrast from the aerosil particles trapped in the liquid-crystal. The results suggest that a dynamic coupling between the low-density aerosil-gel and the liquid-crystal in the manner of coupled springs not only mimics the liquid-crystal director fluctuations in the gel but also transfers energy from these fluctuations to the aerosil-gel dynamics, helping to suppress the director fluctuations. The observed relaxations at the smectic-A$_\mathrm{d}$-to-nematic phase transition do not show single-exponential decays that usually can be found for thermal processes, but higher-order exponential decays. This is a clear indication of the complexity of the dynamics present in the system. Presently, no theory explains such dynamic coupling. The results presented here suggest however that director fluctuations in smectics should be given more attention. A theoretical modelling of the system as a random set of coupled mass springs will probably allow to quantitatively deduce coupling and dampening strengths.

Increasing the real-space resolution using a zone plate setup is an obvious next step in the study of 8CB – aerosil dispersions. This will allow for a detailed study of small-amplitude few-particle dynamics in the system.

The time scales probed in this work were on the order of minutes. Almost all the results are consistent with the presence of shorter time scale dynamics. Therefore, further investigations should be done on shorter time scales. The CCD detector provides a 'kinetics' readout mode that allows for lag times on the order of microseconds. The principle of this mode is based on the fact that data transfer within the chip is faster than the readout process, which takes usually a time of the order of seconds. At least half of the CCD chip has to be masked for the kinetics readout mode. The unmasked stripe is exposed to radiation and, instead of being read out immediately, is transferred to the masked portion of the chip while the next stripe is exposed. Once the chip is filled with data, an interruption is needed for readout. The combination of many frames then yields the coverage of time scales from microseconds to hours. A copper mask has already been designed to be inserted within 2 mm distance from the CCD chip used in this work. It allows for selection of the size of the exposed stripe. Similar measurement techniques were already successfully explored elsewhere [LLMS00].

In some of the data presented here, the effect of the recirculating chiller used for temperature control was clearly visible. The stability of the setup was characterized by means of a pure self-supporting aerosil-gel reference sample. It was found that the chiller introduced small oscillations into the system. The activated gel's response relaxed with a time constant of ~ 13 minutes. Thus, only relaxation processes significantly different from this time structure could be interpreted as sample dynamics. However, in spite of the masking effect on the sample dynamics, the driving of the sample dynamics by external vibration is itself interesting to study as it will allow for better understanding of the nature of fluctuations of the system. For such a study, the vibrational and temperature control should be decoupled. Controlled fluctuations could be introduced into the system by means of a frequency-tunable transducer, whereas the temperature control could be done by resistive heating. The influence of the driving frequency on the rigidity and rigidity transitions of the dispersion would be very interesting to study.

The dependence of the dynamic behavior on the density of the aerosil-gel could show interesting properties. In order to better understand the cross-over behavior of low-density 8CB – aerosil dispersions, an XIFS investigation of aerosil in an isotropic solvent, such as acetone or glycerol, could be done as a function of aerosil density. From the observations in the 8CB –

aerosil dispersion, a rigidity transition in the aerosil is expected to be found around a density of 0.1 g(sil)$/$cm^3(total) [IGMR98]. To date there is no simple physical system available to study pure rigidity transitions and percolation connectivity [Ian01]. Aerosil might be such a system.

Furthermore, a dependence on the aerosil particle size and surface chemistry (e.g., methyl groups covering the surface instead of hydroxyl groups) should be investigated. The type of weakly connected gel formed by the pure aerosil will most likely depend on these properties. Therefore, the dynamics of the gel and, with this, the nature of the coupling to liquid-crystal dynamics might be influenced by them as well. A detailed study could help in understanding the details about the coupling.

Another future project should be an element-specific study of the structure found in this and other liquid-crystal-particle dispersions. This could be done by taking measurements at sample-specific absorption edges. Elements, such as germanium or tin, trapped inside a liquid-crystal matrix could be studied to compare their influence on the liquid-crystal with that of the aerosil. Because of their higher atomic number, these elements scatter more strongly. The larger scattered signal would allow for shorter recording times and the study of faster dynamics.

X-ray intensity fluctuation spectroscopy is a method with a great future. Many new insights into the dynamics and critical phenomena of both well-known and new materials and systems can be gained. It also enables new and existing theories to be probed. The applications of this method range from fundamental physics (e.g., probing of coherence properties) to industry (e.g., nanoparticle dispersions or surfactants) and biology (e.g., protein motion). XIFS is well suited for third-generation synchrotron facilities, such as the APS, where high coherent flux is available, an important requirement for studying fast dynamics. The realization of fourth-generation synchrotron sources, such as the free-electron laser (FEL) with its projected high peak brilliance, could push the current limitations of XIFS even further. The challenge of extremely high flux density and the probability of radiation damage will most likely require new approaches to sample preparation and protection. Yet, once these challenges are addressed, the unprecedented coherent flux and the expected time structure of the x-ray FEL will provide exciting new opportunities for probing sample structure and dynamics. The use of focusing optics and sample-specific absorption edges combined with speckle techniques broadens the field of x-ray intensity fluctuation spectroscopy allowing for new approaches in sample investigation. XIFS in the intermediate energy range of 1 to 4 keV has opened up another fascinating path for the application of modern synchrotron radiation sources.

Appendix A

Derivation of Speckle Widths in the Monochromatic Case

In this appendix, speckle widths in the azimuthal and radial directions are derived for the monochromatic case, starting from Eq. (1.14):

$$C_{\vec{r}}(\Delta\vec{r}) = \exp\Big(-\, \Delta q_z^2\, \sigma_T^2 - \big[\Delta q_r^2 + \Delta q_\phi^2\big]\, \sigma_D^2\Big)\ \big|\mu(D)\big|^2 \quad . \tag{A.1}$$

To derive the azimuthal speckle width Ω_{azim} in the direction of Δq_ϕ , Δq_z and Δq_r will be set to zero. Equation (A.1) then reduces to

$$C_{\vec{r}}(\Delta\vec{r}) = \exp\left(-\Delta q_\phi^2\, \sigma_D^2\right)\ \big|\mu(D)\big|^2 \quad , \tag{A.2}$$

which is a pure Gaussian function in Δq_ϕ. Therefore, the FWHM in Δq_ϕ is given by

$$\Omega_{\text{azim}} = \frac{2\sqrt{\ln(2)}}{\sigma_D} \quad . \tag{A.3}$$

In deriving the radial speckle width Ω_{rad} , which is perpendicular to the azimuthal direction, i.e., for $\Delta q_z \neq 0$, $\Delta q_r \neq 0$, and $\Delta q_\phi = 0$, Eq. (A.1) leads to the following form:

$$C_r(\Delta r) = \exp\left(-\Delta q_z^2\, \sigma_T^2 - \Delta q_r^2\, \sigma_D^2\right)\ \big|\mu(D)\big|^2 \quad . \tag{A.4}$$

To extract a width from this equation, it is useful to express Δq in terms of 2θ (compare to Eq. (1.13)):

$$\begin{aligned} \Delta q_r &= k\Big[\sin(2\theta_2) - \sin(2\theta_1)\Big] \quad , \\ \Delta q_z &= k\Big[\cos(2\theta_2) - \cos(2\theta_1)\Big] \quad , \end{aligned} \tag{A.5}$$

where k is the length of $\vec{k}_{\text{in}}$ as well as $\vec{k}_{\text{out}}$ and $2\theta_1$ and $2\theta_2$ are the two scattering angles. They describe the two radial positions on the detector.

With these expressions, Eq. (A.4) becomes

$$C_r(\Delta r) = \exp\left(-k^2\Big[\cos(2\theta_2) - \cos(2\theta_1)\Big]^2 \sigma_T^2 - k^2\Big[\sin(2\theta_2) - \sin(2\theta_1)\Big]^2 \sigma_D^2\right) \; \big|\mu(D)\big|^2 \; . \tag{A.6}$$

The radial speckle width is derived from Eq. (A.6) by comparing it with a Gaussian function. To do this, the exponent of Eq. (A.6) is developed into a Taylor series around $2\theta_1 = 2\theta_2$:

$$-k^2\Big[\sigma_T^2 \sin^2(2\theta_2) \; + \; \sigma_D^2 \cos^2(2\theta_2)\Big] \; [2\theta_2 - 2\theta_1]^2 + O\Big([2\theta_2 - 2\theta_1]^3\Big) \; . \tag{A.7}$$

Neglecting third and higher order terms in the very small angular difference between $2\theta_1$ and $2\theta_2$, the *angular* FWHM $\Omega_{\text{rad},2\theta}$ in real space is given by

$$\Omega_{\text{rad},2\theta} = \frac{2\sqrt{\ln(2)}}{k\sqrt{\sigma_T^2 \sin^2(2\theta) + \sigma_D^2 \cos^2(2\theta)}} \; . \tag{A.8}$$

To convert this into units of reciprocal space, the Bragg relation $q = 2k \, \sin\left(\frac{2\theta}{2}\right)$ is used:

$$\Omega_{\text{rad}} = 2k \; \sin\left(\frac{\sqrt{\ln(2)}}{k\sqrt{\sigma_T^2 \sin^2(2\theta) + \sigma_D^2 \cos^2(2\theta)}}\right) \; , \tag{A.9}$$

which, with $\sin(\Omega_{\text{rad},2\theta}) \approx \Omega_{\text{rad},2\theta}$ in the small angle approximation, can be simplified to

$$\Omega_{\text{rad}} \approx \frac{2\sqrt{\ln(2)}}{\sqrt{\sigma_T^2 \sin^2(2\theta) + \sigma_D^2 \cos^2(2\theta)}} \; . \tag{A.10}$$

Appendix B

Influence of Aperture Shapes on Speckle Widths and Contrast

This appendix discusses the influence of aperture shapes on speckle patterns. A speckle pattern in the Fraunhofer regime is described mathematically by the Fourier transform of the illuminated volume in the sample. The shape of this volume is defined by the shape of the beam and the thickness of the sample. The most important cases are a circular and a slit-type shape, described mathematically by the 'circ' and the 'rect' function:

$$\mathrm{circ}\Big(\sqrt{x^2+y^2}\Big) \equiv \begin{cases} 0 & : \quad x^2+y^2 > 1 \\ 1 & : \quad x^2+y^2 \leq 1 \end{cases} , \tag{B.1}$$

$$\mathrm{rect}(x) \equiv \begin{cases} 0 & : \quad |x| > 1 \\ 1 & : \quad |x| \leq 1 \end{cases} . \tag{B.2}$$

A Fourier transform (FT) of a circular function yields

$$\mathrm{FT}\Big(\mathrm{circ}(r)\Big) = \frac{2\pi J_1(\nu)}{\nu} , \tag{B.3}$$

where J_1 is the Bessel function of the first kind and order one and ν and r are related by $\nu = 2\pi/r$. For a slit-type aperture, the Fourier transform gives a sinc function:

$$\mathrm{FT}\Big(\mathrm{rect}(r)\Big) = \frac{\sin(\nu)}{\nu} \equiv \mathrm{sinc}(\nu) . \tag{B.4}$$

These two functions are plotted in Fig. B.1.

A speckle pattern is given by the Fraunhofer scattering from the wavefront disturbance introduced by the sample volume (see Eq. (1.5)):

$$A(\vec{r}) = \frac{k\ \exp\big(ikR_{\mathrm{det}}\big)}{2\pi i\, R_{\mathrm{det}}} \iint B(\vec{r}_0)A(\vec{r}_0)\ \exp\big(-i\,\vec{q}\,(\vec{r})\cdot\vec{r}_0\big)\ \mathrm{d}r_0^3 , \tag{B.5}$$

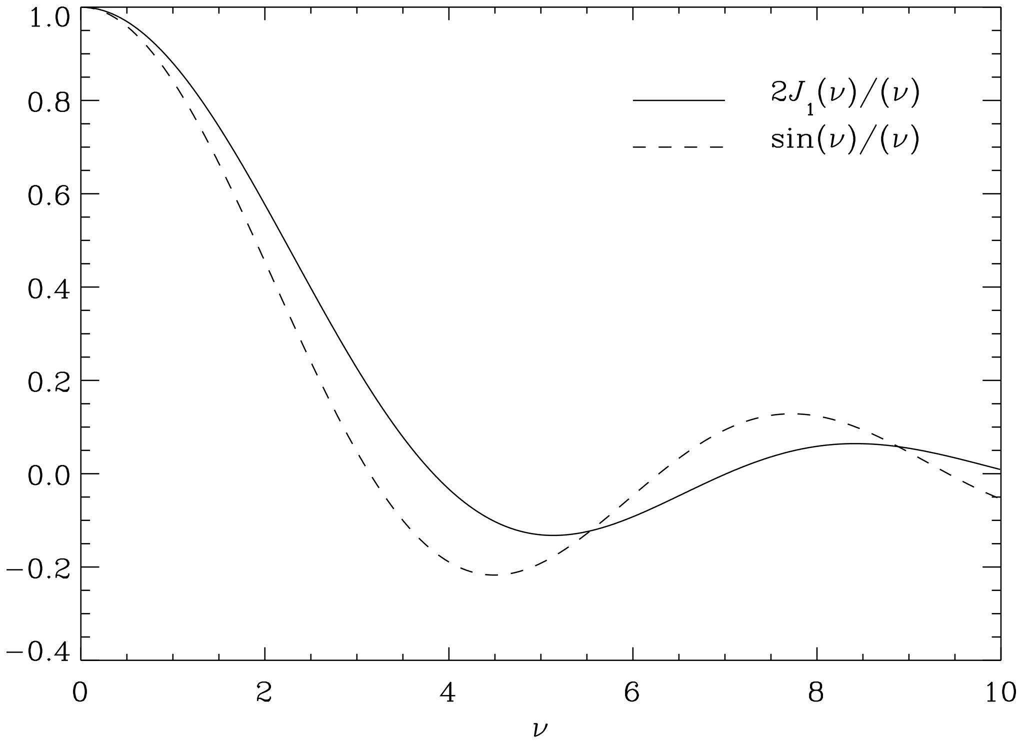

Figure B.1: *Fourier transforms of a* circ *function (solid curve) and a* rect *function (dashed curve). Both functions are normalized to unity for* $\nu = 0$.

where $A(\vec{r})$ is the amplitude in the plane of observation. In Chapter 1.2, assumptions I-III ensure that sample correlations do not affect the speckle size. They will only modulate the pattern on length scales that are large compared to the speckle size. Thus, the largest probed distance in the sample plane (the size of the aperture) determines the smallest unit in the Fraunhofer pattern (the size of the speckle). Therefore, a plain aperture shall now be considered and the influence of sample correlations within the size of this aperture shall be neglected. $B(\vec{r}_0)$ is then given by the aperture function, and $A(\vec{r}_0)$ is considered to be unity. Therefore, for a circular aperture of diameter l, located at distance R_{det} from the plane of observation, and with $r_0^2 = x_0^2 + y_0^2$,

$$B(\vec{r}_0) = B(r_0) = \text{circ}\left(\frac{r_0}{l/2}\right) \quad , \tag{B.6}$$

and for $r^2 = x^2 + y^2$,

$$A(\vec{r}) = A(r) = \frac{k \, \exp\left(ikR_{\text{det}}\right)}{2\pi i \, R_{\text{det}}} \, \frac{\pi l^2}{4} \left[2 \, \frac{J_1\left(klr/2R_{\text{det}}\right)}{klr/2R_{\text{det}}}\right] \quad . \tag{B.7}$$

For a one-dimensional slit aperture of size l,

$$B(x_0) = \text{rect}\left(\frac{x_0}{l}\right) \quad , \tag{B.8}$$

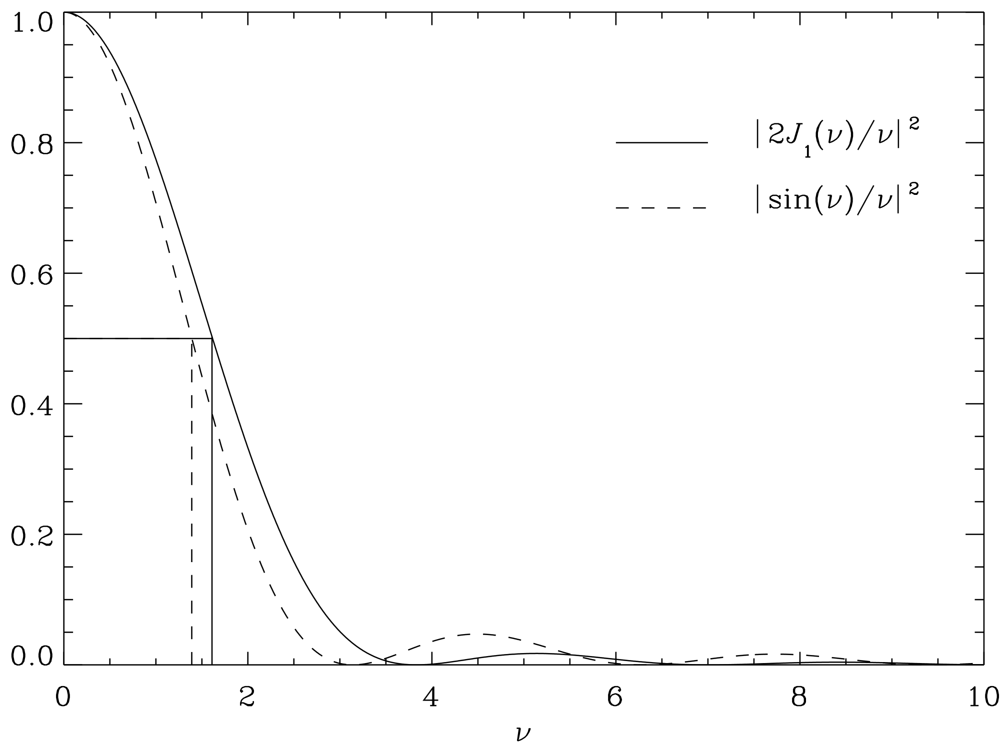

Figure B.2: Airy *function (solid curve) and the absolute square of a* sinc *function (dashed curve). Both functions are normalized to unity at $\nu = 0$. $\nu_{50\%}$ is indicated on both curves.*

and with this,

$$A(x) = \frac{k\,\exp\left(ikR_{\rm det}\right)}{2\pi i\,R_{\rm det}}\;l\;\left[\mathrm{sinc}\left(\frac{klx}{2R_{\rm det}}\right)\right] \quad . \tag{B.9}$$

In general, with

$$\nu = \frac{klr}{2R_{\rm det}} \quad , \tag{B.10}$$

where l is the aperture's diameter, the resulting intensity can be expressed as

$$I(r) \propto \Big|\Upsilon(\nu)\Big|^2 \quad , \tag{B.11}$$

where $\Upsilon(\nu)$ stands for either '$2J_1(\nu)/\nu$' or 'sinc(ν)', depending on the type of the aperture. Both intensity functions are shown in Fig. B.2. The function $|\Upsilon|^2$ for a circular aperture is known as an Airy function.

The 50% level of Eq. (B.11) occurs when

$$\nu_{50\%,\rm circ} \approx 1.616 \tag{B.12}$$

or

$$\nu_{50\%,\rm slit} \approx 1.392 \quad . \tag{B.13}$$

For these ν, r is the distance from the maximum at $\nu = 0$ to the 50% level in the pattern. The FWHM r_{FWHM} is therefore given by twice this distance:

$$r_{\mathrm{FWHM,circ}} = 2\,\nu_{50\%,\mathrm{circ}} \frac{2R_{\mathrm{det}}}{kl} \approx 1.03 \frac{2\pi R_{\mathrm{det}}}{kl} \quad , \tag{B.14}$$

$$r_{\mathrm{FWHM,slit}} = 2\,\nu_{50\%,\mathrm{slit}} \frac{2R_{\mathrm{det}}}{kl} \approx 0.89 \frac{2\pi R_{\mathrm{det}}}{kl} \quad . \tag{B.15}$$

To transfer r_{FWHM} into units in reciprocal space, the relation $q = 2k\sin\left(\frac{2\theta}{2}\right)$ will be used, where 2θ is the scattering angle. This yields

$$\begin{aligned} \Omega_{\mathrm{FWHM}} &= 2k\sin\left(\arctan\left(\frac{r_{\mathrm{FWHM}}}{2R_{\mathrm{det}}}\right)\right) \\ &= 2k\sin\left(\arctan\left(\frac{2\nu_{50\%}}{kl}\right)\right) && \text{(B.16)} \\ &\approx 4\frac{\nu_{50\%}}{l} \quad , && \text{(B.17)} \end{aligned}$$

where the small angle approximation was used for the last step. Comparing this width in reciprocal space with the result from Eq. (1.15), one obtains

$$\frac{2\sqrt{\ln(2)}}{\sigma_l} = 4\frac{\nu_{50\%}}{l} \quad \Rightarrow \quad \sigma_l = \frac{\sqrt{\ln(2)}}{2\nu_{50\%}}\, l \quad , \tag{B.18}$$

i.e.,

$$\sigma_{l,\mathrm{circ}} = \frac{\sqrt{\ln(2)}}{1.03\pi}\, l = 0.26\, l \tag{B.19}$$

for the circular aperture and

$$\sigma_{l,\mathrm{slit}} = \frac{\sqrt{\ln(2)}}{0.89\pi}\, l = 0.30\, l \tag{B.20}$$

for the slit-type aperture.